ELECTROCHEMICAL DECARBOXYLATION OF CARBOXYLIC ACIDS OVER PLATINUM SURFACES FOR BIO-OIL UPGRADING

Margot Olde Nordkamp

ELECTROCHEMICAL DECARBOXYLATION OF CARBOXYLIC ACIDS OVER PLATINUM SURFACES FOR BIO-OIL UPGRADING

DISSERTATION

To obtain
the degree of doctor at the University of Twente,
on the authority of the rector magnificus,
prof. dr. ir. A. Veldkamp,
on account of the decision of the Doctorate Board,
to be publicly defended
on Friday the 1st of March 2024 at 14.45 hours

by

Margot Josephina Maria Olde Nordkamp

born on the 27th of February, 1995
in Oldenzaal, the Netherlands

This dissertation has been approved by:

Promotor:
Prof. dr. G. Mul

Co-promotor:
Prof. dr. B.T. Mei

The research in this thesis was performed in the PhotoCatalytic Synthesis group within the Faculty of Science and Technology, and the MESA+ Institute for Nanotechnology at the University of Twente. This project has received funding from Topconsortia voor Kennis en Innovatie – Biobased Economy (TKI-BBE).

Cover design:	Drawing representing the electrochemical upgrading of bio-oil through the electrochemical conversion of carboxylic acids, by Margot Olde Nordkamp
Printed by:	Ispkamp Printing
Lay-out:	Margot Olde Nordkamp
ISBN (print)	978-90-365-5992-8
ISBN (digital)	978-90-365-5991-1
DOI:	10.3990/1.9789036559928

Graduation committee

Chair/Secretary

Prof. dr. J.L. Herek	University of Twente

Promotor

Prof. dr. G. Mul	University of Twente

Co-promotor

Prof. dr. B.T. Mei	University of Twente
	Ruhr Universität Bochum

Committee members

Prof. dr. F. Harnisch	Universität Leipzig
	Helmholtz Centre for Environmental Research
Prof. dr. P.C.A. Bruijnincx	University of Utrecht
Prof. dr. S.R.A. Kersten	University of Twente
Prof. dr. C.A. Nijhuis	University of Twente
Dr. R.H. Venderbosch	Biomass Technology Group B.V.

Samenvatting

In dit proefschrift wordt de elektrochemische anodische decarboxylering van carbonzuren met een korte keten op platina elektroden voor de opwaardering van bio-olie onderzocht en besproken. Het belangrijkste doel hierbij is om de chemische transformaties te begrijpen die optreden op de Pt anode, en specifiek de afhankelijkheid van deze transformaties van de pH van het elektrolyt, de aard van het carbonzuur en de morfologie van de Pt anode. Daarnaast wordt de haalbaarheid van het gebruik van Pt anodes met een lage Pt belading besproken om de kosten van het elektrodemateriaal te verminderen. Bovendien werd gepulseerde elektrolyse van mengsels van carbonzuren gebruikt om de opbrengst te verhogen en de productselectiviteit te optimaliseren. Over het algemeen was het doel om de economische levensvatbaarheid van elektrochemische decarboxylering te vergroten.

In **Hoofdstuk 1** wordt het gebruik van elektrochemische decarboxylering van carbonzuren (ook wel Kolbe-elektrolyse genoemd) voor het verbeteren van de samenstelling van bio-olie gemotiveerd. Allereerst wordt de relevantie van bio-olie als duurzame energiebron behandeld, gevolgd door een introductie van elektrochemische opwaarderingstechnologieën gericht op het verbeteren van de kwaliteit van bio-olie. Hierna verschuift de focus naar Kolbe-elektrolyse en het potentieel ervan om bio-gebaseerde carbonzuren om te zetten naar waardevolle chemicaliën. Hoofdstuk 1 sluit af met een overzicht van de belangrijkste uitdagingen en de recente technologische vooruitgang op het gebied van Kolbe-elektrolyse voor het opwaarderen van bio-olie.

In **Hoofdstuk 2** wordt het onderzoek beschreven met betrekking tot de prestaties van Pt anodes met een lage Pt belading in de elektrochemische decarboxylering van azijnzuur. Geplatineerde elektroden werden gemaakt via elektrodepositie (Pt-ED/Ti), sputteren (Pt-TF/Ti) en een zogenoemde ‘dewetting’ procedure (Pt/FTO) op titanium of fluor-gedoteerd tin oxide substraten met als doel om elektroden met verschillende Pt-oppervlaktebedekkingen te verkrijgen. Pt-ED/Ti elektroden waren inactief voor Kolbe-elektrolyse vanwege de lage oppervlaktebedekking van Ti met Pt, welke resulteerde in de oxidatie van het

blootgestelde Ti-substraat. De Pt/FTO elektroden vertoonden een hoge anodische productie van ethaan, maar de selectiviteit nam in de loop van de tijd af door blootstelling van het FTO-substraat, wat leidde tot een verhoogde vorming van zuurstof. Pt-TF/Ti elektroden vertoonden een hoge selectiviteit voor Kolbe-elektrolyse vergelijkbaar met die van pure Pt-anodes, maar het voortdurend oplossen van Pt zorgde voor een verminderde stabiliteit van deze elektroden. Om de levensduur van Pt-anodes met lage Pt belading te verlengen en zo de praktische haalbaarheid in Kolbe-elektrolyse te verbeteren, zouden anodes met dunne, volledig dekkende films van Pt op het substraat, gebruikt moeten worden. Hierbij dient het oplossen van Pt zoveel mogelijk vermeden te worden.

In **Hoofdstuk 3** is de oppervlaktestructuur en samenstelling van pure Pt-anodes onderzocht tijdens Kolbe-elektrolyse van azijnzuur. Metingen met cyclische voltammetrie, gegevens van de elektrochemische kwartskristalmicrobalans en spectra van röntgenabsorptiespectroscopie toonden aan dat continue oxidatie van platina werd belemmerd door de aanwezigheid van een barrière laag van (geadsorbeerde) acetaat moleculen op het elektrode-oppervlak. Bovendien onthulden gegevens van inductief gekoppelde plasma-massaspectrometrie (ICP-MS) dat het oplossen van Pt werd versterkt in aanwezigheid van (geadsorbeerd) acetaat. Verdere studies om de oplossnelheid van Pt onder Kolbe-omstandigheden te verkennen zijn vereist om de economische levensvatbaarheid van elektro-organische synthese via Kolbe-elektrolyse te beoordelen.

In **Hoofdstuk 4** is de invloed van de pH van het elektrolyt tijdens Kolbe-elektrolyse van azijnzuur op pure Pt-anodes onderzocht. Het Kolbe-product (ethaan) werd selectief geproduceerd bij het gebruik van een elektrolyt met een pH gelijk aan of groter dan de pKa-waarde van azijnzuur. Echter, in een alkalisch elektrolyt (pH 9 en pH 12) verschoof de selectiviteit in de loop van de tijd naar het Hofer-Moest-product methanol. De vorming van het co-product koolstofdioxide en de daaropvolgende vorming van carbonaat en bicarbonaat belemmeren het dimerisatie proces, waardoor een selectiviteitsverschuiving optreedt. Wanneer selectiviteit naar het Kolbe-product gewenst is, dient

ophoping van koolstofdioxide vermeden te worden. Dit kan door gebruik te maken van doorstroomreactoren.

In **Hoofdstuk 5** is Kolbe-elektrolyse van (mengsels van) azijnzuur, propionzuur en hexaanzuur onderzocht op Pt-anodes. In een mengsel van azijnzuur en propionzuur werd propionzuur dominant omgezet ten opzichte van azijnzuur, terwijl in een mengsel van hexaanzuur en propionzuur het hexaanzuur dominant werd omgezet. Temkin-adsorptie-isothermen onthulden dat hexaanzuur sterker adsorbeert aan het elektrode-oppervlak dan propionzuur en azijnzuur, wat de variaties in zuurconversie, productselectiviteit en substraatspecificiteit verklaart. Door gebruik te maken van pulserende elektrolyse kan productselectiviteit gemanipuleerd worden. Door het toedienen van blokgolf galvanische pulsen, kan substraatspecificiteit en productselectiviteit in mengsels van azijnzuur en propionzuur gestuurd worden naar propionzuurconversie. Niettemin is het noodzakelijk om deze galvanische pulsen te combineren met methoden om zuurstofvorming zoveel mogelijk te beperken. Dit maakt een efficiënte conversie van carbonzuren via Kolbe-elektrolyse mogelijk voor de productie van brandstoffen en chemicaliën.

List of abbreviations and symbols

Abbreviations

AC	alternating current
AD	as deposited
BDD	boron-doped diamond
C_2H_4	ethylene
C_2H_6	ethane
capex	capital expenditure
CV	cyclic voltammetry
CE	counter electrode
CFP	carbon fiber paper
CO_2	carbon dioxide
C_n	carboxylic acid with chain length of n carbon atoms
DC	direct current
DFT	density functional theory
ECH	electrochemical hydrogenation
ECO	electrochemical oxidation
ECSA	electrochemical surface area
EDX	energy dispersive X-ray spectroscopy
ESRF	European synchrotron radiation facility
eQCM	electrochemical quartz crystal microbalance
EXAFS	extended x-ray absorption fine structure
FE	faradaic efficiency
FID	flame ionization detector
FTO	fluorine-doped tin oxide
GC	gas chromatography
HPLC	high pressure liquid chromatography
ICP-MS	inductively coupled plasma mass spectroscopy
IrO_2	iridium oxide
LSV	linear sweep voltammetry
O_2	oxygen
OCV	open circuit voltage
OER	oxygen evolution reaction
NP	nanoparticles
Pt	platinum
Pt-ED	electrodeposited Pt
PTFE	polytetrafluoroethylene (Teflon)
Pt-TF	thin film of Pt
PtO	platinum oxide

RDE	rotating disc electrode
RE	reference electrode
RF	radio frequency
RHE	reversed hydrogen electrode
rpm	rotations per minute
RRDE	rotating ring disc electrode
RuO_2	ruthenium oxide
SEIRAS	surface-enhanced infrared spectroscopy
SERS	surface-enhanced Raman spectroscopy
SHINs	shell isolated nanoparticles
SEM	scanning electron microscopy
SNR	signal-to-noise
TCD	thermal conductivity detector
Ti	titanium
WE	working electrode
XANES	x-ray absorption near edge structure
XPS	x-ray photoelectron spectroscopy

Symbols

E	cell potential (V)
F	Faraday constant (96.485 C mol^{-1})
FE	Faradaic efficiency (%)
H_{upd}	hydrogen underpotential deposition
I	current (mA)
J	current density (mA/cm^2)
pKa	acid dissociation constant (-)
Q	molar He gas flow rate (mol/s)
Q_a	passed anodic charge (C)
Q_c	passed cathodic charge (C)
t	time (s)
t_a	anodic pulse duration (ms)
t_c	cathodic pulse duration (ms)
V	volume (L)
z_i	number of the electrons needed for the formation of product I (-)
α	slope (-)
Φ_i	volume fraction of gas i (%)

Table of Contents

“Alles wordt, niets is.”
- *Plato*

Chapter 1

An introduction to electrochemical upgrading of bio-oil

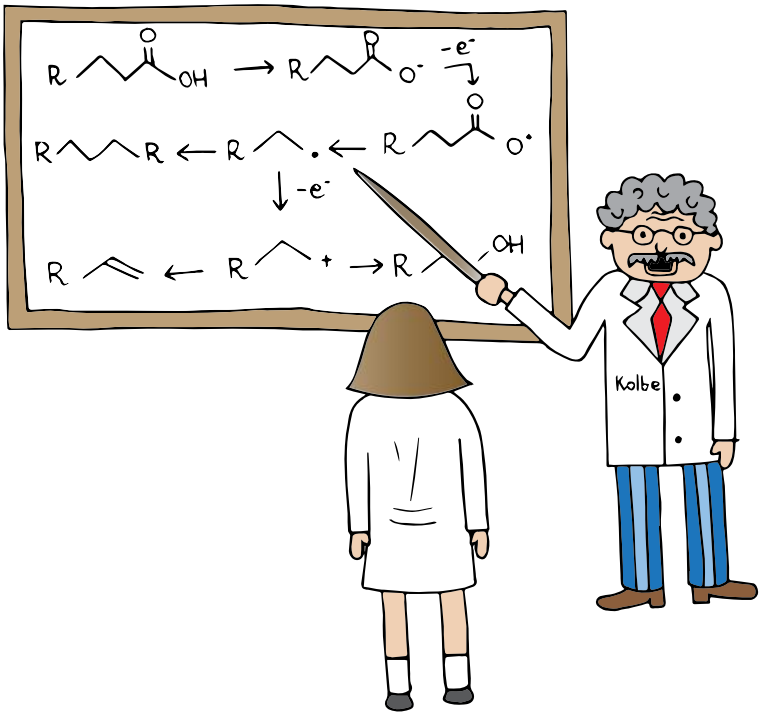

1.1. Global energy: supply, demand and consequences

Over hundred centuries ago, humans solely relied on wood fires to find use in heating and cooking. Today, houses are equipped with modern heating systems and are connected to the electrical grid, providing convenience at the push of a button. Throughout human history, our energy landscape has experienced considerable shifts. In the past, energy generation was dependent on manual labour and wood fires, whereas our present energy supply heavily leans on fossil fuel sources[1]. The invention of the steam engine in the 18th century has substantially increased the utilization of fossil fuels, now accounting for more than 80% of our worldwide annual energy consumption[2]. As both global population and human prosperity are expanding, the depletion of fossil fuels will inevitably continue to increase[3]. This poses challenges for the future, not only because our fossil fuel reserves are limited, but also because the combustion of these fuels is accompanied by greenhouse gases emissions, like carbon dioxide (CO_2).

Nature can absorb CO_2 using sunlight through photosynthesis. However, due to the slow formation of fossil fuels combined with their rapid combustion in large quantities, a significant portion of CO_2 cannot be adsorbed and consequently will accumulate in the atmosphere[4]. Since the beginning of the Industrial Age, the atmospheric CO_2 concentration has increased from 280 parts per million (ppm) to 412 ppm today[5]. It is expected that this number continues to rise if we maintain our reliance on fossil fuels. Since atmospheric CO_2 traps solar radiation and releases it in the form of heat, elevated levels of CO_2 will result in global warming. The global average temperature has increased by at least 1.1 ºC[6] since the beginning of the industrial age, while solar activity remained relatively constant. This temperature rise has far-reaching implications for our existence on Earth. Already noticeable is polar ice melting and subsequent sea level rise. By the end of this century, projections for the rise in sea levels vary between 0.8 to 2 meters[7], enough to completely submerge large coastal cities, like New York or Rotterdam[8].

To mitigate global warming and reduce the impact on our climate, steps must be taken to reduce greenhouse gas emissions. This involves harnessing alternative, clean and renewable energy sources to replace fossil fuels. Decades ago, the transition from fossil fuels to renewable energy sources was initiated by the production of energy through wind and solar power. Energy from solar and wind is abundantly available and the production of electricity from these sources does not emit greenhouse gases. Presently, roughly 40% of our renewable energy worldwide is derived from wind and solar power[9]. However, other forms of renewable energy are explored as well as fluctuations in availability of sun and wind causes technological limitations. Figure 1.1 shows a schematic representation of a typical daily load profile for solar and wind energy production and energy usage.

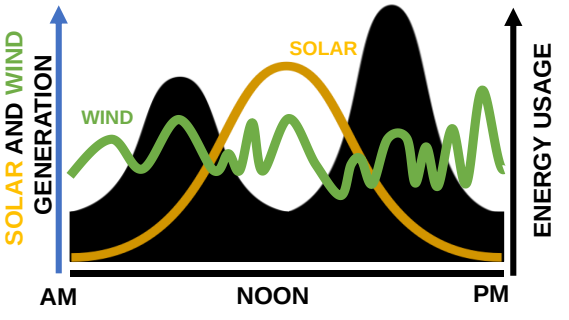

Figure 1.1 Schematic representation of daily load profile for solar (yellow line) and wind (green line) generation and energy usage (black area). Based on International Energy Agency (IEA), 2023.

For practical all industrial processes, a reliable and continuous source of energy is essential. Moreover, sectors like the chemical industry and the transportation sector face challenges in electrifying their processes, because substantial investments of time and money are required to replace their current technology[10,11]. For these reasons, there is a need for a reliable, continuous energy source that can efficiently be utilized without substantial adaptations to existing technology.

1.2. Energy from biomass

Energy from biomass holds potential to form a significant portion of the anticipated renewable energy provisions of the future offering biofuels in various forms like gas, liquid and solid fuels along with applications in electricity and heat[12]. For the two latter, biomass played a predominant role worldwide prior to the industrial revolution, however it remains important today as it is widely used in cooking and heating in the developing world. Nonetheless, much of today's attention on biomass as an energy source focuses on liquid transportation fuels[13,14]. Biobased fuels are emerging as excellent renewable additives to fossil-based fuels as they reduce the overall carbon footprint of the transport sector which heavily depends on petroleum[15]. Besides, existing infrastructure does not require significant alterations to employ biobased fuels in transportation.

Biomass refers to any source of organic matter that can be utilized as renewable and sustainable source of energy. It includes various biological materials such as wood and agricultural residues but also encompasses by-products from agricultural and industrial sectors such as manure or pulp sludge. Biofuels can be classified into three generations[16]. The so called first generation (1G) refers to biofuels produced from edible energy crops. The use of this generation biofuels however has raised serious concerns on food supply, food security and cultivable land needs[17]. Second generation biofuels (2G) are fuels produced from various types of non-food biomass. Although, these type of biofuels do not impact global food production, manufacturing process are more complex and less well developed than those for first generation biofuels[18]. Third generation fuels (3G) are produced from microalgae, however the commercialization of these biofuels faces serious challenges in terms of economic feasibility[19]. Therefore the production of these fuels is still primarily limited to the laboratory and pilot scale[20].

To produce biofuels, biomass can be thermochemically converted, for example through gasification or liquefaction (pyrolysis or hydrothermal liquefaction). In gasification, the biomass is heated to temperatures reaching up to 900 ºC in an

oxygen environment to produce syngas[21]. This gas can be further processed to liquid fuels using Fischer-Tropsch synthesis. In liquefaction, the biomass is heated to produced liquid products from the biomass. The most matured liquefaction technology is pyrolysis, in which biomass is rapidly heated to lower temperatures of 450-600 ºC in absence of oxygen to produce the so-called pyrolysis oil (typically 65 wt%), char (15 wt%) and non-condensable gases (20 wt%)[22]. Pyrolysis oil, also referred to as bio-oil contains a wide variety of organic compounds including carboxylic acids, alcohols, carbohydrate derivatives and defragmented lignin. Due to the high water (15-30 wt%) and oxygen content (up to 50 wt%), the energy density of raw bio-oil is rather low[23,24]. In addition to a high corrosiveness, caused by the presence of carboxylic acids with acetic acid being one of the most abundant molecules in the oil[25], the oil has a low thermal stability. Therefore, upgrading processes are required to increase the quality of the oil.

There have been intensive studies on bio-oil upgrading. Various technologies have been developed for bio-oil upgrading of which catalytic hydrotreating and catalytic cracking are most widely used[26]. In catalytic hydrotreating, bio-oil is mixed with hydrogen and passed over a catalyst bed at high temperatures and pressures (300-450˚C, up to 200 bar)[26] to eliminate undesired elements such

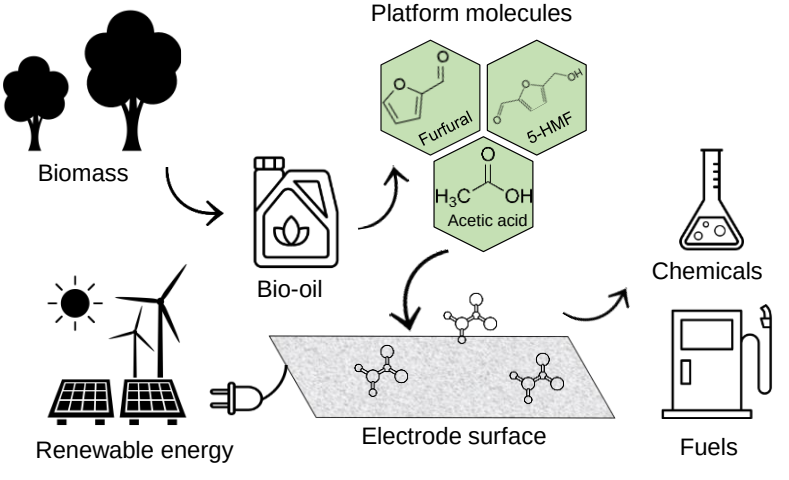

Figure 1.2 Schematic representation of electrochemical upgrading of bio-oil for the production of chemicals and fuels.

as nitrogen, sulphur and oxygen. In catalytic cracking, hydrogenation reactions are accompanied by cracking over zeolite catalysts at temperatures above 350˚C and pressures up to 200 bars[27]. This process is highly effective in producing large amounts of light products. Despite the effectiveness, significant quantities of energy and hydrogen are required. Hydrogen is typically obtained via fossil fuel-based processes, leading to a considerable carbon dioxide footprint. Furthermore, due to severe coke formation reactor clogging can occur, as a consequence of the deactivation of the catalyst[28]. Considering the expected surplus in electricity due to increasing capacities in wind and solar installations, electrochemical techniques can be of great interest, for example to deliver the 'green' hydrogen. Moreover, and part of this thesis, it can also be used in upgrading of bio-oil, as at the moderate reaction conditions required it is an appealing alternative to catalytic upgrading to obtain fuels and/or chemicals (Figure 1.2).

1.3. Electrochemical conversion of bio-oil

In an electrochemical cell, bio-oil compounds can be converted electrochemically using electrons supplied via (renewable) electricity[29]. The potential difference applied between two electrodes triggers a flow of electrons which facilitates the movement of ions to the electrode surfaces where the

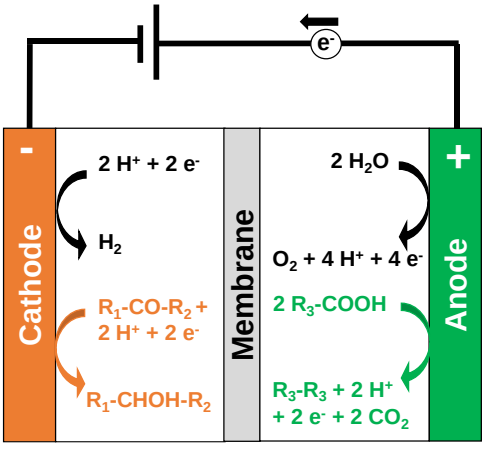

Figure 1.3 Schematic representation of an electrochemical cell with hydrogen evolution (black) and electrochemical hydrogenation of ketones (orange) at the cathode and oxygen evolution (black) and electrochemical oxidation of carboxylic acids (green) at the anode.

reactants are converted[30]. At the negative electrode (cathode), compounds are reduced whereas at the positive electrode (anode), oxidation reactions take place. Figure 1.3 displays a schematic representation of an electrochemical cell in aqueous media exemplifying the conversion of biobased platform molecules. Besides the formation of hydrogen from protons, electrochemical hydrogenation (ECH) of biobased platform molecules such as ketones can occur at the cathode. At the anode, alongside the formation of oxygen from water molecules, electrochemical oxidation (ECO) of biobased compounds like carboxylic acids can take place.

Several different approaches to electrochemical upgrading of bio-oils have been proposed in the literature[29,31–37], discussing ECH[33–35] and/or ECO[36,37]. A wide variety of bio-oil model compounds has been hydrogenated including benzaldehyde[38], acetone[39] and furfural[40]. The primary focus of ECH research until today has been on increasing mechanistic understanding and on the development of efficient and selective electrocatalysts. A wide range of metals have been found to be active for ECH including precious metals (i.e., Pt, Pd, Ru, Rh) and non-precious metals (i.e., Ni, Cu, Co). Besides model compounds, ECH has also shown to be effective in actual bio-oil treatment[41,42]. The extent to which the quality of the fuels produced using ECH is improved compared to traditional upgrading techniques (i.e., hydrotreating) is likely lower, however preliminary economic and environmental analyses have shown that ECH can provide economic and environmental benefits compared to or in conjunction to traditional thermochemical bio-oil upgrading processes[31].

Research into ECO of biomass-derived compounds received far less attention in literature, however this field is expanding as ECO has the potential to produce value added chemicals while simultaneously producing H_2 or hydrogenated compounds at the cathode. As ECO reactions often have faster reaction kinetics than the oxygen evolution reaction (OER) from water, the overall process generally requires lower overpotentials compared to those of conventional water electrolysis[43]. Moreover, the value of ECO products is typically higher than that of oxygen. High product yields have been obtained during ECO of e.g. 5-

hydroxymethylfurfural (HMF)[44], furfural[45] and valeric acid[46]. Electrochemical conversion of bio-derived carboxylic acids via Kolbe electrolysis has been proposed to produce valuable compounds while upgrading bio-oil[47–54].

1.4. Kolbe electrolysis of carboxylic acids

1.4.1. The history of Kolbe electrolysis

Kolbe electrolysis, named after the German chemist Hermann Kolbe, was discovered in 1848 and is an important reaction in organic chemistry to produce hydrocarbons. In the Kolbe reaction, two carboxylic acids are decarboxylated to two radicals which can dimerize and form an alkane (see reaction equation 1.1).

$$2\,RCOOH \rightarrow R-R+2\,CO_2+2H^+ +2e^- \qquad (1.1)$$

The reaction was first encountered by Faraday in 1834, when he studied the electrochemical behaviour of acetate ions, and noticed the production of an inflammable gas[55]. However, it was Hermann Kolbe that described the reaction in more detail and applied it to synthesize numerous hydrocarbons[56]. Hereafter, several discoveries were made that are important for our current understanding on Kolbe electrolysis. In 1855, Charles Adolphe Wurtz demonstrated that unsymmetrical hydrocarbons could be formed by carbon-carbon coupling of two different alkyl radicals when performing Kolbe electrolysis on a feed containing two different acids[57]. In 1891, Crum-Brown and Walker researched Kolbe electrolysis of dicarboxylic acids and found that the difficulties in selectivity in the coupling of dicarboxylic acid electrolysis could be conquered by oxidizing the half esters of the dicarboxylic acids[58]. Ten years later, Hofer and Moest showed that variations in the reaction conditions during Kolbe electrolysis resulted in the formation of alcohols[59].

1.4.2. Reaction mechanism of Kolbe electrolysis

Various theories regarding the reaction mechanism of Kolbe reactions have been suggested and discussed over the past century. Currently, there is much consensus about the concept depicted in Figure 1.4. In the presence of base, deprotonation of carboxylic acid occurs. The resulting carboxylate anions adsorb on the anode surface due to the attractive force generated by the applied positive

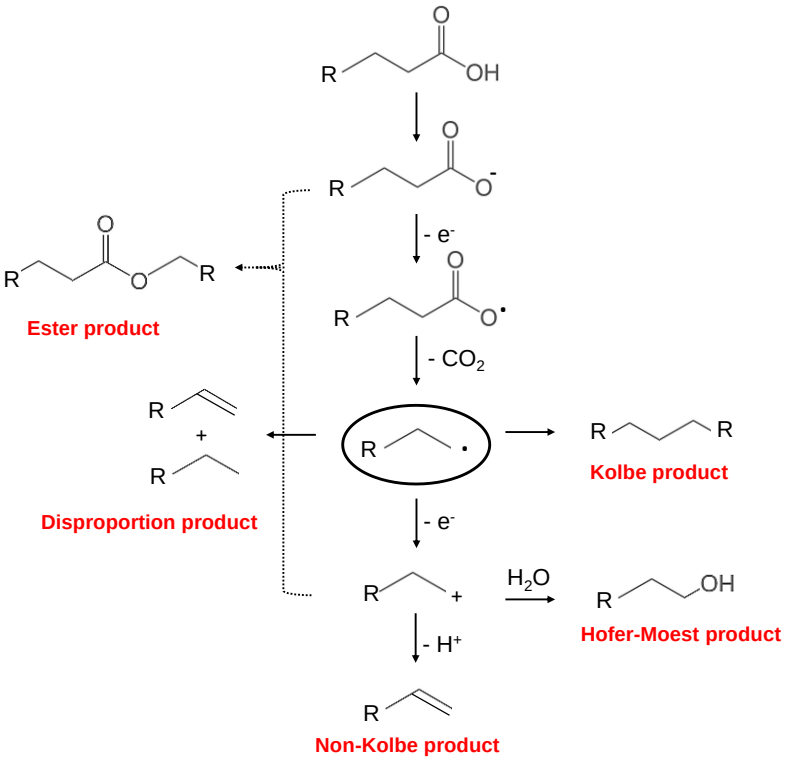

Figure 1.4 Schematic representation of the reaction mechanism for the formation of Kolbe, Hofer-Moest, Non-Kolbe, disproportion and ester products.

potential. Hereafter, an irreversible single-electron transfer occurs from the carboxylate to the anode, while simultaneous decarboxylation results in the formation of alkyl radicals and CO_2. These alkyl radicals further react via four distinct reaction pathways depending on the specific reaction conditions. In the first reaction pathway, alkyl radicals dimerize to form prolonged alkanes (Kolbe product). Besides, the disproportion of two alkyl radicals can occur generating an alkane and alkene (disproportion products). Moreover, oxidation of the alkyl radicals is possible leading to the formation carbenium ions. These can either react with an alkene via β-H-elimination forming non-Kolbe products or hydrolyse to form alcohols (Hofer-Moest products). Lastly, esters can be formed via the reaction of the carbenium ion with a deprotonated acid. Oxygen evolution or solvent oxidation are competing side reactions in aqueous or alcoholic solutions. However, at a critical potential of 2.1 to 2.7 V vs. RHE (reversed hydrogen

electrode), the coverage of the surface with alkoxy or alkyl radicals is sufficiently high to inhibit these reactions, while Kolbe electrolysis is promoted[60–62]. In the earliest mechanistic studies, it was suggested that the Kolbe reaction was a free radical reaction (i.e. homogeneous solution phase reaction), so without direct involvement of the electrode surface[58,63,64]. However, later studies disproved this free radical theory by using rotation disk electrodes[65] and pulsed electrolysis[66] experiments on Pt anodes to demonstrate that the electrode surface promotes the reaction rate. Only recently, the reaction mechanism of Kolbe electrolysis on Pt anodes has been revisited and it was shown that the above-mentioned critical potential, also referred to as the 'inflection zone,' coincides with a transition between OER at lower potentials to hydrocarbon production (Kolbe reaction) at higher potentials. Moreover, Density-Functional Theory (DFT) calculations demonstrate that decarboxylation and C-C coupling are the likely rate-determining steps in the formation of the Kolbe product[60].

1.4.3. The influence of reaction conditions

As briefly stated before, reaction conditions play an important role in determining the followed reaction pathway and product distribution in electrolysis of carboxylic acids. The experimental parameters that have been identified to impact the reaction outcome include the current density, acid concentration, pH, temperature and pressure, supporting electrolyte, solvent, electrode material and shape and functional groups of the acid[53,62,67–71]. High current densities and increased carboxylate concentration favor the formation of the Kolbe dimer. This is attributed to a high concentration of alkyl radicals at the electrode surface, promoting dimerization[62]. Moreover, high current densities coincide with high oxidation potentials, which are required to overcome the aforementioned critical potential above which Kolbe dimerization proceeds effectively. A weakly acidic/neutral pH seems to be preferable for the production of Kolbe products[47,62]. By adding an alkali metal hydroxide or alkoxide to the electrolyte the concentration of carboxylate anions is increased. During electrolysis, a constant concentration of carboxylate anions is ensured because it is continuously regenerated from the acid by the base formed at the cathode. The dimerization pathway is favored by high pressures and low temperature, likely

because increased pressures facilitate the formation of a lipophilic environment at the electrode surface, hindering water adsorption and disfavoring the formation of carbenium ions. At high temperatures, the integrity of the lipophilic layer is disrupted which reduces the concentration of alkyl radicals at the electrode surface and hence the dimerization rate[68]. The presence of foreign anions also lowers the alkyl radical concentration at the anode by competitive adsorption, and must therefore be excluded from the electrolyte to promote the Kolbe reaction pathway[62,69]. Methanol is the solvent of choice for Kolbe electrolysis as its oxidation is largely suppressed by the formation of the carboxylate layer. Water has been used as well, however with lower yields to the Kolbe dimer due to competitive OER in aqueous media[62]. As anode material, bulk platinum is mostly used to facilitate radical formation[62,70–72]. In non-aqueous media, PbO_2, gold and nonporous graphite can also be used for (non-)Kolbe electrolysis[62]. Finally, the carboxylic acid structure has a significant influence on the reaction outcome as the solubility of the acid in aqueous media differs due to the varying carbon chain length. Additionally, the carbon chain length influences the formation of micelles, typically leading to electrode blocking[53]. Besides the acid chain length, the type of substituent in the α-position of the carboxylic acid plays an important role in determining the yield of the coupling product. Electron withdrawing groups or hydrogen favor the radical dimerization whereas electron donating groups shift the reaction towards the carbenium ion pathway[47]. In summary, to achieve high yields of the dimerized Kolbe-products, high current densities are applied over bulk Pt anodes in an undivided cell containing methanol-based electrolyte with high carboxylate concentration.

1.4.4. Kolbe electrolysis for the conversion of biobased carboxylic acids

Despite the numerous investigations over the past 150 years examining the impact of different reaction parameters and the potential range of substrates, only recently Kolbe and non-Kolbe electrolysis have been revisited and a growing number of studies focus on the required understanding and applicability of Kolbe electrolysis in bio-refineries[47,49,52,53,73,74]. The overall aim is to enhance the performance and increase the economic viability of Kolbe electrolysis. Extensive research on the choice of the anode material has been performed to

avoid the utilization of pure Pt anodes. Thin films of RuO_2 and IrO_2[70], and carbon based anodes such as boron-doped diamond[75] were investigated. However, these materials cannot yet compete with bulk Pt as they are not readily accessible in commercial quantities, have limited scalability and their performance towards Kolbe products is not comparable to that of pure Pt[72]. Besides, the influence of electrolyte composition has been studied and shown to significantly impact the product yield during Kolbe electrolysis. Addition of a supporting electrolyte can improve the performance of electrolysis by enhancing mass transport, however introducing foreign anions can significantly hinder the Kolbe reaction[69]. Regarding the electrolyte pH, contradictory observations and conclusions with respect to stability in performance have been reported. Therefore, a detailed investigation on the electrolyte composition during Kolbe electrolysis is required, also considering product-electrolyte separation during downstream processing. Highly concentrated aqueous solutions of (mixtures of) short and medium chain carboxylic acids have been electrolysed to investigate the implementation of biobased feedstock in electro synthesis refineries[50,53]. Although several studies have shown that (mixtures of) biobased carboxylic acids have the potential to produce drop-in fuel or speciality chemicals via Kolbe electrolysis, controlled conversion of carboxylic acids with high conversion and product selectivity remains challenging. Overall, further research on the electrochemical conversion of carboxylic acids is required to enhance the potential of Kolbe electrolysis for making an important contribution to a circular and biobased viable economy.

1.5. The scope of the thesis

In this dissertation, the electrochemical conversion of carboxylic acids via Kolbe electrolysis (using model compounds) on platinum anodes under various reaction conditions is investigated in detail. The scope of the experimental chapters along with their respective research hypotheses are outlined below.

Chapter 2 discusses the use of low-loading Pt anode for electrochemical decarboxylation (Kolbe electrolysis) of acetic acid. The results support the

hypothesis that differences in surface coverage of the platinized anodes cause variation in performance and electrode stability.

Chapter 3 investigates the electrode surface of bulk Pt anodes during Kolbe electrolysis of acetic acid. The formation of a barrier layer of (adsorbed) acetate on the electrode surface is suggested which suppresses the continuous formation of platinum oxide. Instead under Kolbe conditions active anodic dissolution of Pt was observed, challenging the technical implementation of the use of Pt anodes in Kolbe electrolysis.

In *Chapter 4,* the influence of electrolyte pH on the time dependent product selectivity during Kolbe electrolysis of acetic acid on Pt anodes was studied. In electrolytes with a pH close to the pKa of acetic acid, ethane was selectively produced. However, in alkaline environment, dissolution of CO_2 resulted in a selectivity shift to methanol, which confirms that product distribution in Kolbe electrolysis of acetic acid is strongly pH dependent.

Chapter 5 investigates Kolbe electrolysis of (mixtures of) acetic acid, propionic acid and hexanoic acid on platinum anodes. In line with our hypothesis, the results indicate that differences in adsorption strength resulted in variations in acid conversion, product selectivity and substrate specificity. Using galvanic square waveform pulsing, these performance parameters could be influenced in mixed Kolbe electrolysis of acetic acid and propionic acid.

The final chapter of this dissertation, *Chapter 6,* reflects on the performed research and provides recommendations for further research.

Chapter 2

Electrochemical decarboxylation of acetic acid on platinized anodes with varying surface coverages

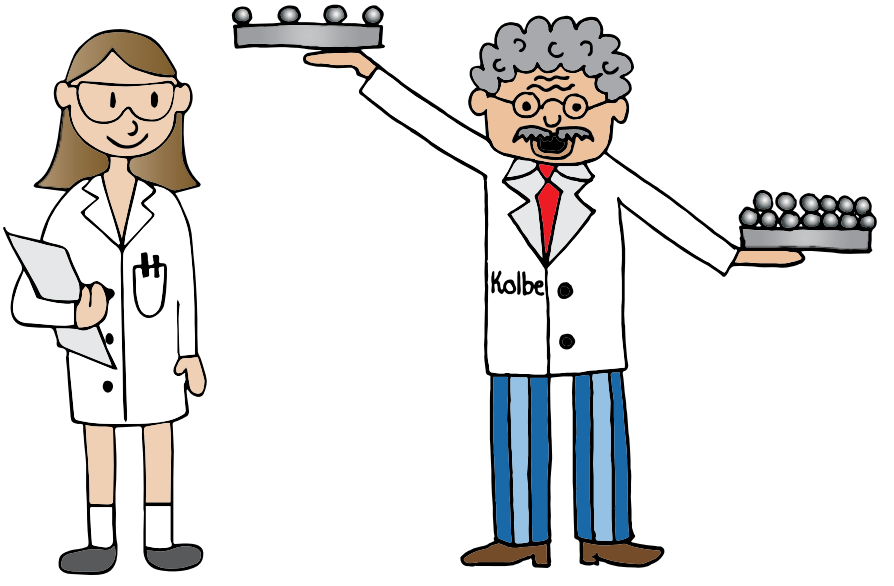

Abstract

Pt anodes with different surface coverages of Pt on Ti and FTO substrates were analyzed for their performance in electrochemical decarboxylation of acetic acid. The results revealed that anodes with low Pt surface coverage do not yield any decarboxylation products, while oxygen evolution and electrode degradation are dominant. With thin films of Pt fully covering the substrates, similar activity to Pt foil was achieved. As Pt dissolution is still significant under the applied process conditions, it must be prevented to enhance the practical feasibility of these anodes in acid decarboxylation.

2.1. Introduction

Existing literature in the last decades on (non-)Kolbe electrolysis typically dealt with understanding of fundamental aspects such as the reaction mechanism and reaction kinetics. Only recently a growing number of studies focuses on the necessary understanding of the effect of process conditions on performance, with the objective to enhance the applicability of electrochemistry, for example in bio-oil upgrading[48,51–53,73,76]. Process conditions include among others reactant concentration[67], reactor configuration[77], applied potential[60] and the electrode material[70,72,78]. Regarding the electrode material, the majority of research in aqueous solutions of carboxylic acids has focused on the use of (bulk) platinum (Pt) to initiate decarboxylation and radical formation. Besides bulk Pt, self-made electrodes consisting of a thin films of RuO_2 and IrO_2[70] have been investigated, as well as carbon based anodes such as boron-doped diamond[75]. Nonetheless, these materials are not readily accessible in commercial quantities, have limited scalability and their performance is not comparable to that of pure Pt. To reduce costs, but not compromise on acid decarboxylation performance, anodes with reduced Pt content have been investigated. Research on platinum-based bimetallic catalysts have been carried out by Yuan et al.[79] who prepared 3D self-supported core–shell Pt@Ir nanoparticles by electrodeposition on porous carbon fiber paper (CFP) as anodes for the electrocatalytic conversion of carboxylic acids to fuel-based hydrocarbons. Qui et al[70]. investigated the electrochemical decarboxylation of valeric acid on drop casted Pt thin films (Pt-TF) and found that Pt-TF were more active for the oxygen evolution reaction (OER) than for Kolbe electrolysis. They ascribed this to structure sensitivity (e.g., particle size effect or a change in surface composition change). To explore this in more depth, the performance of Pt nanoparticles (Pt NP) with different particle sizes for the electrochemical decarboxylation of valeric acid was studied in subsequent work[71]. Similarly, Pt NPs had no apparent decarboxylation activity regardless of the particle size, which they claim was attributed to the formation of an oxide layer that is inactive for the decarboxylation reaction. In contrast to both studies, later work from Yuan et al[78] showed that enhanced activity and stability towards electrocatalytic decarboxylation of n-octanoate was achieved when employing

Pt nanocrystals on CFP in an aqueous solution of n-octanoate. By using different electrodeposition procedures, anodes with different ratios of Pt (100) to Pt (110) were prepared, show-casing differences in product selectivity. Furthermore, a recent study assessed the employment of commercial platinized titanium anodes for the electrochemical conversion of n-hexanoic acid and found a Kolbe performance close to that of pure Pt[72]. Recent work[80] reviewed Pt anodes for Kolbe electrolysis and suggest that electrodeposition and drop casting where the deposition methods of choice for the production of Pt nanoparticles and thin films respectively, producing electrodes with varying surface coverages. Ti foil was mostly used as substrate in aqueous media due to its stability under the applied oxidation potentials[49,70–72]. However, CFP was also employed as it has a high conductivity and large surface area[78,79].

The overview presented above covers the research conducted on low loading Pt anodes and shows that most studies have primarily focused on acid degradation documenting only values for the Current Efficiency. Nevertheless, the influence of surface coverage and substrate material is not yet fully resolved and when comparing the data in various studies, contradictory observations and conclusions with respect to performance have been reported. Therefore, in this work, low loading Pt anodes using different preparation methods on various substrate materials were analyzed for their performance in the electrocatalytic decarboxylation of acetic acid. The results confirmed the hypothesis that substrates with partial surface coverage of Pt show low performance in acid decarboxylation. Moreover, it was demonstrated that continuous Pt dissolution reduces the surface coverage of Pt and hence lowers the activity and stability. Pt dissolution must be prevented by e.g., protective coatings to increase the lifetime of the electrodes and hence enhance the practical feasibility of the use of low loading Pt anodes in Kolbe electrolysis.

2.2. Experimental

2.2.1. Materials and chemicals

Ti foil (0.5mm thick, 99%), Fluorine-doped Tin Oxide (FTO) (Visiontek System, UK), and Platinized titanium mesh (Magneto Special Anodes B.V.) were used as anode material/support. Nitric acid (ACS reagent, 70%), acetone (technical grade, BOOM BV), isopropanol (technical grade, BOOM BV), ethanol (technical grade, BOOM BV) were used for cleaning purposes. Na_2HPO_4 (ACS reagent >99%), H_2PtCl_6 (ACS reagent, >99.9%), acetic acid (glacial, ReagentPlus®, >99%), sodium acetate (ACS reagent, >99.0%) all from Sigma Aldrich, were used as purchased, without purification. Ultrapure water (18.2 $M\Omega cm^{-1}$); home made by a Millipore, Milli-Q Advantage A10 system) was used as the solvent.

2.2.2. Experimental setup

All measurements were performed in a single compartment three electrode glass cell (100 ml) equipped with a working electrode with an area of 0.8 cm^2 (Pt-ED/Ti) or 4 cm^2 (Pt/FTO), a platinized titanium mesh counter electrode (6 cm^2 geometric area) and an Ag/AgCl (3 M NaCl, ProSense) reference electrode (see also Appendix A, Figure A.1a for a schematic representation of the cell), all connected to a Biologic VMP3 Potentiostat. A custom-made Teflon electrode holder was used to cover the backside of the Ti foil to have a defined exposed electrode area. A Teflon electrode clamp (PTFE plated, Pt plate holder, AliExpress) (Appendix A, Figure A.1b) was used to hold the Pt/FTO samples.

2.2.3. Preparation and characterization of low loading anodes

2.2.3.1 Electrodeposited Pt on Ti substrate

Before electrodeposition, the Ti foils were ultra-sonically cleaned in ethanol for 15 min each and were finally rinsed with Milli-Q water. Deposition was performed in a solution of 0.7 M Na_2HPO_4 and 4 mM H_2PtCl_6 and applying -0.4 mA/cm^2 continuously for 15 min.

2.2.3.2. Dewetted Pt on FTO substrate

Pt films were deposited on FTO using a magnetron Sputter Coater (ATC Polaris, AJA International Inc., USA). Pt target (99.99% purity, AJA International Inc.,

USA) and FTO (Visiontek System, UK). The overall resistivity of FTO (25 x 2x 1x1 mm) is 8-10 ohm cm^{-2}. High purity argon (99.999%) was used as the process gas for sputtering. Before Pt sputtering, the FTO substrates were ultra-sonically cleaned in acetone, isopropanol and ethanol for 15 min each and were finally rinsed with Milli-Q water. All the films were deposited at a working pressure of 4.2 x 10^{-6} bar of Ar using 5 W plasma and a RF frequency of 13.56 MHz source (Power source; 0313GTC, T&C Power, USA). Dewetting of as-deposited films was performed in a tube furnace (Carbolite HST12/300) at 500 ºC with a ramp of 10 ºC min^{-1} for the desired duration.

2.2.3.3. Surface characterization of low loading anodes

A Scanning Electron Microscope (SEM) (JSM6010LA, JEOL system) was used to observe the distribution of platinum on the surface of the titanium and FTO substrates.

2.2.4. Electrochemical measurements

Prior to each experiment the glass cell, working and counter electrode were cleaned with 10% nitric acid and Milli-Q water to remove organic residues. The electrolyte was prepared using Milli-Q water, equal amounts of acetic acid and sodium acetate with a total concentration of 1 M and pH of 5. After deoxygenating the freshly prepared electrolyte (70 ml) using 30 ml/min Helium (>5.0), the cyclic voltammograms were recorded using a scan rate of 100 mV/s. Unless mentioned otherwise, the potentials were not corrected for ohmic drop, preventing artefacts caused by overcompensation. If not stated otherwise, results are presented against the RHE scale, calculated according to the following equation:

$$E_{RHE} = E_{Ag/AgCl} + 0.059pH + E^0_{Ag/AgCl} \qquad (2.1)$$

Where $E_{Ag/AgCl}$ is the measured potential and $E^0_{Ag/AgCl}$ is the Ag/AgCl (3M NaCl) reference electrode potential (+0.210 V).

The electrochemical active surface area (ECSA) was estimated by integrating the hydrogen adsorption/desorption portion of the cyclic voltammogram (0 to 0.4 V vs RHE) and dividing this charge by the specific charge of H^+ adsorption on Pt

(210 μC/cm^2). The solution was stirred by a magnetic stirring bar, using a stirring rate of 900 rpm. All experiments were carried out at room temperature.

2.2.5. Product analysis

Gaseous products were analysed by gas chromatography (GC, Interscience CompactGC, the Netherlands). Light gases (H_2, O_2, CO_2) were detected with a ShinCarbon micropacked column (ST 80/100 2m, 0.53mm at 90°C) connected to a thermal conductivity detector (TCD) at 110°C. Hydrocarbons (C1-C4) were detected using a Rt Q BOND PLOT (0.32mm ID, 10μm, 15m, at 60°C) column connected to a flame ionization detector (FID) at 150°C. Gaseous products were collected using a He (5.5) purge at a constant flow rate of 30 mL/min. External calibration was performed individually for the possible products (see Appendix A.2 and A.3). Prior to the measurements, helium was bubbled through the solution to remove air. The Faradaic Efficiency (FE) of the reaction products was calculated using Equation 2.2.

$$FE\ (\%) = \frac{z_i F \Phi_i Q}{I} \cdot 100\% \qquad (2.2)$$

in which z_i is the number of the electrons needed for the formation of product i (-), F is Faraday's constant (96,485 C/mol), Φ_i is the volume fraction of gas i (%), Q is the molar He gas flow rate (mol/s) and I is the applied current (C/s).

2.3. Results and discussion

2.3.1. Electrodeposited Pt on Ti substrate

Platinized titanium samples were produced by electrodepositing Pt on Ti foil. Figure 2.1a shows a representative cyclic voltammogram (CV) of Ti foil and electrodeposited Pt on Ti (Pt-ED/Ti) in 1 M acetic acid buffer.

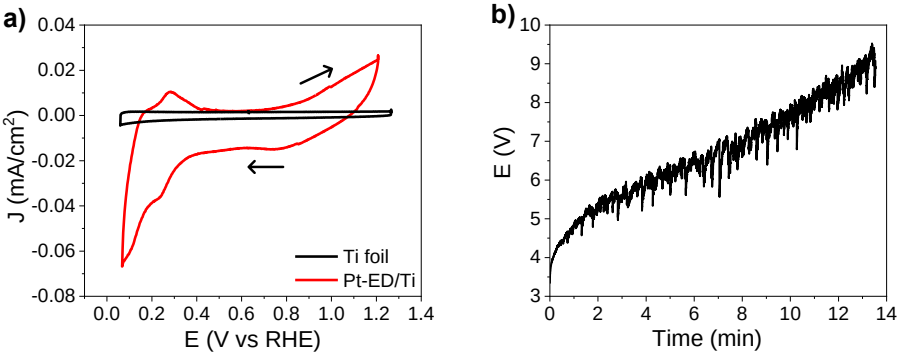

Figure 2.1 a) Cyclic voltammogram of Ti foil (black line) and Pt-ED/Ti (red line) in 1 M acetic acid/sodium acetate solution at pH 5, starting at OCV (~1 V) to 1.25 V back to 0.05 V with a scan rate of 100 mV/s. b) Potential vs. time curve during a constant current experiment at 25 mA/cm² on Pt-ED/Ti in 1 M acetic acid/sodium acetate solution.

When sweeping the potential from open circuit voltage (OCV) (~1 V vs RHE) to 1.25 V vs RHE and back to 0.05 V vs RHE, only little current is drawn in case of the Ti foil. Under anodic conditions, an oxide layer grows on the Ti surface which functions as an insulating layer hampering electron flow. After electrodeposition, Pt particles cover the Ti surface as evidenced by the characteristic features of Pt oxidation and reduction in the CV (E > 1.0 V in the positive scan and 0.6 - 0.9 V in the negative scan respectively) and the relevant hydrogen adsorption/desorption at 0.12 V and 0.22 V that can be assigned to Pt(110) and Pt(100) facets, respectively[81]. The morphology and elemental composition of as-prepared electrodes were studied by SEM and EDX elemental mapping. Figure 2.2a and b show the SEM images of a cracked Ti surface with microstructures of agglomerated 3 µm Pt accumulating in the defects of the Ti substrate. The elemental maps in Figure 2.2c and d show that Pt microstructures

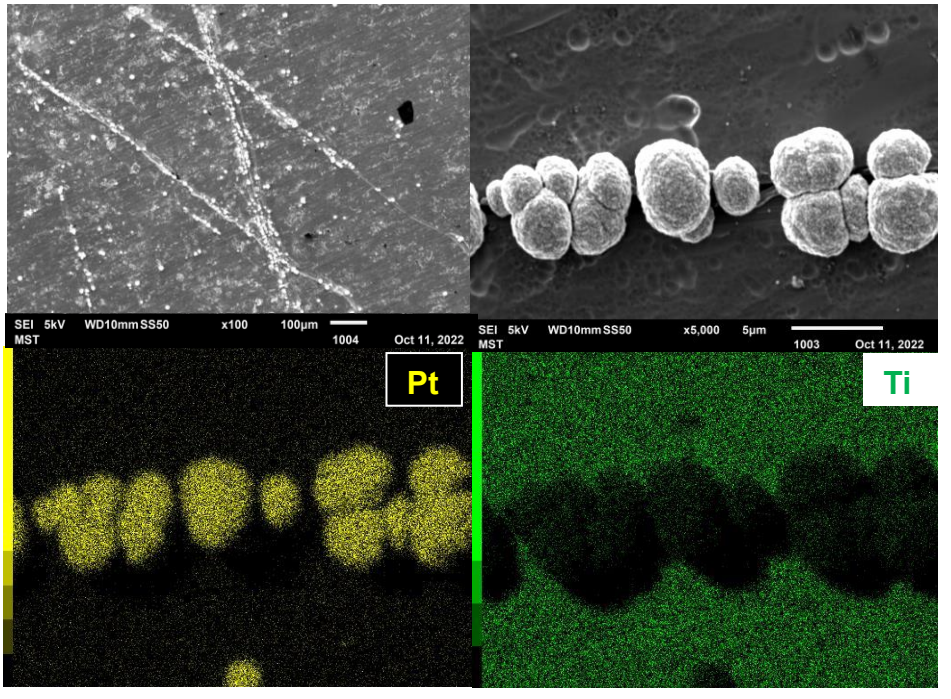

Figure 2.2 a) SEM image of Pt-ED/Ti, with scale bar of 100 µm b) inset of SEM image of Pt-ED/Ti with scale bar 5 µm c, d) EDX mapping of electrodeposited Pt on Ti.

(yellow) are deposited on the Ti substrate (green). From the charge density associated with hydrogen adsorption/desorption derived from the corresponding CV (Figure 2.1a), an ECSA of Pt of 0.06 cm^2 was estimated.

The electrocatalytic decarboxylation of acetic acid was conducted in aqueous solution under a constant current of 25 mA/cm^2. Literature suggests that water oxidation is totally suppressed on Pt by decarboxylation at the given conditions[60,61,82]. However, a gas sample analyzed after the first 10 minutes of constant current showed exclusive production of hydrogen and oxygen from the reduction and oxidation of water, respectively. The absence of ethane and carbon dioxide suggests that decarboxylation of acetic acid did not occur. The activity of Pt-ED/Ti towards water splitting was however short-lived as the electrode was unstable under the given conditions. The E-t curve in Figure 2.1b presents a gradual rise of the measured potential at a constant current, which is attributed to the oxidation of exposed titanium forming a passivating oxide layer. These results are consistent with previous work on Kolbe electrolysis using Pt

microstructures on a Ti substrate as electrocatalyst for valeric acid oxidation[70,71]. The researchers found that electrochemical decarboxylation was negligeable and OER was preferred. Furthermore, an increase in the potential suggested electrode degradation.

2.3.2. Dewetted Pt on FTO substrate

As titanium was unstable under the applied anodic conditions, an alternative substrate material with higher stability was explored. Fluorine-doped tin oxide coated glass (FTO) has been evaluated for its electrochemical stability under both anodic and cathodic polarization conditions and proven to be stable for at least 2 hours at high anodic potentials (up to 2.1 V vs. RHE) in a sodium acetate solution[83]. The electrochemical activity of bare FTO for acid decarboxylation was determined in an aqueous acetic acid electrolyte (see Appendix A, Figure A.4). Under the anodic conditions, exclusive formation of oxygen was observed. A dewetting technique was applied to cover the FTO substrate with Pt agglomerates to have controlled deposition of Pt islands with higher surface area and crystallinity[84]. SEM images of bare FTO, Pt on FTO as deposited (Pt/FTO (AD)), Pt on FTO dewetted for 1 and 24 hours (Pt/FTO (1h) and Pt/FTO (24h) respectively) are shown in Figure A.5 in Appendix A. In case of Pt/FTO (AD), a Pt layer is fully covering the FTO substrate (Figure A.5a). Dewetting resulted in the formation of a structured electrode consisting of nano islands of Pt with an average size of 50 nm (Figure A.5b and c) irrespectively of the dewetting time. Though the surface morphologies obtained by SEM of Pt/FTO (1h) and Pt/FTO (24h) appear to be identical, cyclic voltammetry (Figure 2.3a) suggests that the surface area of Pt/FTO (24h) is slightly higher, but still significantly smaller than the ECSA of the Pt/FTO (AD). The ECSA of the Pt/FTO samples (Table A.5 in Appendix A) were extracted from the CV scans in Figure 2.3a and are roughly 50-100 times larger than that of Pt-ED/Ti. Moreover, changes in the hydrogen desorption region (0 – 0.4 V) indicate exposure of high-index facets for the Pt/FTO (1h) sample, being absent for Pt/FTO (24h) electrodes. In both Pt/FTO (1h) and Pt/FTO (24h), two sharp peaks at ~0.12 and 0.24 V are present corresponding to hydrogen adsorption/desorption on Pt (110), however in Pt/FTO (24h) a third peak at 0.32 V corresponding to hydrogen adsorption on

high-index facets like Pt (553)[85] is missing. This could mean that with extended dewetting time, high-index facets of Pt disappear.

Figure 2.3c shows the Faradaic Efficiency (FE) to ethane and oxygen and the concentration (vol%) of CO_2 over time during a constant current experiment performed at 25 mA/cm^2 in an aqueous acetic acid electrolyte. A high FE to ethane and high vol% to CO_2 indicate that the decarboxylation rate was initially high on Pt/FTO (1h). However, after 90 min of constant current the FE to ethane decreased gradually from ~75% to ~50%. At the same time, an increase in oxygen production was observed. The Pt/FTO (24h) sample initially showed a comparable selectivity towards ethane. However, after 60 minutes, similarly there was a notable shift in FE from ethane to oxygen, which was even more

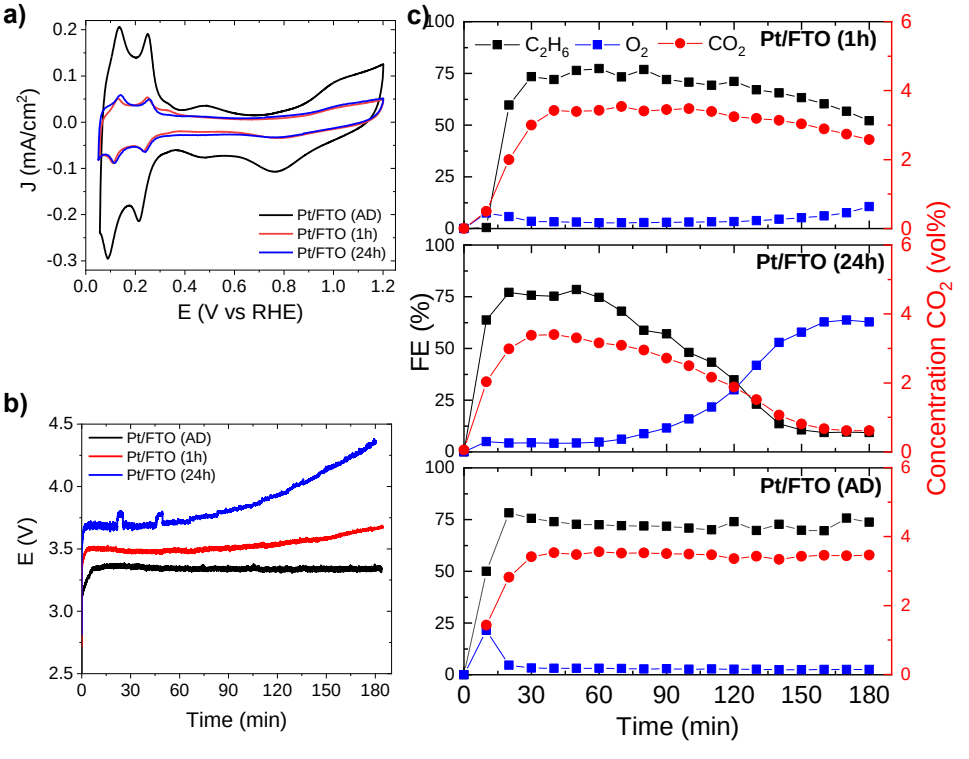

Figure 2.3 a) Cyclic voltammogram of Pt/FTO (AD), Pt/FTO (1h) and Pt/FTO (24h) in 1 M acetic acid/sodium acetate solution pH 5, scan rate: 100 mV/s. b) Potential vs. time curve. c) FE (%) to ethane (black line) and oxygen (blue line) and concentration of CO_2 (red line)(vol%) over time (min) during a constant current of 25 mA/cm^2 on Pt/FTO samples in 1 M acetic acid/sodium acetate solution (pH 5).

prominent than the shift observed in Pt/FTO (1h). Simultaneously with the shift in FE, an increase in potential was noticeable for Pt/FTO (1h) and Pt/FTO (24h) (Figure 2.3b). Only for the Pt/FTO (AD) electrode a stable activity towards acid decarboxylation and Kolbe product formation was observed.

The differences in the time dependent product distribution (Figure 2.3c) could be explained by variations in the surface coverage and stability of the Pt-FTO electrodes. Under the applied conditions, anodic dissolution of Pt occurs[72,86], lowering the surface coverage of Pt and increasing the exposed area of FTO. As FTO is highly selective towards oxygen production in aqueous acetic acid solutions, an increasing share of oxygen in the time dependent product distribution was expected. The higher initial surface coverage of Pt on Pt-FTO (AD) compared to the dewetted Pt-FTO (1h) and Pt-FTO (24h) samples could explain why a decrease in ethane production did not occur for Pt-FTO (AD) within the duration of the experiment. Differences between the dewetted samples could be induced by the possible absence of high-index facets of Pt for Pt-FTO (24h), resulting in lower stability of Pt-FTO (24h). The CV scans (Figure A.6 in Appendix A) show that after the experiment the ESCA had decreased for all samples, which again suggests the dissolution of platinum. In Figure 2.3c it was shown that on a thin film of Pt on FTO, product selectivity was comparable to that of a Pt foil[61,82], making the use of thin films of Pt as a replacement for bulk platinum on a technical scale interesting. However, as Pt dissolution is a persistent issue in Kolbe electrolysis in aqueous media, the stability of Pt thin films will not be competitive to that of bulk Pt foil, which can be considered as an infinite reservoir of electrocatalyst.

2.3.3. Pt thin films on Ti substrates

To elucidate the stability of thin film electrodes further, Pt thin films with different thicknesses (5, 10 and 100 nm) were prepared on a Ti substrate. Figure 2.4a shows the Faradaic efficiency to ethane (%) over time (min) during a constant current experiment at 100 mA/cm² (to approach current densities closer to technical scale).

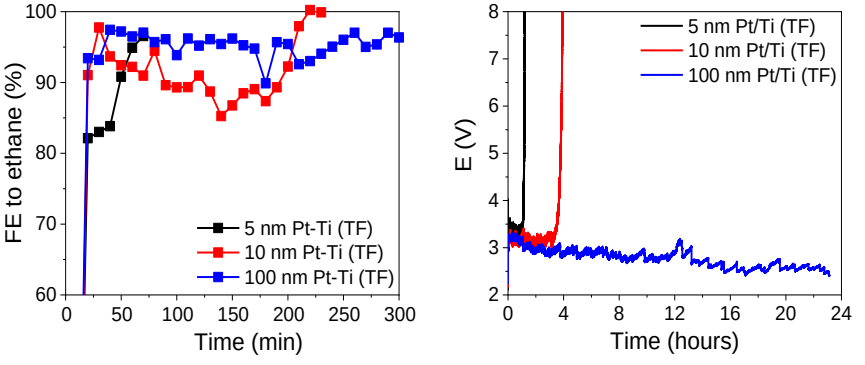

Figure 2.4 a) FE to ethane (%) over time (min) b) Potential vs. time curve during a constant current experiment at 100 mA/cm^2 in 1 M acetic acid/sodium acetate (pH 5) on thin films of Pt on Ti with a thickness of 5, 10 and 100 nm.

Independent of the thickness, all 3 samples were highly selective (FE > 90%) towards ethane production. However, for 5 nm Pt-Ti (TF) after ~1 hour no ethane was detected anymore and simultaneously an exponential increase in the potential (see Figure 2.4b) was observed suggesting the oxidation of the underlying titanium substrate similarly to Pt-Ti (ED) electrodes. With increasing thickness, 10 nm Pt-Ti (TF), an increase in durability to 4 hours of the electrode was determined and for the 100 nm thick layer, the potential remained relatively constant even after 24 hours. As the thickness of the Pt film is much higher, it logically takes longer for the titanium substrate to be exposed during continuous platinum dissolution under the applied conditions. Based on the data in Figure 2.4b a rough estimate of the Pt dissolution rate could be deducted (see Appendix A.7). The Pt dissolution rate seems to be significant under the applied reaction conditions with 1.5 and 2.5 ng s^{-1} cm^{-2} for 5 and 10 nm Pt-Ti (TF) respectively.

In literature, a Pt dissolution rate in the order of some 0.1 ng s^{-1} cm^{-2} was reported during Kolbe electrolysis of acetic acid, which is 15 and 25 times lower. Nevertheless, these values were measured in a non-aqueous electrolyte under lower applied anodic potentials with bulk Pt[86]. The CV scans in Figure A.8a and b in Appendix A show that the ECSA of 5 and 10 nm Pt-Ti had decreased indicating the dissolution of Pt. After the experiment, the ECSA was slightly higher for 100 nm Pt-Ti (Figure A.8c) suggesting surface roughening took place,

which can be considered to occur in a homogenous manner, i.e., layer by layer dissolution, thus without the loss of ECSA.

The results described above demonstrate that the surface coverage of Pt plays an important role in the activity and stability of the electrode. When the surface coverage is low, i.e., for Pt-ED/Ti, decarboxylation does not occur and side reactions like OER and electrode degradation take place. Neubert et al.[72] confirm the importance of the degree of surface coverage. They show that an uncovered surface of as little as 1-3% can already lead to a decrease in decarboxylation efficiency of roughly 50%. Continuous anodic dissolution of Pt poses significant challenges for the implementation of low loading platinum anodes, as it reduces the surface coverage of the electrode, unlike for bulk platinum anodes. However, because of the high costs of bulk platinum, the use of it will not be economically viable and therefore complicates technical implementation of Kolbe electrolysis. Despite having a lower performance, platinized anodes with high substrate coverage, e.g. thin films have shown to be cost-effective[72] especially when platinum dissolution can be avoided as much as possible. In Chapter 6 more attention will be devoted to the challenges of the stability of platinum anodes, and potential solutions will be presented that could enhance the feasibility of these electrodes.

2.4. Conclusions

Kolbe electrolysis of acetic acid on low loading platinum anodes was investigated and the activity and stability were examined. Pt-ED/Ti anodes were inactive for acid decarboxylation due to a low surface coverage of Pt resulting in the oxidation of the exposed Ti substrate. Dewetted Pt on FTO anodes showed high production of ethane but its selectivity dropped over time due to the exposure of FTO leading to enhanced formation of oxygen. Thin films of Pt demonstrated high selectivity for Kolbe electrolysis comparable to that of bulk Pt anodes, however Pt dissolution lowered the stability of these anodes. Pt dissolution must be prevented by e.g., protective coatings to increase the lifetime of the electrodes and hence enhance the practical feasibility of the use of low loading Pt anodes in Kolbe electrolysis.

Chapter 3

Investigating the platinum electrode surface during Kolbe electrolysis of acetic acid

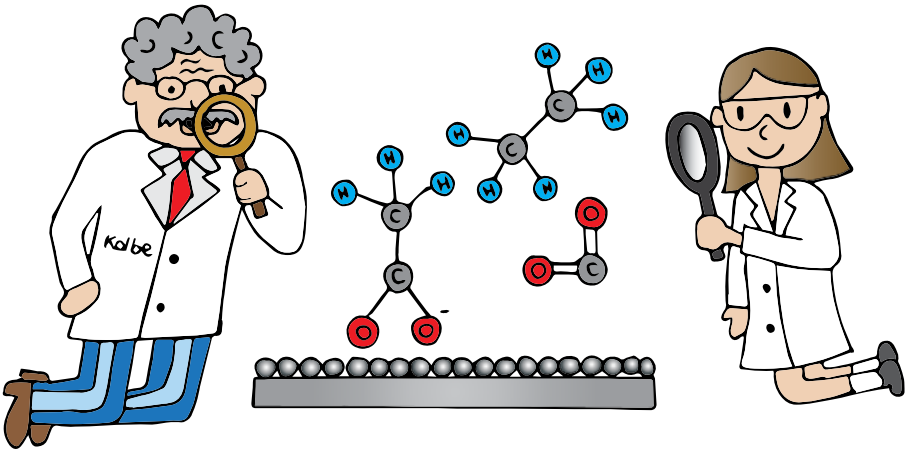

This chapter is based on:

Olde Nordkamp, M., Ashraf, T., Altomare, M., Borca, A. C., Ghigna, P., Priamushko, T., Cherevko, S., Saveleva, V.A., Atzori, C., Minguzzi, A., He, X., Mul, G. & Mei, B. T. (2023). Investigating the Platinum Electrode Surface During Kolbe Electrolysis of Acetic Acid. *Surfaces and Interfaces*, 44, 103684, DOI: 10.1016/j.surfin.2023.103684.

Abstract

Bulk platinum is commonly applied as the anode material for Kolbe electrolysis of carboxylic acids thanks to its superior performance. Literature claims that the formation of a barrier layer on the Pt anode in carboxylic acid electrolyte suppresses the competing oxygen evolution and promotes anodic decarboxylation. In this work, we show by using a combination of complementary *in situ* and *ex situ* surface sensitive techniques, that the presence of acetate ions also prevents the formation of a passive oxide layer on the platinum surface at high anodic potentials. Furthermore, Pt dissolves actively under these conditions, challenging the technical implementation of Kolbe electrolysis. Future studies exploring the activity-structure-stability relation of Pt are required to increase the economic viability of Kolbe electrolysis.

3.1. Introduction

Today's world energy supply and chemical production processes are mainly based on fossil resources like coal, crude oil, and natural gas. The environmental impact of the use of these resources has encouraged researchers to investigate the use of green and sustainable processes to produce synthetic fuels, chemicals and building blocks[36,87–89]. Electrosynthesis is a means to synthesize chemical compounds by utilizing 'green' electrons supplied through solid electrodes, preferably employing the expected surplus of renewable electricity generated by wind and solar installations. Additionally, these processes are often performed at mild reaction conditions, at low pressures and temperatures. Depending on the composition and structure of the electrocatalysts used in the electrochemical reaction, the product yield and selectivity can be tuned. To design improved electrode materials, understanding structure-activity correlations is essential and these have been determined for various electrochemical processes[90–93]. Not surprisingly, the oxygen evolution reaction (OER) is one of the most frequently studied anodic reactions[92,94–96], which is of relevance for water electrolysis, as well as in general for a broad range of electro synthetic reactions performed in aqueous media[97–99]. Using a wide range of operando methods, such as X-ray-based techniques[100,101], isotope labeling[102], Raman spectroscopy[103] and other surface sensitive techniques including Quartz Crystal Microbalance[104], it has been demonstrated that the (electronic) structure of anodes is dynamic under OER conditions. It is thus essential to obtain detailed knowledge of the elemental composition and the crystal structure of the electrode in action[95,105,106]. Compared to the understanding of the function of OER catalysts, significantly less is known about the structure-activity relation in electrochemical organic conversions of biobased platform molecules, such as sugars[107], aldehydes[108] and carboxylic acids[78]. Particularly carboxylic acid conversion via Kolbe electrolysis to hydrocarbons and CO_2[61], (see Figure B.1 in Appendix B) has been revisited recently. Several parameters influence the product yield and selectivity of (non-)Kolbe electrolysis, such as applied current density[62], electrolyte composition[61] and electrode material[75]. Platinum is the electrode material of interest to facilitate radical formation. Early work of

Dickinson and Wynne-Jones[82] showed that platinum electrodes are particularly suitable for Kolbe electrolysis of acetic acid, forming large quantities of ethane, whereas gold and nickel electrodes exclusively formed oxygen. Multiple explanations for the superior electrode activity of platinum exist. Most frequently, the formation of a 'barrier layer' on the surface of the platinum electrode is proposed, which supposedly inhibits the competing oxygen evolution reaction in aqueous electrolyte[60,86,109]. In a study of Lui et al.[60], Density Functional Theory (DFT) calculations were used to demonstrate that CH_3COO^* radicals strongly bind to oxidized Pt surfaces, facilitating C-C bond breaking and consecutive coupling of CH_3^* to ethane. Conway and Vijh[109] showed large Tafel slopes in the high potential region (>2.1 V), indicative for the existence of a barrier-layer type of film on the electrode. Ranninger and coworkers[86] also studied the oxidation of acetate at moderate current densities (<20 mA/cm^2) using Pt electrodes in methanol-based electrolyte using either LiOH and triethylamine (NEt_3) for neutralization, i.e. in the presence of low water content only. They observed cathodic Pt dissolution being slightly suppressed in the presence of water, which was assigned to the formation of Pt-oxides. The formation of Pt-oxides was later confirmed by X-ray Photon Spectroscopy (XPS) after decarboxylation of valeric acid on RuO_2 and Pt nanoparticles[71]. Interestingly, the dissolution rate was affected by the concentration of acetate, assigned to the formation of an adsorbed layer of carboxylate anions. Due to the absence of such a carboxylate-barrier layer on gold and nickel electrodes, these materials are considered inactive for (non-)Kolbe electrolysis[82,110]. Despite the hypotheses on the formation of a barrier layer on Pt anodes, to date a conclusive description of the Pt surface under Kolbe conditions does not exist and the stability of Pt electrodes is not yet explored in detail particularly using aqueous electrolytes. Clearly surface sensitive experimental studies are required to fully disclose the surface structure and stability of platinum electrodes during Kolbe electrolysis.

Therefore, in this chapter we combine classical electrochemical techniques, such as Cyclic Voltammetry (CV) and *in situ* techniques such as electrochemical Quartz Crystal Microbalance (eQCM) and X-ray Absorption Spectroscopy (XAS), to reveal the surface structure of (bulk) Pt anodes during Kolbe electrolysis of

acetic acid in aqueous electrolyte. Cyclic voltammetry measurements, eQCM data and *ex situ* XAS spectra conclusively demonstrate that continuous oxidation of platinum is inhibited by the presence of acetic acid even at high current densities of 100 mA/cm^2 and despite the abundance of water. Using Inductively Coupled Plasma Mass Spectrometry (ICP-MS) active dissolution of platinum was revealed after polarization in aqueous electrolyte at high potential. Thus, this study reveals the complex interplay between acetate ions and water leading only to a partial Pt-oxide formation and active anodic dissolution of Pt which in-turn challenges the technical implementation of Kolbe electrolysis.

3.2. Experimental

3.2.1. Materials and chemicals

Platinum foil (0.025 mm thick, 99.9% pure, Alfa Aesar), platinized titanium mesh (Magneto Special Anodes B.V.) Pt wire (Alpha Aesar, >99,99%) Ti foil, (0.5mm thick, 99%) were used as anode material/support. Nitric acid (ACS reagent, 70%), acetic acid (glacial, ReagentPlus®, >99%), sodium acetate (ACS reagent, >99.0%), perchloric acid (ACS reagent, 70%), sodium perchlorate (ACS reagent >98%) and PtO_2 (≥99.9%) all from Sigma Aldrich were used as purchased, without purification. Ultrapure water (18.2 MΩcm^{-1}); home made by a Millipore, Milli-Q Advantage A10 system) was used as the solvent.

3.2.2. Electrochemical measurements

All measurements were performed in a single compartment three electrode glass cell (100 ml) equipped with a platinum foil working electrode (0.8 cm^2 geometric area), a platinized titanium mesh counter electrode (6 cm^2 geometric area) and an Ag/AgCl (3 M NaCl, ProSense) reference electrode (see also Appendix A, Figure A.1a for a schematic representation of the cell), all connected to a Biologic VMP3 Potentiostat. A custom-made Teflon electrode holder was used to cover the backside of the working electrode and to have a defined exposed electrode area. Prior to each experiment the glass cell, working and counter electrode were cleaned with 10% nitric acid and Milli-Q water to remove organic residues. The electrolyte was prepared using Milli-Q water, acetic acid and/or sodium acetate and/or perchloric acid and/or sodium perchlorate. The blank electrolyte consists of 1 M perchloric acid/sodium perchlorate and the acetic acid electrolyte consist

of 1 M acetic acid/sodium acetate, with in both cases the pH adjusted to 5. After deoxygenating the freshly prepared electrolyte (70 ml) using 30 ml/min Helium (>5.0), the cyclic voltammograms were recorded using a scan rate of 100 mV/s. Unless mentioned otherwise, the potentials were not corrected for ohmic drop, preventing artefacts caused by overcompensation. If not stated otherwise, results are presented against the RHE scale, calculated according to the following equation:

$$E_{RHE} = E_{Ag/AgCl} + 0.059pH + E^0_{Ag/AgCl} \qquad (3.1)$$

Where $E_{Ag/AgCl}$ is the measured potential and $E^0_{Ag/AgCl}$ is the Ag/AgCl (3M NaCl) reference electrode potential (+0.210 V). The solution was stirred by a magnetic stirring bar, using a stirring rate of 900 rpm. All experiments were carried out at room temperature.

3.2.3. Electrochemical Quartz Crystal Microbalance (eQCM)

EQCM experiments were performed using a Gamry eQCM 10M at 5 MHz in a one compartment QCM cell (see Figure B.2 in Appendix B). The sensors were Pt coated Au crystals from Q-sense (Pt film thickness of 300 nm) purchased from Quantum Design GmbH. The sensor was sandwiched between a rubber O-ring and the back contact (the exposed Pt surface area was 0.8 cm^2). A Pt wire was used as counter electrode and Ag/AgCl (3 M NaCl, ProSense) as reference electrode. In each experiment, 7 mL of electrolyte was used. The cell was cooled to 18 °C using a Julabo F12 water bath. Cyclic voltammetry in deoxygenated electrolyte solutions within various potential ranges was used to estimate the thickness of the PtO layer formed during Kolbe electrolysis and reference measurements. The Sauerbrey equation was used to determine the difference in mass from the shift in resonance frequency of the electrode using a calibration constant of 57 Hz cm^2 g^{-1}.

3.2.4. Inductively Coupled Plasma-Mass Spectrometry (ICP-MS)

After polarization of the Pt foil electrode in the single compartment three electrode glass cell (described in section 3.2.2.), the amounts of dissolved Pt in the electrolytes were analyzed by ICP-MS (ICP-MS, PerkinElmer NexION 350×). ICP-MS was calibrated prior to each set of measurements by a four-point

calibration slope prepared from standard solutions that contained ^{195}Pt in a given concentration in either 0.05 M blank electrolyte (perchloric acid/sodium perchlorate) or in 0.05 M acetic acid electrolyte (acetic acid/sodium acetate). While initially both electrolyte solutions had a concentration of 1 M, the samples were diluted 20 times for the ICP-MS analysis. The dilution factor was considered during the analysis of the results. ^{187}Re standard was used as an internal standard. The internal standard solution was prepared in 1% HNO_3 electrolyte and was introduced to the nebulizer of the ICP-MS via a Y-connector.

3.2.5. X-ray absorption spectroscopy (XAS)

X-ray absorption spectra were recorded at the beamline (BM-23) of the European Synchrotron Radiation Facility (ESRF) in Grenoble, France at the platinum L3-edge (11563.7 eV). All scans were normalized with respect to the beam intensity using ATHENA. The pre-edge background was fitted by means of a straight line and the post-edge background by means of a quadratic polynomial. EXAFS data analysis was performed using the EXCURVE code using a k2 weighting scheme. To improve the signal-to-noise ratio (SNR), a spectrum was obtained by averaging 30 scans, each scan having an acquisition time of ~3 minutes. The XAS experiments were performed on thin film (10 nm) platinized titanium samples produced by sputtering. The reference samples, Pt foil and Pt oxide (pelletized from PtO_2) were measured in transmission mode to ensure optimal data quality and to avoid self-absorption. All sample measurements were performed in fluorescence mode with a low grazing incident angle of 5°. A schematic of the XAS cell is provided in Figure B.3 in Appendix B[111]. For *ex situ* XANES, Pt electrodes were polarized in the single compartment three electrode glass cell (described in section 3.2.3).

3.3. Results and discussion

To study the dynamics of the platinum surface under Kolbe and reference electrolyte conditions, cyclic voltammetry was used in a wide potential range (0.05 to 3 V vs RHE). As frequently reported, a steep increase in current, solely related to the oxygen evolution reaction, can be observed starting at ~1.7 V in the absence of acetic acid/acetate electrolyte (Figure 3.1a)[60,61].

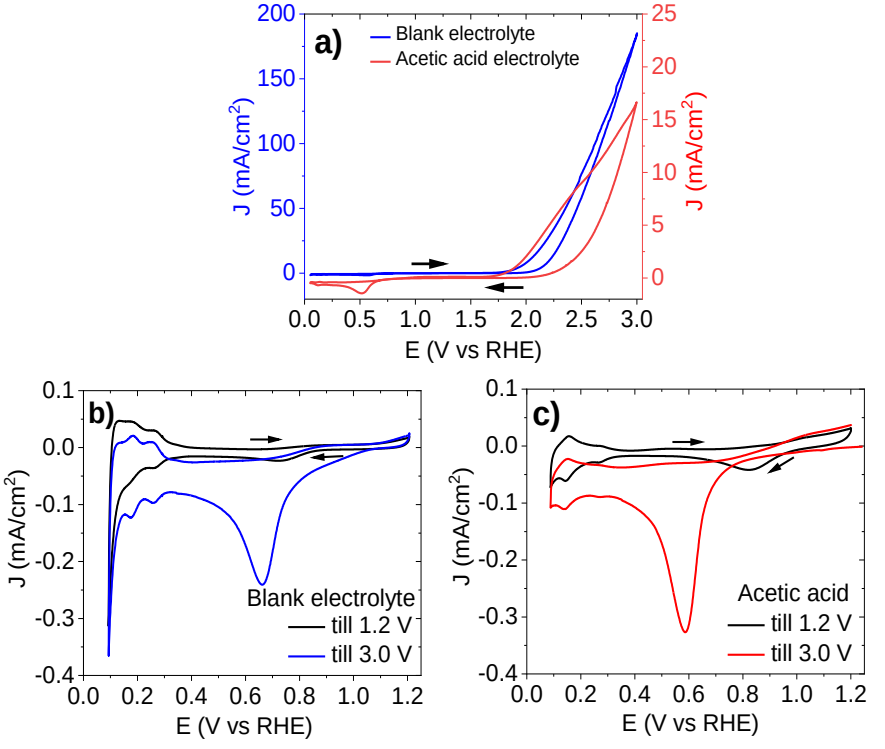

Figure 3.1 Cyclic voltammogram of a) blank electrolyte (blue) and acetic acid electrolyte (red) in high potential window (0.05 – 3 V vs RHE) b) inset of CV in blank electrolyte c) inset of CV in acetic acid electrolyte scanned till 3V and 1.2 V window. Scan rate: 100 mV/s. Arrows show the sweep direction. CV scans were performed in the single compartment three electrode glass cell.

In the presence of carboxylic acids, the onset potential for oxygen evolution reaction is hardly affected, but the current density shows an inflection in the forward scan at approximately 2.2 V, resulting in lower overall currents. This was also observed in previous literature on Kolbe oxidation of valeric acid on Pt anodes[70] and moreover recent work confirmed the selective formation of Kolbe products at potentials >2.2 V vs. RHE[61]. According to literature, subsequent to the formation of a stable PtO layer at potentials >1.2 V[112], a layer of deprotonated acid forms at the surface of the electrode reducing the surface coverage of H_2O and OH^-. This results in an 'inflection zone' apparent at ~2.2 to 2.7 V, which coincides with a transition between OER at lower potentials to hydrocarbon production (Kolbe reaction) at higher potentials[60]. The formation of a platinum oxide layer and its reduction to metallic Pt can be observed for both

electrolytes (Figure 3.1b and 1c), most obviously from the oxide reduction peak minimizing to ~0.7 V for the blank electrolyte, and at ~0.6 V for the acetic acid containing electrolyte, after *prior* increase of the anodic potential to 3 V. When the voltage is limited to 1.2 V in the positive scan direction, the reduction of platinum oxide is largely suppressed (Figure 3.1b and 1c). A shift in the oxide reduction peak can be correlated to the thickness and composition of the formed oxide phase, e.g. PtO_2 or $PtO(OH)_2$ (depending on the pH of the electrolyte) upon polarization at high potentials [113,114].

To gain further insight into the possible structure of the platinum oxide layer formed during polarization at high potentials, additional CV measurements were performed. Now, *prior* to the CV scans, the Pt electrode was polarized using a constant current density of 100 mA/cm^2 for different durations, i.e., to pass different amounts of charge through the Pt electrode (see Figure B.4b in Appendix B for the measured potentials). After polarization, the potential was held at 1.3 V for 30 minutes to remove oxygen generated during polarization from the solution. After preconditioning, the formed platinum oxide film was reduced during a negative potential sweep (see Figure B.5 in Appendix B). The characteristic reduction and oxidation features of Pt seem independent of the specific treatment, however significant differences in the location and the area of the platinum oxide reduction peak (between 0.9 and 0.4 V vs RHE) are noticeable. The integrated charge densities of the Pt oxide reduction peak extracted from the performed CV measurements alongside with the shift in peak position relative to an unpolarized Pt anode are summarized in Figure 3.2. After polarizing the Pt anode in blank electrolyte for 12 s (until 1 C is passed), the platinum oxide reduction peak shifted by ~70 mV in the negative direction compared to the unpolarized electrode (Figure 3.2a). During polarization, metallic platinum is converted to platinum oxide after which adsorbed water molecules are oxidized to oxygen gas. The slight shift of the peak potential in the negative direction and the increased area of 0.85 mC/cm^2 underneath the platinum oxide reduction peak after polarization are thus caused by the growth of an oxide film[115]. If the duration of polarization in blank electrolyte is increased to result in a charge accumulation of 10 C, the shape of the platinum oxide

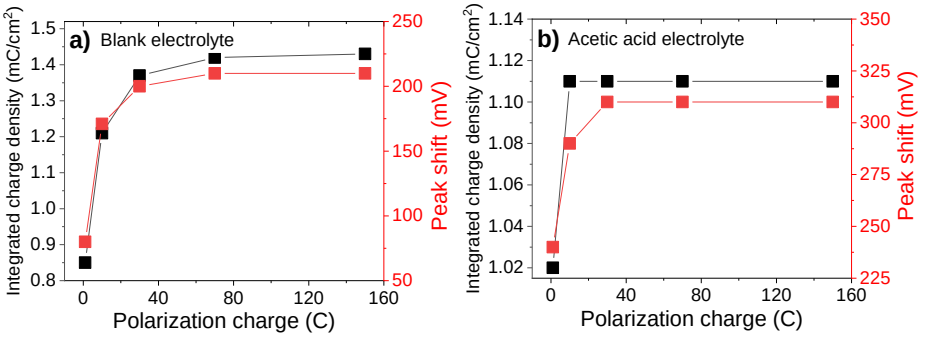

Figure 3.2 Integrated charge density (mC/cm^2) during platinum oxide reduction and the shift of the platinum oxide reduction peak to lower values (mV) relative to the unpolarized electrode after polarizing the platinum electrode at 100 mA/cm^2 in a) blank electrolyte and b) acetic acid electrolyte for different durations (1, 10, 30, 70 and 150 C). The solid lines are drawn to guide the eye.

reduction peak changes from a single reduction event to a superposition of at least two contributions with an integrated charge density of 1.2 mC/cm^2 (see Figure B.5a in Appendix B). Furthermore, a shift in the peak center of ~170 mV is observed. This is shown earlier by Birss et al.[113], suggesting the formation of an oxide layer of $PtO(OH)_2$ with $Pt(OH)_3HSO_4$ after polarization at high anodic potentials in a 0.5 M sulfuric acid solution. Burke and coworkers also showed that platinum oxide films were formed with different compositions after anodic polarization at high potential[116,117]. As such two different forms of platinum oxides are likely observed here. Additional changes in peak area and location of the platinum oxide reduction peak after extended electrolysis were observed for even longer duration experiments. Only after polarization equivalent to 150 C, the peak area and shape of the platinum oxide reduction peak resemble the structure of the sample polarized to 70 C which suggests that a steady composition of the platinum oxide film layer was obtained. After polarizing the platinum electrode in acetic acid electrolyte (until 1 C has passed), already a shift of the platinum oxide reduction peak of ~235 mV (see Figure 3.2b) was observed. The large negative shift of the platinum oxide reduction peak is in contrast to a minor shift observed after polarization in blank electrolyte. Considering that the formation of a barrier layer is widely postulated to occur in acetic acid-containing electrolytes, we assume that the extensive shift is an indication of an adsorbed CH_3COO^- layer. PtO reduction is thus inhibited and

requires that the formed layer on the anode desorbs, before the platinum oxide film is reduced[82,86]. At 10 C, the platinum oxide reduction peak shifts by ~310 mV relative to the unpolarized electrode, after which the position and the area of the platinum oxide reduction peak remain the same (1.11 mC/cm^2) even for extended polarization (150 C). So, the polarization analysis suggests that the formation of the platinum oxide film is independent of the polarization duration once the accumulated charge is larger than 10 C.

To study the formation of the platinum oxide layer in more detail, eQCM measurements were performed to reveal the mass changes associated with platinum oxide reduction after polarization in acetic acid electrolyte. The Pt anode was pre-polarized at constant current density of 5 mA/cm^2 until 1, 10 or 70 C of charge were passed. The lower current density was applied to reduce the risk of electrode roughening, dissolution and delamination and thus damaging the thin Pt layer on the crystal[118,119].

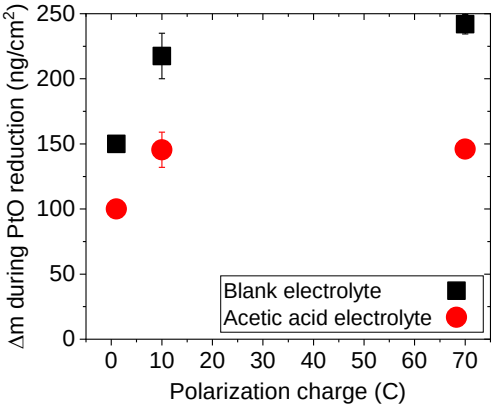

Figure 3.3 Mass decrease (ng/cm^2) during platinum oxide reduction after polarizing the platinum electrode (Pt-covered eQCM crystal with a Pt film thickness of 300 nm) at 5 mA/cm^2 in blank electrolyte (black squares) and acetic acid electrolyte (red circles) for different durations (1, 10 and 70) determined by eQCM. The error margins are based on n=2. Note that the decrease in mass is not related to Pt dissolution but the weight loss associated with the reduction of platinum oxide to Pt. Representative raw data are shown in Figure B.8.

Figure 3.3 displays the mass changes associated with the platinum oxide reduction (between 0.4 and 0.9 V vs. RHE typically) as a function of the polarization duration. CV scans and associated mass changes in blank and acetic acid electrolyte after polarization till 1 C are shown in Appendix B, Figure B.8. It is clearly evident that the mass losses associated with the reduction of the platinum oxide layer are generally lower after polarization in acetic acid electrolyte than in blank electrolyte. This agrees with the overall lower integrated charge density of the platinum oxide reduction peaks obtained for acetic acid electrolyte after polarization (Figure 3.2b). For the blank electrolyte, the mass losses increase as a function of polarization duration. This indicates that the thickness of the platinum oxide layer grows as a function of polarization duration, although the increase seems to stagnate with higher polarization durations. This stagnation was also observed in the integrated charge density of the platinum oxide reduction peak for the blank electrolyte. The reduction of the platinum oxide films formed after polarization to 10 C and 70 C in acetic acid electrolyte result in the same mass loss of ~145 ng/cm^2 (see Figure B.9a and b in Appendix B for reproducibility of mass loss during PtO reduction in blank and acetic acid electrolyte). This is consistent with the independence of the integrated charge densities as a function of polarization duration revealed by analysis of the PtO reduction signal (Figure 3.2b).

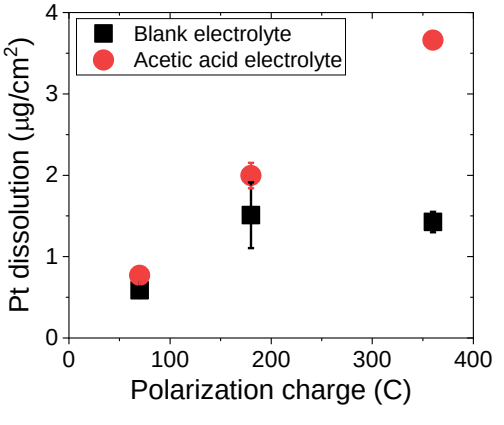

Figure 3.4 Measured Pt concentration (ug/cm^2) in blank (black squares) and acetic acid (red circles) electrolyte after anodic polarization of a Pt foil electrode at 100 mA/cm^2 for different durations (70, 180 and 360). The error margins are based on n=2.

Anodic dissolution of platinum during Kolbe electrolysis was studied using Inductively Coupled Plasma Mass Spectrometry (ICP-MS). After polarization at a constant current density of 100 mA/cm^2 (up to 360 C), the concentration of Pt in the electrolyte was measured (see Figure 3.4). Here, longer polarization durations were required to enable quantification of dissolved platinum in the electrolyte. The dissolution of Pt in acetic acid electrolyte increases linearly with polarization duration whereas the concentration of platinum measured in blank electrolyte initially increases after which it converges to a stable value of ~1.5 µg/cm^2 when the polarization duration exceeds 180 C. Cyclic voltammetry and eQCM data discussed above suggested the formation of a barrier layer consisting of CH_3COO^- anions on the electrode surface which prevents the continuous growth of platinum oxide during polarization in acetic acid electrolyte. Simultaneously, Pt complexation with dissolved acetate anions can occur[120,121], altogether enhancing the dissolution of Pt in acetic acid electrolyte leading to constant (active) Pt dissolution. In the absence of acetic acid, the continuously growing oxide layer passivates the platinum surface, resulting in decreased Pt(O) dissolution, even in aggressive media[120,122].

To complete the analysis of the PtO layer, and dissolution thereof, the electronic structure and structural changes of the platinum oxide layer were analyzed by *ex situ* X-ray absorption spectroscopy. An attempt was made to perform *in situ* X-ray absorption spectroscopy, however due to vigorous gas evolution, the obtained spectra were of poor quality (low S/N). Therefore, polarized Pt electrodes were studied *ex situ* in ambient conditions using X-ray Absorption Near Edge Structure (XANES) and Extended X-ray Absorption Fine Structure (EXAFS) spectra in fluorescence mode, after being removed from the electrolyte. Figure 3.5 shows the XANES spectra obtained after polarization of the Pt anode in acetic acid electrolyte. For comparison, the XANES spectra of Pt foil, PtO_2 reference samples, unpolarized Pt and Pt anode polarized in blank electrolyte are shown as well. When comparing the XANES spectra of the unpolarized Pt electrode with the Pt foil reference spectra, the following changes can be observed: the location of the adsorption edge shifted to higher energy, the white line has a higher peak intensity and a small difference in the post-edge region is

observed for the unpolarized Pt electrode. A strong white-line intensity and the dip in the post-edge region are characteristic spectral features of platinum oxides[123] (see PtO_2 reference spectrum in Figure 3.5), this means that the unpolarized Pt electrode is slightly oxidized compared to the reference Pt foil. Possibly, a thin surface oxide film was already present after preparation of the Pt samples. After polarization in acetic acid electrolyte, no significant additional changes occur to the XANES spectra of the Pt electrode. In agreement with the previous discussion, this implies that the Pt electrode hardly oxidizes after polarization in acetic acid electrolyte. On the contrary, after polarization in blank electrolyte, the white-line peak intensity is more intense, confirming that a significantly thicker platinum oxide layer was formed after polarization in blank electrolyte than in acetic acid electrolyte. This was also confirmed by linear combination fitting of the XANES spectra of the polarized anodes with the Pt foil and PtO_2 reference samples (see Table B.11 in Appendix B). Again, this is consistent with the presented electrochemical analysis and the eQCM data, where an overall higher mass loss during platinum oxide reduction was observed (Figure 3.3).

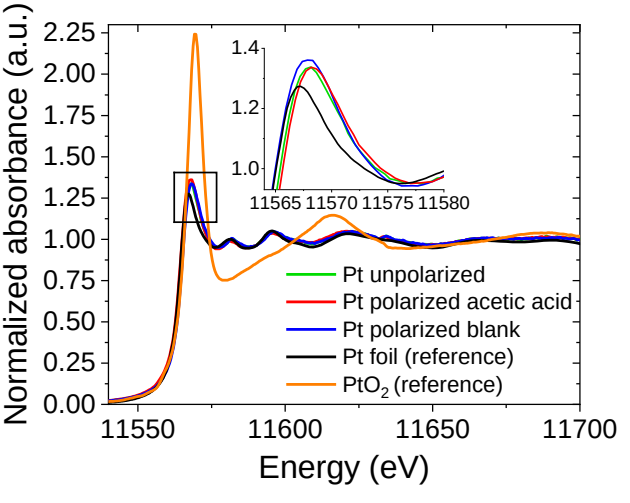

Figure 3.5 Pt L3-edge normalized XANES of a Pt foil reference (black), PtO_2 pellet reference (orange), unpolarized Pt (green), Pt after polarization in acetic acid electrolyte (red), Pt polarized in blank electrolyte (blue). The platinized titanium electrodes were polarized in acetic acid and blank electrolyte at 100 mA/cm^2 until 70 C of charge was reached.

The EXAFS spectra of the polarized Pt electrodes were also recorded to investigate structural changes after polarization at high potentials, however no significant changes could be observed in the phase or amplitude of the EXAFS (see Appendix B.10). This suggests that the structure of the films remains unchanged after polarization and is broadly comparable to that of platinum metal. It is worthwhile noting that EXAFS analysis of the platinum oxide surface was difficult due to the low surface to bulk ratio. This should be increased for a better estimation of the structural changes.

In summary, our novel analytical data confirm that the presence of acetate (acetic acid) inhibits the formation of platinum oxide at high oxidative potentials but stimulates significant active dissolution of Pt (~0.8 ng s^{-1} cm^{-2} in acetic acid electrolyte). In fact, data extrapolation suggests that it will take approximately 310 days until the complete Pt electrode is dissolved under continuous operation (1 cm^2, 0.025 mm thick, 100 mA/cm^2). Thus, for technical implementation of the electrosynthesis reaction, the use of Pt needs to be reconsidered, and the dissolution of platinum during Kolbe electrolysis needs to be studied in more detail[72,86]. In addition, in situ XPS could be employed to further explore the surface structure and composition alongside with the actual oxidation state of the platinum oxide layer under Kolbe conditions.

3.4. Conclusions

Kolbe electrolysis of acetic acid on platinum anodes was investigated confirming the formation of a barrier layer of (adsorbed) acetate on the electrode surface suppressing the continuous formation of platinum oxide. Furthermore, it was shown that dissolution of Pt(oxide) was enhanced by the presence of (adsorbed) acetate. The latter has a negative impact on the practical feasibility of the use of Pt anodes in Kolbe electrolysis. Follow up studies to further explore the oxidation state and dissolution rate of Pt under Kolbe conditions are required to assess the economic viability of electro organic syntheses via Kolbe electrolysis.

Chapter 4

Study on the effect of electrolyte pH during Kolbe electrolysis of acetic acid on Pt anodes

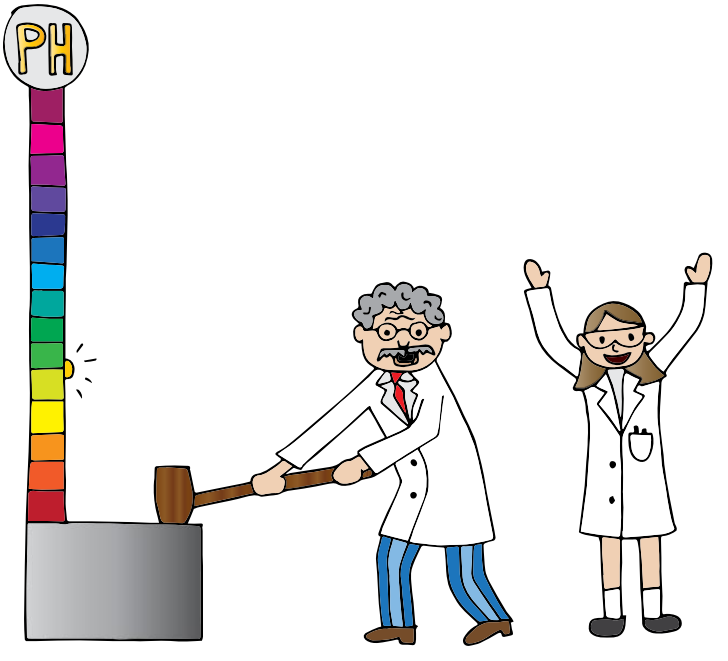

This chapter is based on:

Nordkamp, M. O., Mei, B., Venderbosch, R., & Mul, G. (2022). Study on the Effect of Electrolyte pH during Kolbe Electrolysis of Acetic Acid on Pt Anodes. ChemCatChem, 14(16), DOI: 10.1002/cctc.202200438.

Abstract

In this work, the influence of electrolyte pH is investigated during Kolbe electrolysis of acetic acid. The results demonstrate that reaction selectivity in acetic acid (acetate) oxidation on Pt anodes is determined by the pH and the anionic composition of the electrolyte. Kolbe electrolysis is favoured in electrolytes with a pH similar to, or larger than the pKa of acetic acid, suppressing the formation of O_2 on Pt electrodes. However extended duration of electrolysis of acetate at alkaline pH results in loss of Faradaic Efficiency to ethane, compensated by the formation of methanol. This change in selectivity is likely caused by the dissolution of CO_2 near the electrode-electrolyte interface, resulting in enlarged concentration of bicarbonate/carbonate. On the positively polarized Pt (oxide) surface, these anions seem to inhibit methyl radical conversion to ethane.

4.1. Introduction

Kolbe electrolysis, converting acids into alkanes and CO_2, has been previously proposed in the literature to upgrade bio-oil by lowering the acid content[48,50,52,70,124], while simultaneously producing valuable chemicals. Today a growing number of studies focuses on the necessary understanding of the effect of process conditions on performance, to enhance the applicability of electrochemistry in bio-oil upgrading[48,51–53,73,76]. Specifically, the influence of electrode material[70,72,78] solvent type and reactant concentration[67], reactor configuration[77] and potential[60] are crucial. This is illustrated by, for example Zhang et al.[67] for the conversion of palmitic acid to n-triacontane. Kolbe electrolysis was performed on a platinum electrode using a biphasic solvent system of H_2O/MeOH and petroleum ether. It was shown that at extreme cell voltages above 20 V a yield of 64.7% of n-triacontane was obtained in a basic electrolyte (1.3 M KOH) and at a cell temperature of 55ºC. Besides pure platinum electrodes, platinized titanium electrodes were investigated for the conversion of n-hexanoic acid to n-decane[72]. Qui et al.[70] demonstrated the catalytic activity of RuO_2 and IrO_2 thin films for the conversion of valeric acid. The two latter studies reported promising activity and selectivity to both Kolbe and (non-)Kolbe products, while platinum (e.g. platinum foil) was revealed as the most effective electrode for Kolbe electrolysis. The influence of supporting electrolytes on Kolbe electrolysis of valeric acid was studied by Stang and Harnish[69] revealing that only Na_2SO_4 allows for improved electrolysis performance, whereas addition of nitrate was shown to be detrimental for the Faradaic efficiency (FE) of the Kolbe reaction. This study also suggests that the conversion of valeric acid is independent of the electrolyte pH[69]. Considering that earlier work of Schäfer[62] reports weakly acidic electrolytes to be preferred for Kolbe product formation, whereas Hofer-Moest products are formed primarily at alkaline conditions, the influence of electrolyte composition and pH is not yet fully resolved. A comprehensive overview of the time dependent product formation has not been investigated yet, and comparing the data in various studies, even contradictory observations and conclusions with respect to performance stability have been reported[62,69].

For this reason, this chapter analyses Kolbe electrolysis of acetic acid in more detail with respect to its reaction-time and pH-dependent product selectivity. Specifically, aqueous electrolytes of acetic acid with pH values ranging from pH 2 to 12 were used for the decarboxylation of acetic acid on Pt electrodes. Gas products where continuously monitored in time using gas chromatography, and liquid products were analysed by offline liquid analysis and cyclic voltammetry. The results show that product distribution is strongly pH dependent and product selectivity is changing as a function of reaction time. This can be related to an increasing concentration of carbonate at the liquid-solid interface as a result of the production and dissolution of CO_2.

4.2. Experimental Section

4.2.1. Electrochemical measurements

All measurements were carried out in a single compartment (100 ml) three electrode glass cell equipped with a platinum foil (0.025 mm thick, 99.9% pure, Alfa Aesar) working electrode (1 cm^2 geometric area), a platinized titanium mesh (Magneto Special Anodes B.V.) counter electrode (4 cm^2 geometric area) and an Ag/AgCl (3 M NaCl, ProSense) reference electrode (see Appendix A, Figure A.1) connected to a Biologic VMP3 Potentiostat. Prior to each experiment the glass cell, working and counter electrode were cleaned with 10% nitric acid (ACS reagent, 70%, Sigma Aldrich) and Milli-Q water (18.2 Ωcm) to remove organic residues. The electrolyte was prepared using Milli-Q water (18.2 Ωcm), acetic acid (glacial, ReagentPlus®, ≥99%, Sigma Aldrich) and/or sodium acetate (ACS reagent, ≥99.0%, Sigma Aldrich). The pH of the solution was adjusted by varying the ratio of acetic acid and sodium acetate. If required, the pH was adjusted by the addition of sodium hydroxide (reagent grade, ≥98%, Sigma Aldrich). Generally, the use of supporting electrolyte was avoided because of their negative influence on product yield and selectivity during Kolbe electrolysis[125]. In case of insufficient electrolyte conductivity, sodium perchlorate (ACS reagent, ≥98%, Sigma Aldrich) was added as specified in Table C.1, Appendix C. Unless mentioned otherwise the reported product distribution was obtained by averaging two replicate measurements (n=2, using each time fresh electrolyte solution). Linear scan voltammetry was performed at a scan rate of 10 mV s^{-1},

and cyclic voltammetry was performed at a scan rate of 50 mV s^{-1}. Chronopotentiometric measurements were performed at different currents for a duration of 160 min, while simultaneously measuring gaseous products. The solution resistance was measured using high frequency impedance (ZIR) (Table C.1, Appendix C). Unless mentioned otherwise, the potentials are not corrected for ohmic drop preventing artefacts caused by overcompensation. The solution was stirred using a stirring rate of 900 rpm. All experiments were conducted at room temperature.

4.2.2. Product analysis

Gaseous products were analysed by gas chromatography (GC, Interscience CompactGC, the Netherlands). Light gases (H_2, O_2, CO_2) were detected with a ShinCarbon micropacked column (ST 80/100 2m, 0.53mm at 90°C) connected to a thermal conductivity detector (TCD) at 110°C. Hydrocarbons (C1-C4) were detected using a Rt Q BOND PLOT (0.32mm ID, 10µm, 15m, at 60°C) column connected to a flame ionization detector (FID) at 150°C. Gaseous products were collected using a He (5.5) purge at a constant flow rate of 30 mL/min. External calibration was performed individually for the possible products. Prior to the measurements, helium was bubbled through the solution to remove air. Liquid products were measured by injecting liquid aliquots of the electrolyte into a GC-FID (Agilent). Methanol was detected on a Zebron 7HG-G013-11 (0.25µm ID, 250 µm, 40m) column. The pH of the samples was neutralized and samples were diluted to lower the salt concentration prior to analysis. External calibration curves are shown Appendix A 2.1. and 2.2.

4.2.3. Calculations

If not stated otherwise, experimental potentials are not compensated, and results are presented against the RHE scale, calculated according to Equation 4.1.

$$E_{RHE} = E_{Ag/AgCl} + 0.059pH + E^0_{Ag/AgCl} \quad (4.1)$$

where $E_{Ag/AgCl}$ is the measured potential and $E^0_{Ag/AgCl}$ is the Ag/AgCl (3M NaCl) reference electrode potential. The Faradaic Efficiency (FE) of the reaction products was calculated using Equation 4.2.

$$FE\ (\%) = \frac{z_i F \Phi_i Q}{I} \cdot 100\% \qquad (4.2)$$

in which z_i is the number of the electrons needed for the formation of product *i* (-), *F* is Faraday's constant (96,485 C/mol), Φ_i is the volume fraction of gas *i* (%), *Q* is the molar He gas flow rate (mol/s) and *I* is the applied current (C/s).

4.3. Results and discussion

Using linear sweep voltammetry (LSV) the oxidation of acetic acid was assessed at variable pH (Figure 4.1) (electrolyte composition, measured electrolyte pH and solution resistances are summarized in Table C.1, Appendix C). At pH 2, in acidified perchlorate solution ('blank'), a significant oxidative current is observed at potentials larger than ~1.6 V vs. RHE, typical for oxidation of Pt surfaces, followed by oxygen evolution on Pt oxide. In acetic acid solution at the same pH (pH 2), the current density is significantly smaller, and water oxidation largely suppressed. Despite the significant concentration of acetic acid (1 M $CH_3COOH/NaCH_3COOH$ solutions) only 1% of deprotonated acetate is available at pH 2 (see Equation C1.1 and 1.2 and Figure C.1 in Appendix C) and an inflection zone is not observed. The LSV at pH 4 is quite comparable to the LSV recorded at pH 2, but the oxidative current in the presence of acetic acid is somewhat higher than at pH 2. At pH 5 and pH 9, currents are again lower in the presence of acetic acid/acetate compared to the blank, while now the occurrence of an inflection zone is clearly visible, initiating at ~2.6 V at pH 5 and at ~2.8 V at pH 9 (see inset Figure 4.1c and 4.1d). This is typically explained by a selectivity change from oxygen evolution to the occurrence of the Kolbe reaction[60,126]. Water oxidation now also requires higher potentials (shifting in onset potential from ~1.7 V at pH 2 to ~2.0 V at pH 9, due to a change in the kinetics of water oxidation). Significantly different LSV profiles are obtained at pH 12. Water and Pt oxidation in alkaline chlorate now show a plateau region. This plateau region is also visible in the presence of acetate, while the inflection zone occurs at potentials above 3 V. The determined current-potential curves for acetic acid/acetate are consistent with literature, suggesting adsorption of deprotonated carboxylic acid on the Pt electrode favors subsequent decarboxylation[77,82,127]. To correlate the occurrence of the inflection zone to a

change in the product distribution, the Faradaic efficiency using aqueous solutions of 1 M $CH_3COOH/NaCH_3COO$ at pH 5 are shown in Figure 4.1f.

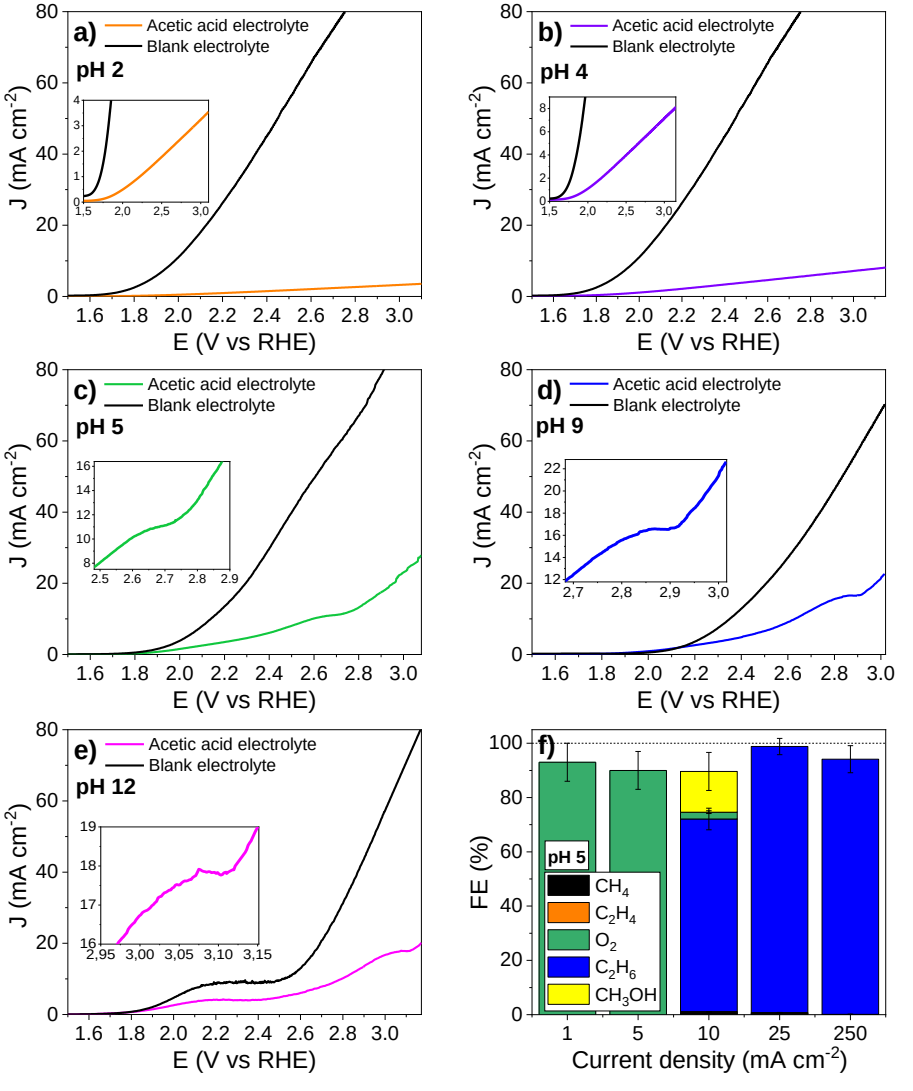

Figure 4.1 Linear sweep voltammogram (LSV) of blank (1 M perchloric acid/ perchlorate) and 1 M acetic acid/acetate at a) pH 2 b) pH 4 c) pH 5 d) pH 9 e) pH 12. LSVs are recorded with scan rate of 10 mV/s at stirring speed of 900 rpm. The potentials are uncompensated. f) Faradaic efficiency to methane, ethylene, oxygen, ethane and methanol obtained for constant current experiments (160 min) using an aqueous acetic acid/acetate electrolyte at pH 5.

For constant current experiments at current densities <10 mA/cm^2, so at voltages lower than ~2.6 V (see Figure C.2 in Appendix C for the measured potentials), oxygen was exclusively formed. Interestingly, for constant current measurements performed at 10 mA/cm^2, i.e., at a potential of 2.7 V vs. RHE, which is within the inflection zone (Figure C.2c), a FE of ~70% towards ethane (the Kolbe product) was obtained, whereas also methanol (Hofer Moest product) was formed. The latter suggests that the concentration of radicals near the electrode surface was not sufficiently high to selectively produce ethane. At current densities of 25 mA.cm^{-2} and higher, at potentials beyond the inflection zone, ethane is formed with very high selectivity (FE > 95%).

To further evaluate the FE at variable pH, chronopotentiometry was applied, while simultaneously measuring the time-dependence of the formed gaseous products by gas chromatography. Due to significant solution resistance in acidic electrolytes, i.e., pH 2 and pH 4, in the absence of supporting electrolyte, chronopotentiometry was first evaluated at constant current densities of 25 mA/cm^2, requiring potentials beyond the inflection zone of > 3 V (see the LSV profiles in Figure 4.1).

Figure 4.2 shows the Faradaic efficiency (%) to methane, ethylene, ethane and oxygen and the measured concentration of CO_2 (vol%) over time (min). For all electrolytes, the selectivity to the products methane and ethylene was negligible (<1%). In acidic media (pH 2) the reaction was selective towards oxygen evolution, and Kolbe products were not detected. At pH 4, the Kolbe products ethane and CO_2 were observed with an ethane FE of ~36%. Based on the absence of an inflection zone in the LSVs due to the low concentration of acetate ions (as shown in Appendix C, Figure C.1 only ~1% and ~8% are deprotonated at pH 2 and pH 4 respectively), a high selectivity towards oxygen evolution was expected for aqueous acetic acid electrolyte with pH 2 and 4[60]. The observed selectivity towards Kolbe products at pH 4 is thus rather surprising. Moreover, mass transport was expected to interfere with Kolbe product formation (see Table C.1, Appendix C for solution resistances), yet even for experiments at pH 4 using unstirred electrolyte (Figure C.3 in Appendix C), a Faradaic efficiency of ~18% to ethane was observed. For electrolytes at

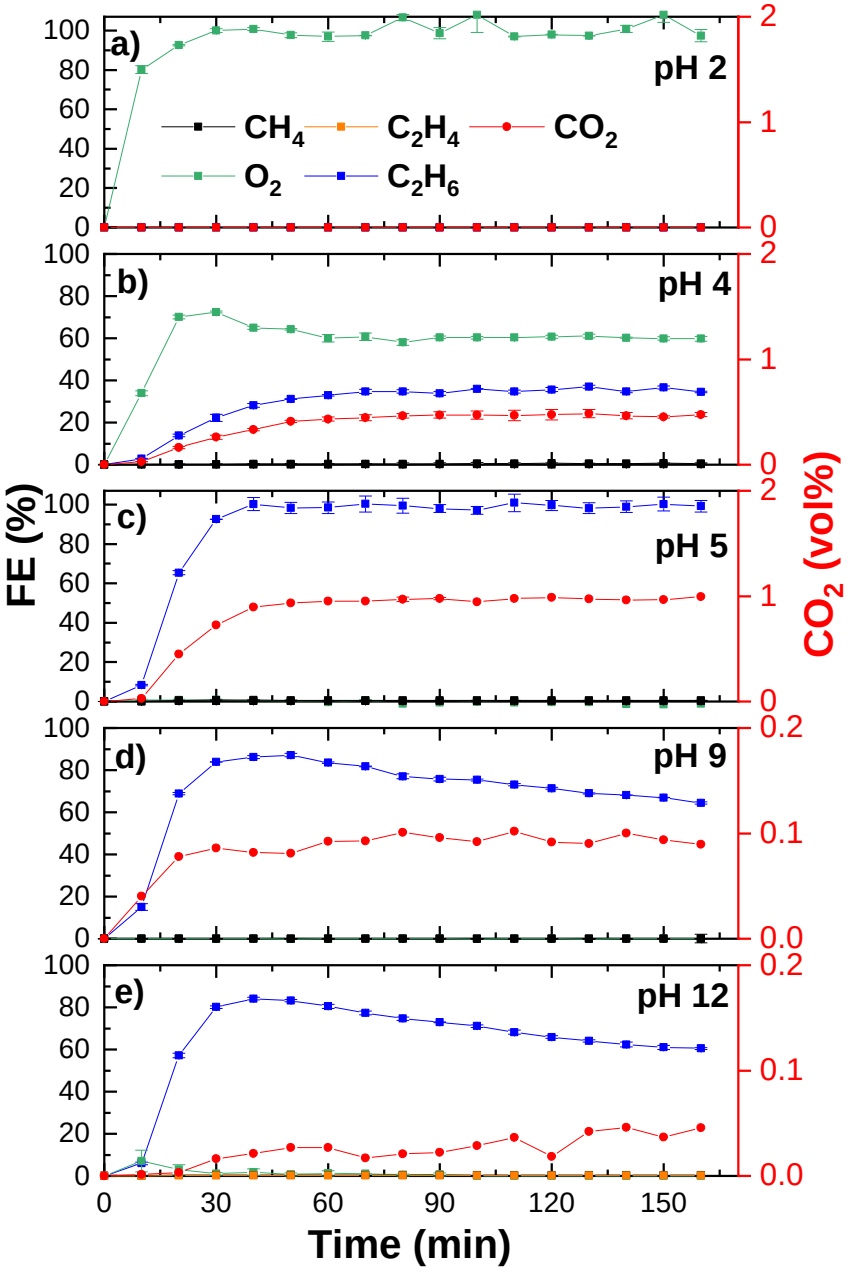

Figure 4.2 FE (%) and CO_2 concentration (vol%) over time during Kolbe electrolysis of aqueous solutions of 1 M acetic acid/acetate at a) pH 2, b) pH 4, c) pH 5, d) pH 9 and e) pH 12. All experiments were performed at 25 mA/cm^2 in a 100 mL undivided cell using a stirring rate of 900 rpm. The gas phase was analysed (measurements taken every 10 min) for methane (black), ethylene (orange), ethane (blue) oxygen (green) and carbon dioxide (red).

intermediate pH (pH 5) the reaction is highly selective towards Kolbe product formation (ethane FE of > 95%) over the entire duration of the measurement. For alkaline electrolyte conditions (pH 9 and 12), the FEs towards ethane show a maximum of ~86 or ~84% at t=30 min, followed by a linear decay to a FE of ~64% and ~60% at t=160 min for pH 9 and 12. It should be noted here that the amount of CO_2 detected in the gas phase, is one order of magnitude smaller (<0.1 vol%) at pH 9 and pH 12, attributed to an extensive capture of CO_2 by the solution. The solubility of CO_2 is pH-dependent and carbonic acid, bicarbonate or carbonate are formed via the carbonate equilibrium (see also equations C4.1, C4.2 and C4.3 in Appendix C4.4). In acidic electrolyte (pH <4.3), carbon dioxide is in equilibrium with carbonic acid, causing a low solubility, while in alkaline solutions, CO_2 is converted to bicarbonate and carbonate ions, leading to extensive absorption in solution. In fact, while starting the measurement at pH 12, a final pH of 9.5 after electrolysis was obtained (see Table C.1 in Appendix C), in agreement with carbon dioxide accumulation in the electrolyte. The data shown in Figure 4.2d and 4.2e seem to suggest that the lowering ethane FE is associated with the formation of bicarbonate/carbonate near the electrolyte/electrode interface. To further strengthen this hypothesis, the electrolyte at pH 12 was purged for 60 minutes with CO_2, followed by a measurement at similar conditions as reported in Figure 4.2e. After presaturation with CO_2, the FE to ethane did not exceed ~70%, not even in the initial stages of the experiment (see Figure C.5 in Appendix C). Besides, a constant current experiment was performed at high current density (250 mA/cm^2) using aqueous solutions of acetic acid/acetate pH 9 containing 0.1 and 0.5 M of sodium bicarbonate (Figure 4.3a and b) to serve as additional evidence for this hypothesis. Figure 4.3a shows that the FE to ethane was significantly lowered in the presence of sodium bicarbonate (~86% for 0 M compared to ~49% and ~5% for 0.1 M and 0.5 M respectively at t=20 min). To analyze the liquid composition of the electrolyte and explain the remaining ~30-35% FE in Figure 4.2d and 4.2e, cyclic voltammetry was performed immediately after chronoamperometry to qualitatively analyze the formed products.

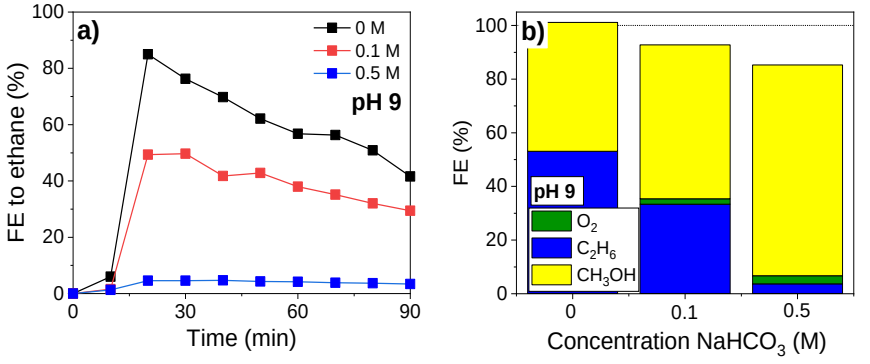

Figure 4.3 a) Faradaic efficiency (%) to ethane over time (min) b) Bar chart of the Faradaic efficiency to oxygen, ethane and methanol during Kolbe electrolysis of aqueous acetic acid/acetate electrolyte at pH 9 with addition of 0, 0.1 and 0.5 M of sodium bicarbonate ($NaHCO_3$) at 250 mA/cm^2. The experiments were performed for 90 min in a 100 mL undivided cell using a stirring rate of 900 rpm.

As shown in Figure 4.4, in the anodic sweep after electrolysis two peaks are observed, which are assigned to the oxidation of methanol[128]. The formation of methanol was confirmed by dedicated measurements using small volume electrochemical cells and subsequent liquid analysis, thereby allowing FE calculations, summarized in Figure C.6 in Appendix C for electrolyte pH 2, 4, 5, 9 and 12 at 25 mA/cm^2.

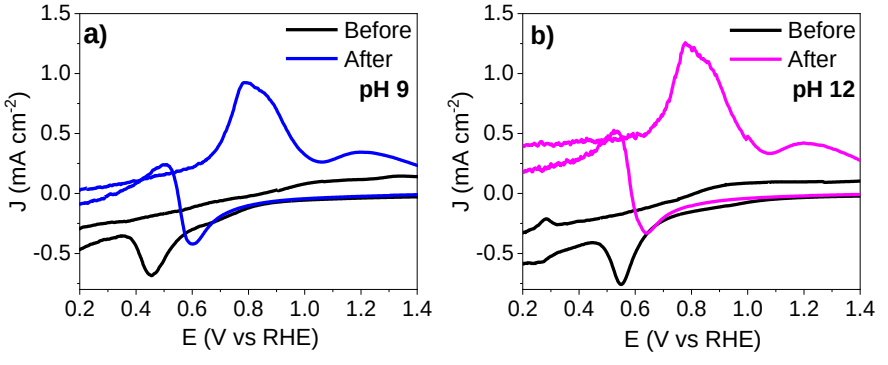

Figure 4.4 Liquid phase analysis using cyclic voltammetry before (black trace) after (colored trace) constant current experiment performed at 25 mA/cm^2 for 160 min using electrolytes with a starting pH of a) pH 9 and b) pH 12.

Liquid analysis (shown in Figure 4.3b) demonstrated that after the constant current experiment of aqueous solutions of acetic acid/acetate pH 9 containing 0, 0.1 and 0.5 M of sodium bicarbonate methanol was obtained. Evidently, the

presence of bicarbonate ions negatively influences the FE to ethane and instead methanol is produced. Importantly, methanol could not be convincingly detected by liquid phases analysis using cyclic voltammetry (Figure C.7 in Appendix C) for measurements performed at 25 mA/cm^2 with electrolytes at pH 2 and pH 4.

Considering these observations, the continuous high selectivity to ethane observed in mildly acidic conditions (pH 5) (Figure 4.2c) is explained by the relatively high availability of deprotonated acetic acid in comparison to pH < 5, and the low solubility of carbon dioxide under these conditions. The pH of the electrolyte is close to the dissociation constant (pKa~4.7) of acetic acid, and equimolar amounts of protonated acid and deprotonated acid are available. The acetate concentration and bulk pH of the electrolyte remain relatively stable during electrolysis because carboxylate ions are in situ regenerated from the carboxylic acid. Additionally, under mildly acidic conditions (pH 5), bicarbonate and carbonate are barely formed (only 22 nanomole/s), and a shift in selectivity from the Kolbe product to the Hofer-Moest product (methanol) does not occur. However, the consumption of acetate ions and conversion of CO_2 to bicarbonate during electrolysis at higher current densities (250 mA/cm^2) and prolonged constant current experiments (300 min) in electrolyte with pH 5 will lead to a reduced buffer capacity and eventually to a shift to high pH. This is demonstrated in Figure C.8 in Appendix C, showing a fast decrease in the measured amounts of ethane and carbon dioxide after passing a charge of 2850 C. The carbon dioxide concentration decreased rapidly from ~10 vol% to ~2 vol% at t=300 min.

Constant current experiments were also performed at 250 mA/cm^2 using other electrolyte compositions (Figure C.9 in Appendix C). For electrolytes with low pH (pH 2 and pH 4), $NaClO_4$ (0.25 M) was now added to decrease the solution resistance. In agreement with the constant current measurements performed at 25 mA/cm^2 (Figure 4.2a and 4.2b), oxygen evolution was dominating. Contrary to Figure 4.2b, at pH 4 oxygen evolution was still favored, however only a minor quantity of carbon dioxide (~0.1 vol%) was detected, even though the potential applied was far beyond the inflection point. This suggests a negative influence of sodium perchlorate on the formation of (non)-Kolbe products. This hypothesis was confirmed by repeating the constant current experiments at pH 4 at 25

mA/cm^2 in the presence of sodium chlorate (compare Figure 4.2b with Figure C.10 in Appendix C). Though formation of CO_2 in small quantities was observed, Kolbe and non-Kolbe products were formed in quantities below the detection limit of cyclic voltammetry and gas/liquid phase analysis, if any. This confirms that at pH 4 chlorate inhibits acetic acid conversion. The chlorate ions have likely disturbed the formation a carboxylate layer and hence (non)-Kolbe products could not be produced. In contrast, Stang and Harnish[69] report that reactant turnover in aqueous solution of valeric acid was not affected by Na_2SO_4 when used as supporting electrolyte. A possible explanation for this is that different anions have a different effect on the product distribution in Kolbe electrolysis[62,129].

In alkaline media (pH 9 and 12) the decrease in FE to ethane (~86% at t=30 min to ~31% at t=160 min) at 250 mA/cm^2 is much steeper compared to the decline in FE to ethane (~86 at t=30 min to ~64% at t=160 min) at 25 mA/cm^2 at pH 9 (see Figure C.10 in Appendix C). This can be explained by the higher CO_2 production rate resulting in faster accumulation of bicarbonate/carbonate near the electrode surface shifting the product selectivity towards methanol. Interestingly, these observations disagree with reports that suggest that Kolbe product formation is promoted at high current densities. This disagreement is likely explained by the extent of carbon dioxide dissolution. Efficient removal of carbon dioxide appears to be mandatory for an extended process operation with high Faradaic efficiency to the Kolbe product.

A change in selectivity from the Kolbe product ethane to the Hofer-Moest product methanol is thus observed at high pH is here attributed to an extensive formation of bicarbonate/carbonate in prolonged experiments. We can only speculate on the origin of the effect of carbonate. It is not unreasonable to assume that carbonate in proximity of the surface of the Pt(O) electrode, will affect the probability of two methyl radicals combining to ethane. Apparently, carbonate favors the formation of methanol. Raman and infrared spectroscopic studies are needed to further evaluate the effect of anions on the electrochemical decarboxylation of acids.

The strong effect of solution pH and associated carbonate formation on performance of (oxidized) Pt in electrolysis of acetic acid/acetate has not been previously reported, also not for other acid/carboxylate combinations. However, when considering the effective use of biomass broadly, it is necessary to investigate whether a selectivity shift also occurs for different carboxylic acids. For example for oxidation of valeric acid the columbic efficiency for reactant conversion was independent of pH[69]. Considering our work, it is likely that a duration-dependent shift in the reaction mechanism will also occur for longer-chain and more complicated carboxylic acids. In practical applications, like in bio-oil upgrading, this suggests that reactors based on continuous flow operation with removal of CO_2 could be effective, to ensure a sustained high selectively to Kolbe products, if desired. Additional research devoted to the influence of pH and current density on product selectivity during Kolbe electrolysis of mixtures of carboxylic acids is needed to reveal the applicability of this research in actual bio-oil upgrading processes.

4.4. Conclusions

Kolbe electrolysis of acetic acid on platinum anodes was investigated and the influence of electrolyte pH on the time dependent product selectivity was revealed. Kolbe products (ethane and carbon dioxide) are selectively produced using electrolytes with a pH similar or larger than the pKa of acetic acid. Yet, in alkaline electrolyte environment (pH 9 and pH 12) selectivity shifted over time to methanol, the Hofer-Moest product. It is highlighted that formation of carbon dioxide and subsequent formation of carbonate and bicarbonate cause the selectivity shift. Thus, based on the presented results, accumulation of CO_2 must be prevented to steer the reaction selectivity to the Kolbe product.

Chapter 5

Substrate specificity and product selectivity in mixed Kolbe electrolysis of short-chain carboxylic acids

This chapter is based on:

Olde Nordkamp, M., Mei, B. & Mul, G. Substrate specificity and product selectivity in mixed Kolbe electrolysis of short-chain carboxylic acids. *In preparation.*

Abstract

Kolbe electrolysis of (mixtures of) C_2, C_3 and C_6 acid on platinum anodes was investigated under classical constant current and galvanic square waveform pulses. Differences in surface interaction were demonstrated by Temkin adsorption isotherms and RRDE experiments, and shown to cause variations in acid conversion, product selectivity and substrate specificity. Using galvanic square waveform pulses, the product selectivity in mixed Kolbe electrolysis of C_2 and C_3 acid could be directed towards ethylene, the product of C_3 oxidation. Combined with methods to reduce the undesired OER, the utilization of galvanic square waveform pulses poses opportunities in enhancing the efficient conversion of bio-derived acids for the production of fuels and chemicals.

5.1. Introduction

In the endeavour of reaching the climate targets set by the European Commission and becoming climate neutral by 2050[130], fossil feedstock has to be replaced by biobased resources for the synthesis of fuels and chemicals. Industrial efforts to optimize the use of biomass-derived carbon are rapidly maturing, resulting in an increased availability of biobased liquids[131,132]. Although research and development have led to advancement in biomass liquefaction technologies[133], the quality of these liquids is still fairly poor and requires upgrading before processing in a refinery is feasible. As large scale traditional upgrading of biobased liquids is energy intensive, these upgrading processes could be well electrified using electrochemical processes to improve bioliquid quality and hence establish a circular and biobased economy[31]. Kolbe electrolysis received increased attention within the last decade for its ability to convert bio-derived acids for the production of fuels and chemicals[47]. Over a period of 150 years, researchers have studied the effect of reaction conditions on electrode performance and screened a broad substrate scope. A vast majority of studies examine electrolyte solutions containing single (complex) carboxylic acids in non-aqueous solvent such as acetonitrile, dimethylformamide or methanol, containing supporting electrolytes like sodium sulphate to increase electrical conductivity[86,134,135]. However, for implementation in refineries using biobased feedstock, highly concentrated aqueous solutions of mixtures of short-chain carboxylic acids, like acetic acid (C_2 acid) and propionic acid (C_3 acid) together representing up to 30% of acid content in bio-oil[136,137] need to be electrolysed.

Levy and Sanderson were one of first to explore the electrochemical oxidation of (mixtures of) short-chain n-alkanoic acids (C_3-C_6) in aqueous media, using Pt electrodes[68,138]. They found that in mixture with hexanoic acid (C_6 acid), electrochemical decarboxylation of C_3 acid resulted in increased yields of the Kolbe dimer product butane, whereas in individual C_3 acid oxidation butane formation did not occur. This was explained using a statistical model to predict the formation of (cross-)coupled products in mixtures of carboxylic acids. This model is based on the integrity of a lipophilic layer with the electrode surface and

shows that improved integrity results in increased yields of coupled products. Later work of Klocke et al.[139], studied the influence of carboxylic acid chain length during anodic decarboxylation of 3-oxanonanoic acid and 3-oxapentadecanoic acid in methanol and also observed increased production of (cross-)coupled products when the carboxylic acid was in mixture with a carboxylic acid with a longer chain length. Likewise, they attributed this phenomenon to enhanced interaction of these acids with the electrode surface. Although both studies discuss the product selectivity in mixtures of carboxylic acids, acid degradation was not examined, and hence information on the substrate specificity in mixtures is missing. More recent work[53] discusses the (hetero-) coupling (of mixtures) of C_4, C_6 and C_8 acids for bio-fuel production purposes, and provide an extensive overview of the product distribution and acid conversion. They show that a delicate balance exists between the need for the formation of a lipophilic layer on the electrode surface as well as relative proximity of the formed radicals at the electrode to effectively form (cross-) coupled products. It was demonstrated that in mixtures of C_4, C_6 and C_8 acid, approximately 60% of the total substrate consumption consisted of C_6 acid. Nevertheless, given that these mixtures consisted of unequal concentrations of these acids, the high substrate specificity for C_6 acid could not be explained solely based on the interaction of this acid with the electrode surface.

While the above studies applied predominantly constant current conditions to evaluate acid decarboxylation, early work has studied the effect of current pulsing during Kolbe electrolysis of C_2 acid to understand the processes occurring at the anode surface leading to dimer formation. They found that the lipophilic layer was affected when a small cathodic current pulse was applied in aqueous acetic acid electrolyte. The negative current destructed the electrode conditions necessary for dimer production, permitting oxygen evolution and thereby reducing reactant conversion[140]. Decades later, Hioki et al.[141] showed that by using rapid alternating polarity instead of classical direct current measurements both product selectivity and reactant conversion could be increased for a wide range of carboxylic acids, including biomass-derived acids. Due to fast polarity switching, local acidification at the electrode surface was

prevented and hence the concentration of deprotonated acid (required for the decarboxylation process) remained high. Up to now, the use of different waveforms for electric current delivery as a means to improve reactivity and selectivity has been discussed for many other synthetic (organic) electrochemical reactions[142–148]. However, the employment of current pulsing was only applied for Kolbe electrolysis of single acid electrolytes, and the influence of the potential waveform during mixed Kolbe electrolysis remains unexplored. Considering that mixtures of acids are available as industrial feedstock, controlling the conversion of carboxylic acids and product selectivity is of relevance for industrial implementation of Kolbe electrolysis as a viable technology to upgrade biobased liquids. Therefore, in this work, we study Kolbe electrolysis of mixtures of short-chain carboxylic acids (C_2, C_3, and C_6) and highlight the effect of galvanic square wave pulse process in steering acid conversion and product selectivity. The results show that changes in product selectivity were observed, which could be explained using Temkin adsorption isotherms of (deprotonated) acids on Pt (oxide) surfaces. Correlation of the isotherms and electrode productivity suggests that carboxylic acids with a higher adsorption strength are dominantly converted over the weaker adsorbing acids. With the use of negative galvanic pulses, the substrate specificity can be even further directed towards the stronger adsorbing acid. Methods to enhance the efficient and selective conversion of bio-derived acids via mixed Kolbe electrolysis are discussed in relation to its economic viability to produce fuels and chemicals.

5.2. Experimental

5.2.1. Materials and chemicals

Platinum foil (0.025 mm thick, 99.9% pure, Alfa Aesar), platinized titanium mesh (Magneto Special Anodes B.V.), and a Pt disc and ring (Metrohm) were used as electrode material in various experiments, respectively. Nitric acid (ACS reagent, 70%), acetic acid (glacial, ReagentPlus®, >99%), sodium acetate (ACS reagent, >99.0%), propionic acid (ACS reagent, ≥99.5%), sodium propionate (≥99.0%), hexanoic acid (≥99%) and sodium hydroxide (reagent grade, >97%) were used as purchased from Sigma Aldrich, without purification. Ethanol (technical grade,

BOOM BV) was used for cleaning purposes. Ultrapure water (18.2 MΩcm^{-1}); home made by a Millipore, Milli-Q Advantage A10 system) was used as the solvent.

5.2.2. Electrochemical measurements

All measurements were performed in a single compartment three electrode glass cell (100 ml) equipped with a platinum foil working electrode (1 cm^2 geometric area), a platinized titanium mesh counter electrode (6 cm^2 geometric area) and a Ag/AgCl (3 M NaCl, ProSense) reference electrode (see also Appendix A, Figure A.1a for a schematic representation of the cell), all connected to a Biologic VMP3 Potentiostat. The whole setup was fabricated to be gas tight, except for two needle ports for gas inlet and gas outlet. Prior to each experiment the glass cell, working, and counter electrode were cleaned with 10% nitric acid and Milli-Q water to remove organic residues. The electrolyte in mixed Kolbe electrolysis experiments always consisted of a total acid concentration of 1 M at pH 5. The acid ratio was varied by adjusting the concentrations of the different acids. In the case of hexanoic acid, a pH of 6-8 was used to avoid two phase separation. After deoxygenating the freshly prepared electrolyte (70 ml) using 30 ml/min Helium (>5.0), electrochemical cleaning was performed using cyclic voltammetry at a scan rate of 200 mV/s after which cyclic voltammograms at 100 and 50 mV/s were recorded. Hereafter, the experiment was carried out under galvanostatic conditions using a current density of 250 mA/cm^2 to ensure we were consistently measuring above the inflection zone were Kolbe electrolysis occurs[61]. After a constant charge of 5000 C had passed, a liquid sample of the electrolyte was collected to measure any liquid products and determine the conversion of C_2 and C_3 acid. Unless mentioned otherwise, potentials were not corrected for ohmic drop, preventing artefacts caused by overcompensation. If not stated otherwise, results are presented against the RHE scale, calculated according to the following equation:

$$E_{RHE} = E_{Ag/AgCl} + 0.059pH + E^0_{Ag/AgCl} \qquad (5.1)$$

Where $E_{Ag/AgCl}$ is the measured potential and $E^0_{Ag/AgCl}$ is the Ag/AgCl (3M NaCl) reference electrode potential (+0.210 V). The solution was stirred by a magnetic

stirring bar, using a stirring rate of 900 rpm. All experiments were carried out at room temperature.

5.2.3. Product analysis

Gaseous products were analysed by gas chromatography (GC, Interscience CompactGC, the Netherlands). Light gases (H_2, O_2, CO_2) were detected with a ShinCarbon micropacked column (ST 80/100 2m, 0.53mm at 90°C) connected to a thermal conductivity detector (TCD) operating at 110°C. Hydrocarbons (C1-C4) were detected using a Rt Q BOND PLOT (0.32mm ID, 10µm, 15m, at 60°C) column connected to a flame ionization detector (FID) operating at 150°C. Gaseous products were collected online every 10 minutes using a He (>5.0) purge at a constant flow rate of 30 mL/min. External calibration was performed individually for the possible products. Prior to the measurements, helium was bubbled through the solution to remove air. Liquid products were measured by injecting liquid aliquots of the electrolyte into a HPLC (Agilent technology 1200 series, Agilent) with a refractive index detector. Acetic acid, propionic acid and ethanol were detected on a Hi-Plex H column which was heated to 65˚C. The mobile phase consists of 5 mM H_2SO_4 solution with a flow of 0.6 mL/min. H_2SO_4 converted the acetate or propionate present in the sample to acetic or propionic acid, which was also detected as such. External calibration curves are shown in Appendix A.2 and A.3. From the measured concentrations acetic or propionic acid, the conversion (in mmoles) was calculated (the volume was assumed to be constant). The Faradaic Efficiency (FE) of the reaction products was calculated using Equation 5.2.

$$FE\ (\%) = \frac{z_i F \Phi_i Q}{I} \cdot 100\% \qquad (5.2)$$

in which z_i is the number of the electrons needed for the formation of product *i* (-), *F* is Faraday's constant (96,485 C/mol), Φ_i is the volume fraction of gas *i* (%), *Q* is the molar He gas flow rate (mol/s) and *I* is the applied current (C/s).

5.2.4. Rotating Ring Disc Electrode (RRDE) experiments

Pt rotating ring disc electrode (RRDE) experiments were performed using a Metrohm Autolab RRDE using a solid Pt disc as working electrode and a Pt ring to detect Pt ring to detect the products of electrochemistry formed at the disc. The counter electrode (CE) was a 2 cm^2 Pt flag electrode. The disc was cleaned with 10% nitric acid and rinsed and sonicated for 10 minutes in Milli-Q to remove organic residues. The collection efficiency of the Pt ring electrodes was determined to be 24% from the data in Appendix D5.1, using $K_4Fe(CN)_6$ (Sigma Aldrich, >99,95%) and KNO_3 (Sigma Aldrich, >99,99%) as redox couple and electrolyte, respectively.

5.2.5. Determination of Temkin adsorption isotherms

A Pt foil (0.8 cm^2) was first cleaned by 10% nitric acid to remove the organics and then rinsed with Millipore water. Prior to the measurements, the three-electrode electrochemical cell was cleaned with 10% nitric acid to remove organics, followed by several series of rinsing with Millipore water. A custom-made Teflon electrode holder was used to cover the backside of the working electrode and to establish a defined exposed electrode area. A platinized titanium mesh was used as the counter electrode and a Ag/AgCl reference electrode was used. The stability of the RE was monitored using a master-RE (Ag/AgCl; 3 M NaCl, BASi). After voltammetric cleaning of the Pt foil, the cyclic voltammograms were measured with 10, 50, and 100 mV/s scan rates to verify the absence of scan rate effects. The 100 mV/s scan rates are presented in this work unless mentioned otherwise. The electrolyte was a 100 mM acetic acid/sodium acetate buffer pH 5. Different concentrations of propionic acid and hexanoic acid were added to the electrolyte, while maintaining a pH of 5. The quantity of underpotentially deposited hydrogen adatoms (H_{upd}) was determined by measuring the charge (the integral of current over time) during the deposition and desorption processes and subtracting the baseline capacitance current. The plotted values represent the charge associated with H_{upd} desorption, which generally matches the H_{upd} charge from adsorption. The adsorption isotherms were determined by fitting the coverages at various concentrations using the Temkin adsorption model, as this model resulted in the best fit[149].

5.2.6. Kolbe electrolysis using galvanic square wave pulses

The pulsed electrolysis experiments were performed in the three-electrode electrochemical cell described above. A Versastat 3 potentiostat galvanostat (Princeton Applied Research) with Versastudio software was used to apply fast galvanic square wave pulses. A 1:1 mixture of C_2 and C_3 acid was used with a total concentration of 1 M and pH 5. After deoxygenating the freshly prepared electrolyte (70 ml) using 30 ml/min Helium (>5.0), electrochemical cleaning was performed using cyclic voltammetry at a scan rate of 200 mV/s after which cyclic voltammograms at 100 and 50 mV/s were recorded. Hereafter, the reaction mixture was electrolyzed under galvanic pulsing conditions for a total duration of 2 hours. The current density of the positive anodic pulse was fixed at 250 mA/cm^2 and the negative galvanic pulse at -1 mA/cm^2. The duration of the anodic pulse was fixed at 200 ms and the duration of the cathodic pulse was varied from 50 – 500 ms. Cyclic voltammograms before and after each experiment were compared to ensure the electrochemical behaviour of Pt did not significantly change because of surface roughening (See Appendix D.5).

5.3. Results and discussion

To evaluate the electrochemical behaviour of the individual carboxylic acids, linear sweep voltammetry (LSV) was conducted using a Pt disc in C_2, C_3 and C_6 acid electrolyte (Figure 5.1) within a RRDE setup. The correspondingly measured ring currents (J_{ring}) are displayed by the dashed lines and can be read against the second y-axis.

Below 1.7 V, no significant disc current (J_{disc}) was observed. However from ~1.7 V, J_{disc} increases for all acid solutions, which can be attributed to the formation of oxygen[60,61]. In C_2 acid electrolyte, J_{disc} reaches a plateau current density of 17 mA/cm^2 at 2.4-2.5 V. This plateau current is referred to as the inflection zone and coincides with a transition between OER at lower potentials to hydrocarbon production (Kolbe reaction) at higher potentials[60].

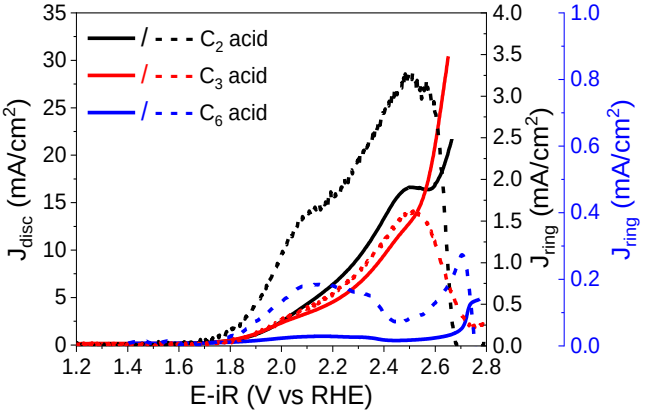

Figure 5.1 Linear sweep voltammogram measured in the RRDE set-up with the electron densities at the Pt disc working electrode (solid lines) and Pt ring detection electrode (dashed lines) at 3000 rpm and 10 mV s^{-1}, E_{ring} +0.1 V vs RHE in 0.5 M C_2 acid and 0.5 M C_3 acid pH 5 and 0.5 M C_6 acid at pH 6-8. The ring currents have been corrected for the collection efficiency and inverted to allow comparison to the J_{disc}.

Although less pronounced, the inflection zone in C_3 electrolyte is visible at approximately 2.5 V. In C_6 electrolyte, an unidentified broad current plateau was observed from ~2.1 to 2.4 V followed by the inflection zone at 2.8 V[150]. The broad current plateau at 2.1-2.4 V is attributed to a change in the kinetics of water oxidation due to the lower buffer capacity of C_6 electrolyte. In line with J_{disc}, J_{ring} also increases from ~1.7 V in all acid solutions, confirming the formation of oxygen. At potentials above the inflection zone, J_{ring} drops to (almost) zero, indicating that oxygen evolution was (completely) suppressed at these high anodic potentials. The strongest increase of J_{ring} was observed for C_2 acid electrolyte reaching a maximum current density of ~3.2 mA/cm^2 at 2.5 V followed by C_3 and C_6 acid (~1.6 mA/cm^2 at 2.5 V and ~0.2 mA/cm^2 at 2.8 V respectively) showing that oxygen evolution is either weakly or strongly suppressed depending on the type of acid interacting with the Pt surface.

To gain a better understanding of the interaction of these acids with the Pt surface, the adsorption isotherms were determined via a cyclic voltammetry method (CV)[149]. The adsorption isotherms can provide information about the adsorption strength of the individual acids and predict the substrate specificity and product selectivity of the acid in mixtures. Figure 5.2a shows the hydrogen

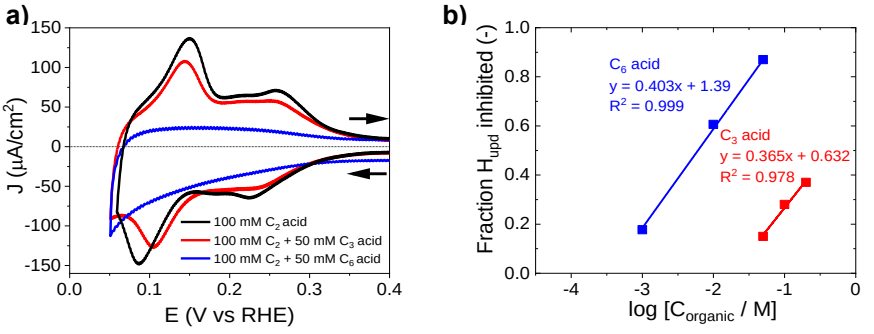

Figure 5.2 Cyclic voltammograms showing hydrogen underpotential deposition for a) 50 mM C_3 acid and 50 mM C_6 acid in 100 mM C_2 acid buffer at 100 mV/s at room temperature. b) Temkin adsorption isotherm of C_3 acid and C_6 acid in C_2 acid buffer, extracted from data in Appendix D, Figure D.2a and D.2b

underpotential deposition adsorption/removal region of a cyclic voltammogram (CV) of Pt in a C_2 acid buffer (100 mM) with 50 mM of C_3 acid or C_6 acid. A buffer of C_2 acid was used as reference solution to exclude the introduction of foreign anions as well as to maintain a stable concentration of deprotonated carboxylic acid. Hydrogen adsorption and desorption on the different facets of Pt can be observed by two peaks at ~0.25 and ~0.1 V when sweeping towards negative potentials and two peaks at ~0.05 and 0.2 V when sweeping towards positive potentials respectively for the C_2 acid buffer[151,152]. The current associated with hydrogen underpotential deposition (H_{upd}) is proportional to the amount of hydrogen deposited on the metal or removed from its surface and can therefore be used to measure the fraction of H sites that are blocked by the adsorption of organic molecules present in solution[149]. When C_3 was added to the C_2 acid buffer, the peaks of hydrogen adsorption and desorption decrease. This agrees well with reports on Pt in acidic media and in the presence of other organic molecules such as phenol, showing that H_{upd} is inhibited on different facets of Pt[149,153]. With the addition of C_6 acid, the peak currents almost completely vanish, showing that the inhibition of hydrogen adsorption is even stronger for C_6 acid compared to C_3 acid. Figure D.2a and D.2b in Appendix D show the hydrogen underpotential deposition adsorption/removal region of the CV for Pt using different concentrations of C_3 acid and C_6 acid in C_2 acid buffer, respectively. Integrating the H_{upd} current obtained in C_3 and C_6 acid electrolyte allows to determine the total charge, i.e., the concentration of adsorbed

hydrogen. This can be compared to the H_{upd} charge of a Pt surface in the C_2 acid buffer to estimate the fraction of H_{upd} that was inhibited by the presence of C_3 acid and C_6 acid molecules. Figure 5.2b shows the fraction of H_{upd} inhibited vs. the logarithmic concentration of C_3 and C_6 acid. A linear fit was made through the data points yielding the Temkin adsorption isotherms for C_3 and C_6 acid in C_2 acid buffer. The slopes (α) provide information on the Temkin constants, which are related to the heat of adsorption of the carboxylic acids[154]. A higher α =0.403 for C_6 acid, and hence higher heat of adsorption indicates a stronger interaction of C_6 acid with the platinum electrode surface compared to C_3 acid (α = 0.365). As a reference, the adsorption isotherm of C_2 acid was given in Figure D.2c in Appendix D, and demonstrates an even weaker interaction (α = 0.08) with a Pt electrode surface[155].

To determine product selectivity and substrate specificity in (mixtures of) C_2, C_3 and C_6 acid, chronopotentiometry was applied while simultaneously measuring the formed gaseous products. Liquid products were measured offline at the end of the experiment.

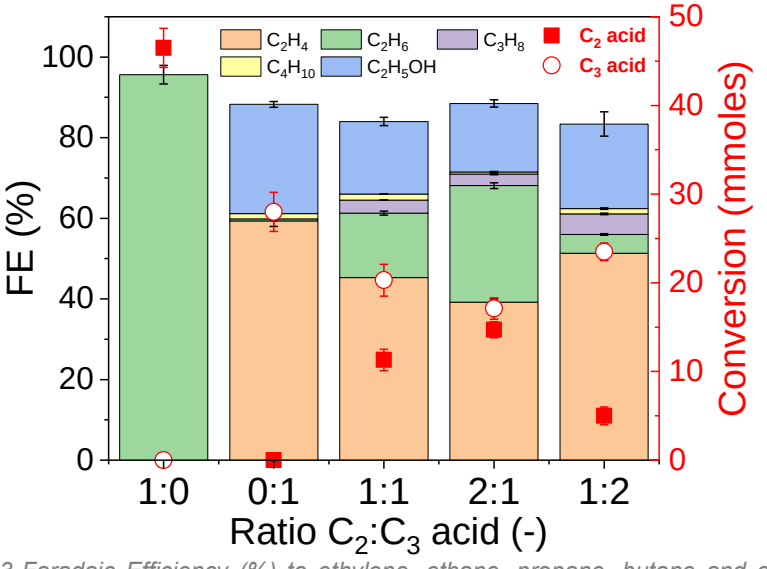

Figure 5.3 Faradaic Efficiency (%) to ethylene, ethane, propane, butane and ethanol during Kolbe electrolysis of mixtures of acetic acid (C_2) and propionic acid (C_3) with different ratios. The second y-axis shows the conversion (in mmoles) of C_2 acid (circle) and C_3 acid (square) after 5000 C of charge passed. The electrolyte pH was close to pkA of both acids (pH ~5), the total acid concentration was 1 M and the applied current density was 250 mA/cm^2. The error margins are based on N=2.

Figure 5.3 shows the Faradaic Efficiency (%) towards the different reaction products and the conversion (mmoles) of C_2 and C_3 acid after electrolysis at 250 mA/cm^2 using mixtures with different C_2 to C_3 acid ratios. After electrolysis in pure C_2 acid electrolyte, the Kolbe dimer ethane was exclusively formed. After the experiments, approximately 47 mmoles of C_2 acid was converted. As the maximum possible conversion was 51 mmoles (calculated by dividing the transferred charge by the Faraday constant and number of electrons required for acid decarboxylation), the electrons were selectivity used for C_2 acid decarboxylation (~92%), which is in agreement with previous literature on Kolbe electrolysis of C_2 acid[60,61,82]. For C_3 acid electrolyte, the main products formed were ethylene and ethanol, with a FE of ~60% and ~27% respectively. These results are also in agreement with previous work on Kolbe electrolysis of C_3 acid oxidation obtaining a product yield of 61% and 31% towards ethylene and ethanol respectively in a 2 M C_3 acid electrolyte with similar pH[138]. Other minor products formed were ethane, butane and ethyl propionate. Alternative reaction processes like the oxidation of ethanol to carbon dioxide and formation of hydrogen peroxide via water oxidation could occur and explain why the total FE does not sum up to 100%. With 28 mmoles, the conversion of C_3 acid however was much lower compared to C_2 acid. Differences in conversion of C_3 acid arise from the reaction mechanism yielding primarily products generated via a two-electron pathway, whereas for C_2 acid oxidation, product formation usually requires one electron to be transferred per C_2 molecule converted. When a 1:1 mixture of C_2 and C_3 acid was electrolyzed, the main products were ethylene and ethanol (with a total FE of ~64%), while ethane was formed with a FE of 16%. Additionally, the conversion of C_3 acid was higher (21 mmoles) than that of C_2 acid (11 mmoles). This shows that conversion of C_3 acid was preferred over C_2 acid conversion. Even for electrolytes containing an excess of C_2 acid (ratio C_2:C_3 = 2:1), C_3 acid was still favourably oxidized over C_2 acid. This becomes evident from a high contribution of ethylene and ethanol (total FE: 56%) in the product composition and a slightly higher conversion of C_3 compared to C_2 acid (17 mmoles vs. 15 mmoles). The high substrate specificity for C_3 acid in mixtures with C_2 acid is likely attributed to the higher adsorption strength of the acid. To verify this hypothesis, mixtures of C_3 and C_6 acid (having an even higher

adsorption strength than C_3 acid, see Figure 5.2) were electrolysed to study the product selectivity and substrate specificity of C_3 acid. Figure 5.4 shows the conversion of C_3 acid and the yield% towards the C_3 acid reaction products after Kolbe electrolysis of mixtures of C_3 and C_6 acid with different ratios.

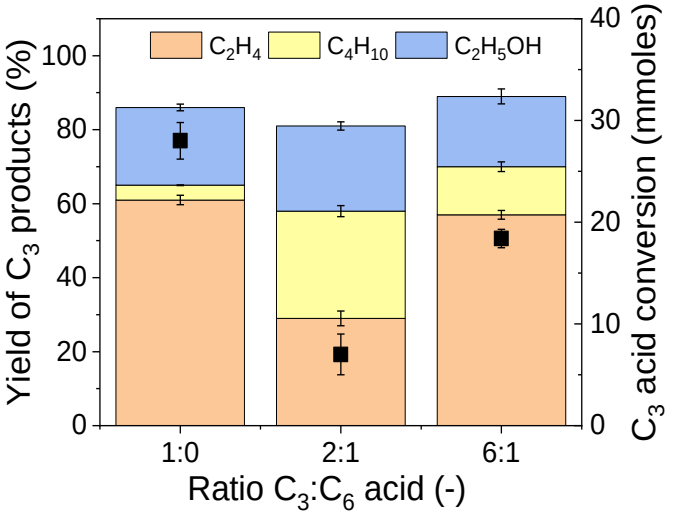

Figure 5.4 Faradaic Efficiency (%) to ethylene, butane, ethanol and other products during Kolbe electrolysis of mixtures of propionic acid (C_3) and hexanoic acid (C_6) with different ratios. The second y-axis shows the conversion (in mmoles) of propionic acid (black squares) after 5000 C of charge passed. The electrolyte pH was maintained between pH 6-8, the total acid concentration was 1 M and the applied current density was 250 mA/cm^2. The error margins are based on N=2.

In a 2:1 mixture of C_3 and C_6 acid, the total yield towards ethylene and ethanol (52%) is significantly lower compared to pure C_3 acid electrolyte (82%). Furthermore, the conversion of C_3 acid decreased by a factor of four from 28 mmol to 7 mmoles, most likely at the expense of C_6 acid conversion as oxygen (formed via competitive water oxidation) was not detected. A quantitative analysis of the oxidation products of C_6 acid was not possible due to shortcomings in our analytics but in theory involve n-pentane, pentene, n-decane, pentanol, n-hexanoic acid-2-pentyl ester, n-hexanoic acid pentyl ester[72]. Cross-coupled products like n-heptane, or cross coupled esters n-hexanoic acid-2-ethyl ester, n-hexanoic acid ethyl ester and n-ethyl-2-pentyl esters could also be formed[138]. In a 6:1 excess of C_3 acid, the conversion of C_3 acid is still fairly low (18 mmoles) in comparison to pure C_3 acid electrolyte.

These results show that in mixtures of C_3 and C_6 acid, C_6 acid strongly supresses the oxidation of C_3 acid. Furthermore, the presence of C_6 acid changes the C_3 acid product distribution by increasing the product yield of butane from 4% to 29% (2:1) and 13% (6:1) being consistent with the work of Levy and Sanderson[138].

It is demonstrated that differences in conversion and product selectivity can be assigned to differences in the adsorption strength of C_2, C_3 and C_6 acid. The conversion of C_3 acid in a C_3 and C_6 acid mixture could be estimated using the adsorption data presented in Figure 5.2b demonstrating that the fraction of H_{upd} inhibited in C_6 acid at a logarithmic concentration of -1.3 was about 6 times higher than the fraction of H_{upd} inhibited in C_3 acid at the same concentration (0.87 vs 0.15). If we assume that the acid conversion solely depends on the adsorption strength of the acid, then a 6 times higher conversion of C_6 acid over C_3 acid was expected in an equal mixture (1:1) of C_3 and C_6 acid. However, in a 2:1 and 6:1 mixture of C_3 and C_6 acid, the conversion of C_6 acid over C_3 acid was expected to be only 3 and 0.96-fold higher. Considering a C_3 acid conversion of 28 mmoles in pure C_3 acid electrolyte, this resulted in an estimated C_3 acid conversion of 7 and 14 mmoles for a 2:1 and 6:1 C_3:C_6 acid mixture respectively, being close to the actual measured C_3 acid conversion (7 and 18 mmoles for 2:1 and 6:1 C_3:C_6 acid ratio, respectively). Deviations between the estimated C_3 acid conversion and the actual C_3 acid conversion can be explained by variations in the product selectivity of C_3 acid oxidation (e.g. increased production of butane via a single electron pathway in the presence of C_6 acid). Overall, the data shows that acids with a higher adsorption strength are favourably oxidized over the weaker adsorbing acids, consequently leading to higher conversion and a larger proportion of oxidation products of this acid in the total product distribution.

To examine if product selectivity and substrate specificity in mixed Kolbe electrolysis can be manipulated, galvanic square waveform pulses were applied in mixtures of C_2 and C_3 acid. Mixtures including C_6 acid were excluded from this dataset as C_6 acid conversion and C_6 oxidation products could not be quantified with the required time resolution. During galvanic square waveform pulsed experiments, a positive current pulse (J_a = 250 mA/cm^2) with a fixed duration (t_a)

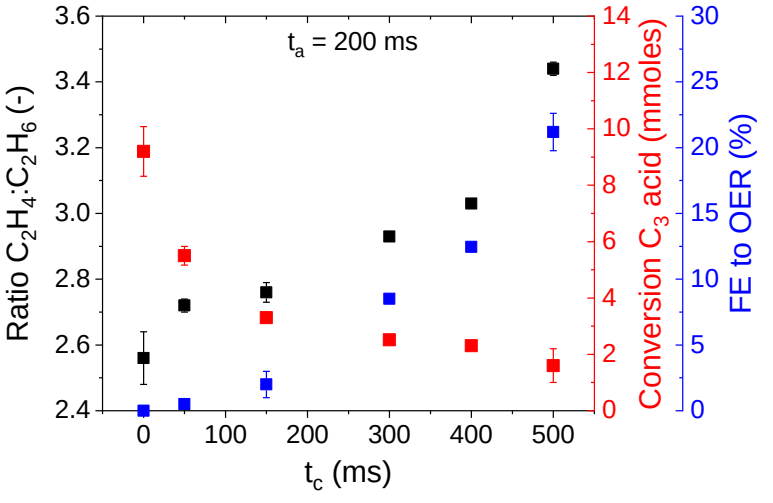

Figure 5.5 Ratio between ethylene and ethane during alternate anodic and cathodic pulses with different pulse durations in Kolbe electrolysis of a 1:1 mixture of C_2 and C_3 acid (1M, pH 5). The second and third y-axis show the conversion (in mmoles) of C_3 acid (red) after 2 hours and FE to oxygen evolution. The anodic pulse was fixed at 250 mA/cm^2 with a duration of 200 ms. The error margins are based on N=2.

was alternated with a slightly negative current pulse (J_c = -1 mA/cm^2) with varying durations (t_c) (See Figure D.3 in Appendix D for a schematic representation). Figure 5.5 shows the ratio of C_2H_4 and C_2H_6 (the major products of Kolbe oxidation of C_3 and C_2 acid respectively) as a function of the cathodic pulse length (t_c)(ms). The second and third y-axis display the conversion of C_3 acid (in mmoles) after 2 hours and the FE to O_2, respectively. The anodic pulse duration (t_a) was fixed at 200 ms. Under constant current conditions (t_c = 0), a C_2H_4:C_2H_6 ratio of 2.5 was obtained. When a cathodic pulse was applied, this ratio increased with extended duration, to a maximum value of ~3.5 at t_c = 500 ms. Variances in the composition of the adsorbed layer on the platinum (oxide) surface and changes in the double layer structure may explain this behaviour. During a negative current pulse, carboxylate anions will desorb and the double layer structure is rearranged. The quantity of desorbed carboxylate anions strongly depends on the cathodic pulse duration (t_c), and hence on the amount of passed cathodic charge (Q_c). When Q_c increases, a larger portion of the adsorbed carboxylate anions will desorb. Given that C_3 acid adsorbs stronger to the electrode surface than C_2 acid (demonstrated by the Temkin isotherms),

more C_2 acid will desorb and end up in the double layer. During the positive anodic pulse, C_2 and C_3 acid adsorb again, however due to the stronger adsorption of C_3 acid, the ratio of adsorbed C_3 to C_2 anions will increase in successive pulses. A higher surface coverage of the Pt electrode surface with C_3 anions will lead to an even more dominant conversion of C_3 acid compared to C_2 acid, consequently increasing the share of C_2H_4 in the product distribution.

Regrettably, the shift in product selectivity was accompanied by a decrease in C_3 acid conversion and an increase in the FE to OER. At a t_c of 500 ms, roughly 22% of the electrons was used for oxygen formation. When the applied Q_c was high, the anodic pulse charge (Q_a) may not be sufficient to fully restore the Kolbe conditions. As a result, oxygen evolution is no longer suppressed by the formation of a (dense) carboxylate layer. Therefore, an exponential increase in O_2 formation was observed starting from a pulse duration of 150 ms. Besides an observed higher FE to OER, the 'loss' of electrons was significant (see Appendix D, Figure D.4). In constant current experiments, roughly 15% of the electrons could not be assigned and hence were attributed to processes like the oxidation of ethanol or the formation of hydrogen peroxide. However, when cathodic pulses were applied, this loss increases to 40%. It is possible that products formed in the vicinity of the electrode surface undergo reduction, leading to the formation of aldehydes. Additionally, electrode restructuring (e.g., platinum oxidation/reduction and dissolution), may also consume part of the electrons. Despite variations in electrolyte composition and pulse conditions, an exponential increase in oxygen evolution was also observed in the work of Hickling et al. when cathodic pulses were applied[140]. They investigated the effect of cathodic pulses in aqueous electrolyte containing acetic acid only and found that when Q_a was roughly 75 times higher than Q_c, oxygen was formed with a FE of ~20%, being close to the OER FE obtained at a charge ratio of 100 (see Table D.3 in Appendix D). A shift in product selectivity and substrate specificity as a result of the galvanic pulses however was not observed since electrolyte containing only acetic acid were electrolysed[18].

Our experimental results demonstrate that substrate specificity and product selectivity in mixed Kolbe electrolysis of C_2 and C_3 acid can be influenced using

galvanic square waveform pulses. It is expected that by applying galvanic square waveform pulses in mixtures with other carboxylic acids substrate specificity will shift to the stronger adsorbing acid. The utilization of galvanic square waveform pulses to influence product selectivity and substrate selectivity in mixed Kolbe electrolysis poses opportunities in the field of electrosynthesis applications using biobased liquids. It could allow for the formation of high-value products. For example, selective production of ethylene from propionic acid can contribute to the production of biobased fuels or plastics. Furthermore, using galvanic square waveform pulses it may be possible to manipulate surface interaction of adsorbed species in solutions containing foreign compounds naturally present in biobased liquids, e.g. alcohols, to selectively decarboxylate acids. However, more research is required to further investigate these potential opportunities.

By combining pulsed electrolysis with methods to suppress the undesired OER, the FE of Pt towards electrochemical decarboxylation and hence the FE to the desired product could be increased even further. By addition of anionic surfactants, such as sodium dodecyl sulphate to the electrolyte, a hydrophobic layer on the Pt anode can be created which repels water molecules and hence improves selectivity to hydrocarbons in Kolbe oxidation[156]. Alternatively, the platinum anode could be modified by a PTFE-layer to increase the hydrophobic nature of the electrode and similarly drive away water molecules from the electrode surface[157]. In Chapter 6 more attention is devoted to these potential solutions that could enhance the feasibility of pulsed electrolysis in mixed Kolbe electrolysis of short-chain carboxylic acids.

Despite the opportunities that pulsed electrolysis in mixed Kolbe electrolysis can offer, it is important that the results obtained in this work are approached with caution. Firstly, because the results do not account for the differences in diffusion constants of the carboxylic acids. Changes in the thickness of the diffusion layer can lead to variations in acid conversion and product selectivity. To provide more insight in this regard, a Rotating Disk Electrode (RDE) could be employed. Secondly, speculations about the composition of the adsorbed layer on the platinum surface have been made, but the adsorbed layer has not been analysed. *In situ* techniques such as surface-enhanced infrared spectroscopy

(SEIRAS) or surface-enhanced Raman spectroscopy (SERS) could reveal the composition of the adsorbed layer in (mixed) Kolbe electrolysis.

5.4. Conclusions

Kolbe electrolysis of C_2, C_3 and C_6 acid and mixtures on platinum anodes was investigated and the reactant specificity and product selectivity were revealed. In mixture with C_2 acid, C_3 acid was favourable oxidized over C_2 acid, whereas in mixture with C_6 acid, C_6 was dominantly converted. The results revealed that differences in surface interaction demonstrated by Temkin adsorption isotherms cause variations in acid conversion, product selectivity and substrate specificity during Kolbe electrolysis of mixtures of C_2, C_3 and C_6 acid. Using galvanic square waveform pulses, substrate specificity and product selectivity in mixed Kolbe electrolysis of C_2 and C_3 acid could be influenced, however this was accompanied by an increase in undesired side reactions, such as oxygen formation. Combining square wave galvanic pulses with methods to reduce OER may enhance efficient conversion of bio-derived acids via Kolbe electrolysis for the production of fuels and chemicals.

Chapter 6

Summary and Outlook

6.1. Summary

This dissertation investigates and discusses the electrochemical decarboxylation of short-chain carboxylic acids on platinum anodes under various reaction conditions. The primary aim was to understand the chemical transformations occurring on Pt electrodes, depending on the electrolyte pH, the nature of the carboxylic acid, and morphology of the Pt electrode. In addition, the feasibility of using low loading Pt electrodes to reduce electrode material costs has been discussed and pulsed electrolysis of mixtures of carboxylic acids were used to improve product yield and alter product selectivity. Overall, the aim was to increase the economic viability of electrochemical decarboxylation.

Chapter 1 discusses the motivation to use electrochemical acid decarboxylation (Kolbe electrolysis) for upgrading of the composition of bio-oil. First, the relevance of bio-oil as sustainable energy source is addressed, followed by an introduction to electrochemical upgrading technologies aimed at enhancing the bio-oil quality. Hereafter, the focus shifts to Kolbe electrolysis and its potential to convert biobased carboxylic acids and produce valuable chemicals. This chapter concludes with an overview of the main challenges and recent technological advances in the field of Kolbe electrolysis for bio-oil upgrading purposes.

Chapter 2 investigates the performance of low loading Pt anodes in the electrochemical decarboxylation of acetic acid. Platinized electrodes were prepared using electrodeposition, sputtering and a dewetting procedure on Ti or FTO substrates obtaining electrodes with different Pt surface coverages. Electrodeposited Pt on Ti anodes were inactive for Kolbe electrolysis due to a low surface coverage of Pt resulting in the oxidation of the exposed Ti substrate. Dewetted Pt on FTO showed high anodic production of ethane but its selectivity dropped over time due to the exposure of FTO leading to enhanced formation of oxygen. Thin films of Pt on Ti demonstrated a high selectivity for Kolbe electrolysis comparable to that of bulk Pt anodes, however continuous Pt dissolution lowered the stability of these anodes. To increase the lifetime of low loading Pt anodes and hence enhance the practical feasibility in Kolbe

electrolysis, anodes with thin films of Pt fully covering the substrate should be employed, while avoiding Pt dissolution.

In **Chapter 3**, the surface structure and composition of bulk Pt anodes during Kolbe electrolysis of acetic acid was investigated. Cyclic Voltammetry measurements, electrochemical Quartz Crystal Microbalance data and X-ray Absorption Spectroscopy spectra showed that continuous oxidation of platinum was inhibited by the presence of a barrier layer of (adsorbed) acetate on the electrode surface. Furthermore, Inductively Coupled Plasma Mass Spectrometry (ICP-MS) data revealed that Pt dissolution was enhanced in the presence of (adsorbed) acetate. Follow up studies to further explore the dissolution rate of Pt under Kolbe conditions are required to assess the economic viability of electro organic syntheses via Kolbe electrolysis.

Chapter 4 studies the influence of the electrolyte pH during Kolbe electrolysis of acetic acid on bulk Pt anodes. Time dependent product analysis revealed that the Kolbe product (ethane) was selectively produced using electrolytes with a pH similar or larger than the pKa of acetic acid. However, in alkaline electrolyte environment (pH 9 and pH 12) selectivity shifted over time to the Hofer-Moest product methanol. It is highlighted that formation of the co-product carbon dioxide and the subsequent formation of carbonate and bicarbonate hinder dimerization and hence cause this selectivity shift. Therefore, accumulation of CO_2 must be prevented by applying continuous reactors, if reaction selectivity to the Kolbe product is desired.

In **Chapter 5** Kolbe electrolysis of (mixtures of) acetic acid, propionic acid and hexanoic acid was investigated using platinum anodes. In mixture with acetic acid, propionic acid was favorably oxidized over acetic acid, whereas in mixture with hexanoic acid, hexanoic acid was dominantly converted. Temkin adsorption isotherms revealed a higher adsorption strength for hexanoic acid compared to propionic and acetic acid which explains the variations in acid conversion, product selectivity and substrate specificity. Considering the strong difference in adsorption strength we rationalized that product selectivity can be manipulated by transient operation. Thus, it was shown by employing galvanic square

waveform pulses that substrate specificity and product selectivity in mixed Kolbe electrolysis of acetic acid and propionic acid could be further directed towards propionic acid conversion. Nevertheless, combining square wave galvanic pulses with methods to reduce oxygen formation is required to achieve efficient conversion of bio-derived acids via Kolbe electrolysis for the production of fuels and chemicals.

6.2 Outlook

Electrochemical decarboxylation of carboxylic acids (Kolbe electrolysis) for bio-oil upgrading purposes can be considered as an attractive approach to replace traditional catalytic upgrading technologies. Operation at moderate reaction conditions while utilizing (surplus) renewable electricity significantly reduces the carbon footprint of bio-oil upgrading processes, simultaneously enabling the production of valuable chemicals and fuels. Despite the expanding research on Kolbe electrolysis using biobased carboxylic acids, a considerable gap still exists between lab-scale scientific developments and their application on an industrial scale. Therefore, in this chapter the remaining knowledge gaps in literature are discussed, focusing on fundamental understanding and industrial challenges. Furthermore, potential opportunities to enhance the role of Kolbe electrolysis in future electrified biorefineries are explored.

To increase fundamental understanding, the key enabler is to better comprehend the role of the electrode. In Chapter 3 the surface of a platinum anode was explored during Kolbe electrolysis of acetic acid using cyclic voltammetry, eQCM and XAS. Even though these techniques strongly support the presence of an adsorbed carboxylate layer on the Pt surface during Kolbe electrolysis, the composition of this layer has not been analyzed. Knowledge on its composition can provide more insight in the adsorption kinetics of Kolbe electrolysis, potentially enhancing product yield and selectivity. To characterize the adsorption layer, surface-sensitive analysis techniques such as *in situ* Surface Enhanced Infrared Spectroscopy (SEIRAS) or *in situ* Surface Enhanced Raman Spectroscopy (SERS) can be employed. Several attempts have been made by the author to use these techniques, however low surface sensitivity caused by

the poor plasmonic properties of platinum resulted in weak signals. In an attempt to enhance the surface sensitivity, the use of shell isolated nanoparticles (SHINs) could be considered[158–160].

Besides studying the composition of the adsorbed layer, it is essential to acquire a better understanding of the dissolution behaviour of Pt. In Chapter 3, Inductively Coupled Plasma Mass Spectrometry was used to demonstrate that anodic Pt dissolution was significant under Kolbe conditions. As this hinders the utilization of Pt anodes in Kolbe electrolysis, it is crucial to know under which applied reaction conditions Pt dissolution is minimal. Besides, possible methods to further reduce Pt dissolution can be explored including application of a protective coating, such as SiO_2[161], or producing platinum alloys to enhance its corrosion resistance. However, the transition of Kolbe electrolysis from the laboratory to an industrial scale will demand significant capital expenditure (capex) since platinum is unabundant and therefore expensive. For example, when considering a simplified batch reactor with a volume-to-electrode ratio of 5 cm^2/L, a 500 cm^2 electrode would be necessary for a 100 L reactor. So, with a minimum price of Pt at 24 €/cm^2 (i.e. 112 €/g), the electrode would cost at least 12,000 €[72]. Furthermore, as the electrode's lifespan is constrained by the continuous dissolution of Pt, it is essential to find alternative electrode materials for Kolbe electrolysis.

Metals like nickel and gold have been considered; however these were found to be inactive for (non)-Kolbe electrolysis, likely due to the absence of the formation of a carboxylate barrier layer[82]. Self-made electrode materials such as thin films of RuO_2/Ti and IrO_2 have demonstrated activity towards Kolbe products[49,70,71]; however, these electrodes are not commercially available, hardly scalable, and lack a current efficiency and selectivity comparable to pure Pt. In future research, the focus could be on finding materials which strongly adsorb RCOO* and weakly bind H_2O* in aqueous conditions, as this may result in lower overpotentials and increased selectivity towards Kolbe products[60].

Furthermore, it is important to increase understanding on the role of the carboxylic acid and screen a wider scope of carboxylic acids. In this thesis, three

different carboxylic acids have been discussed. Chapter 5 revealed that these acids interact differently with the electrode surface and consequently follow distinct reaction pathways under the applied reaction conditions. For applications in bio-oil upgrading, it is particularly important to study acids that are abundantly present in the bio-oil. Besides, as the industrial feedstock will mainly consist of mixtures of acids, blends of acids need to be electrolyzed to investigate substrate specificity. Furthermore, it is important to study the anodic decarboxylation in the presence of other oxygenated components (naturally available in in bio-oil) as they can affect the Kolbe electrolysis process. This will reveal whether prior separation processes are required to maintain a high efficiency towards carboxylic acid decarboxylation.

Finally, to further broaden the spectrum of sustainably produced chemicals, electrochemical conversion of carboxylic acid could be coupled with other processes. During Kolbe electrolysis of medium to long chain carboxylic acids, gas streams are produced that mainly consist of CO_2 as co-product formed at the anode and hydrogen produced at the cathode. These gas mixtures can be employed in bioprocesses to produce valuable products. Previous work[46] has shown that these processes are promising, as they are relatively robust and tolerant towards gas feed impurities such as water vapor and O_2 or varying CO_2/H_2 gas ratio's[162,163]. Alternatively, the anodic decarboxylation of carboxylic acids could be coupled with another electrochemical cathodic process, such as ECH of aldehydes/ketones to double the maximum theoretical efficiency in bio-oil upgrading processes. However, it is vital to resolve mismatch issues between the cathodic and anodic reactions regarding catalyst and electrolyte compatibility to enhance the application potential of these paired electrolysis systems.

Bibliography

[1] B. Sorensen, *Energy Policy* **1991**, *19*, 8–12.

[2] Energy Institute Statistical Review of World Energy, “Energy consumption by source, World,” can be found under https://ourworldindata.org/grapher/energy-consumption-by-source-and-country, **2023**.

[3] N. Abas, A. Kalair, N. Khan, *Futures* **2015**, *69*, 31–49.

[4] C. B. Field, M. R. Raupach, *The Global Carbon Cycle: Integrating Humans, Climate and the Natural World*, Island Press, **2004**.

[5] Global Monitoring Laboratory, “Trends in Atmosperic Carbon Dioxide,” can be found under https://gml.noaa.gov/ccgg/trends/, **2023**.

[6] NASA, “World of Change: Global Temperatures,” can be found under https://earthobservatory.nasa.gov/world-of-change/global-temperatures#:~:text=According to an ongoing temperature,1.9° Fahrenheit) since 1880., **2022**.

[7] M. Vermeer, S. Rahmstorf, *PNAS* **2009**, *106*, DOI 10.1073/pnas.0907765106.

[8] R. Nicholls, R.J., Hanson, S., Herweijer, C., Patmore, N., Hallegatte, S., Corfee-Morlot, J., Chateau, J., Muir-Wood, *“Ranking the World’s Cities Most Exposed to Coastal Flooding Today and in the Future” Executive Summary*, **2007**.

[9] P. Ritchie, H., Roser, M., Rosado, “Renewable Energy,” can be found under https://ourworldindata.org/renewable-energy, **2020**.

[10] M. Wei, C. A. Mcmillan, S. De la Rue du Can, *Curr. Sustain. Energy Reports* **2019**, *6*, 140–148.

[11] P. G. Pereirinha, M. González, I. Carrilero, D. Anseán, J. Alonso, J. C. Viera, *Transp. Res. Procedia* **2018**, *33*, 235–242.

[12] International Energy Agency, “Bioenergy,” can be found under https://www.iea.org/energy-system/renewables/bioenergy, **2023**.

[13] J. M. Bergthorson, M. J. Thomson, *Renew. Sustain. Energy Rev.* **2015**, *42*, 1393–1417.

[14] D. Debnath, M. Khanna, D. Rajagopal, D. Zilberman, *Appl. Econ. Perspect. Policy* **2019**, *41*, 563–582.

[15] G. W. Huber, S. Iborra, A. Corma, *Chem. Rev.* **2006**, *2*, 4044–4098.

[16] A. Dahman, Y; Dignan, C; Fiayaz, A; Chaudhry, *Biomass, Biopolymer-Based Materials, and Bioenergy - Chapter 13 - An Introduction to*

Biofuels, Foods, Livestock, and the Environment, **2019**.

[17] C. Kee, H. Chyuan, W. Chen, T. Chuan, E. Poh, *Energy Convers. Manag.* **2018**, *173*, 81–94.

[18] R. A. Lee, J. Lavoie, *Anim. Front.* **2013**, *3*, 6–11.

[19] J. Chen, J. Li, W. Dong, X. Zhang, R. D. Tyagi, P. Drogui, R. Y. Surampalli, *Renew. Sustain. Energy Rev.* **2018**, *90*, 336–346.

[20] T. Mathimani, N. Mallick, *Renew. Sustain. Energy Rev.* **2020**, *91*, 1103–1120.

[21] J. C. Serrano-ruiz, J. A. Dumesic, *Energy Environ. Sci.* **2011**, *4*, 83–99.

[22] A. R. K. Gollakota, M. Reddy, M. D. Subramanyam, N. Kishore, *Renew. Sustain. Energy Rev.* **2016**, *58*, 1543–1568.

[23] A. V. Bridgwater, *Fast Pyrolysis of Biomass: A Handbook*, CPL Press, **2008**.

[24] P. Basu, in *Gasification, Pyrolysis and Torrefaction*, Elsevier Inc., **2018**, pp. 415–443.

[25] C. H. Lam, W. Deng, L. Lang, X. Jin, X. Hu, Y. Wang, *Energy and Fuels* **2020**, *34*, 7915–7928.

[26] S. Xiu, A. Shahbazi, *Renew. Sustain. Energy Rev.* **2012**, *16*, 4406–4414.

[27] P. M. Mortensen, J. D. Grunwaldt, P. A. Jensen, K. G. Knudsen, A. D. Jensen, *Appl. Catal. A Gen.* **2011**, *407*, 1–19.

[28] A. Ochoa, J. Bilbao, A. G. Gayubo, P. Castaño, *Renew. Sustain. Energy Rev.* **2020**, *119*, 1–29.

[29] S. Hansen, A. Mirkouei, L. A. Diaz, *Renew. Sustain. Energy Rev.* **2020**, *118*, 109548.

[30] H. S. Bard, A., Faulkner, L.R., White, *Electrochemical Methods: Fundamentals and Applications, 3rd Edition*, **2022**.

[31] J. R. Page, Z. Manfredi, S. Bliznakov, J. A. Valla, *Materials (Basel).* **2023**, *16*, DOI 10.3390/ma16010394.

[32] G. Chen, L. Liang, N. Li, X. Lu, B. Yan, Z. Cheng, *ChemSusChem* **2021**, 1037–1052.

[33] Y. Kwon, M. T. M. M. Koper, *ChemSusChem* **2013**, *6*, 455–462.

[34] U. Sanyal, J. Lopez-Ruiz, A. B. Padmaperuma, J. Holladay, O. Y. Gutiérrez, *Org. Process Res. Dev.* **2018**, *22*, 1590–1598.

[35] Z. Li, M. Garedew, C. H. Lam, J. E. Jackson, D. J. Miller, C. M. Saffron,

Green Chem. **2012**, *14*, 2540–2549.

[36] H. Luo, J. Barrio, N. Sunny, A. Li, L. Steier, N. Shah, I. E. L. Stephens, M. M. Titirici, *Adv. Energy Mater.* **2021**, *11*, DOI 10.1002/aenm.202101180.

[37] Y. Yang, T. Mu, *Green Chem. Chem.* **2021**, *23*, 4228–4254.

[38] Y. Wu, Z. Guo, C. Sun, X. Ren, Q. Li, *Fuel Process. Technol.* **2022**, *237*, 1–10.

[39] C. J. Bondue, M. T. M. Koper, *J. Catal.* **2019**, *369*, 302–311.

[40] J. T. Brosnahan, Z. Zhang, Z. Yin, S. Zhang, *Nanoscale R. Soc. Chem.* **2021**, *13*, 2312–2316.

[41] X. Deng, W., Syed-Hassan, S.S.A., Lam, C.H., Hu, X., Wang, *Energy Convers. Manag.* **2022**, *253*, 1–8.

[42] W. Deng, X. Wang, C. Ho, Z. Xiong, H. Han, J. Xu, L. Jiang, S. Su, S. Hu, Y. Wang, J. Xiang, *Fuel Process. Technol.* **2022**, *225*, 107036.

[43] E. M. Andrews, J. D. Egbert, U. Sanyal, J. D. Holladay, R. S. Weber, *Energy&Fuels* **2020**, *34*, 1162–1165.

[44] B. J. Taitt, D. Nam, K. Choi, *ACS Catal.* **2019**, *9*, 660–670.

[45] S. R. Kubota, K. Choi, *ACS Sustain. Chem. Eng.* **2018**, *6*, 9596–9600.

[46] N. Teetz, D. Holtmann, F. Harnisch, M. Stöckl, *Angew. Chemie* **2022**, *134*, 1–6.

[47] F. J. Holzhäuser, J. B. Mensah, R. Palkovits, *Green Chem.* **2020**, DOI 10.1039/c9gc03264a.

[48] S. Palkovits, R. Palkovits, *Chemie-Ingenieur-Technik* **2019**, *91*, 699–706.

[49] G. Creusen, F. J. Holzhäuser, J. Artz, S. Palkovits, R. Palkovits, *ACS Sustain. Chem. Eng.* **2018**, *6*, 17108–17113.

[50] C. Urban, J. Xu, H. Sträuber, T. R. Dos Santos Dantas, J. Mühlenberg, C. Härtig, L. T. Angenent, F. Harnisch, *Energy Environ. Sci.* **2017**, *10*, 2231–2244.

[51] P. Nilges, T. R. Dos Santos, F. Harnisch, U. Schröder, *Energy Environ. Sci.* **2012**, *5*, 5231–5235.

[52] F. J. Holzhäuser, G. Creusen, G. Moos, M. Dahmen, A. König, J. Artz, S. Palkovits, R. Palkovits, *Green Chem.* **2019**, *21*, 2334–2344.

[53] K. Neubert, M. Hell, M. Chávez Morejón, F. Harnisch, *ChemSusChem* **2022**, *15*, DOI 10.1002/cssc.202201426.

[54] M. C. Leech, K. Lam, *Acc. Chem. Res.* **2020**, *53*, 121–134.

[55] M. Faraday, *Ann. Phys.* **1834**, *109*, 481–520.

[56] H. Kolbe, *Justus Liebigs Ann. Chem.* **1849**, *69*, 257–294.

[57] A. Wurtz, *Ann. der Chemie und Pharm.* **1855**, *96*, 364–375.

[58] A. C. Brown, J. Walker, *Justus Liebig's Ann. der Chemie* **1891**, *261*, 107–128.

[59] M. Hofer, H. and Moest, *Ann.* **1902**, *323*.

[60] S. Liu, N. Govindarajan, H. Prats, K. Chan, *Chem Catal.* **2022**, *2*, 1100–1113.

[61] M. O. Nordkamp, B. Mei, R. Venderbosch, G. Mul, *ChemCatChem* **2022**, *14*, DOI 10.1002/cctc.202200438.

[62] H.-J. Schäfer, *Electrochem. IV* **2005**, 91–151.

[63] S. N. . O. J. W. Shukla, *Trans. Faraday Soc. 28* **1932**, 457–462.

[64] O. J. Shukla, S.N., Walker, *Trans. Faraday Soc.* **1931**, 35–40.

[65] Fioshin, M.Y., Vasil'ev, Y.B., *Russ Chem Bull 12* **1963**, 393–400.

[66] M. Fleischmann, J. R. Mansfield, Lord Wynne-Jones, *J. Electroanal. Chem.* **1965**, *10*, 522–537.

[67] Y. Zhang, G. Liu, J. Wu, *J. Electroanal. Chem.* **2018**, *822*, 73–80.

[68] J. E. Sanderson, P. F. Levy, L. K. Cheng, G. W. Barnard, *J. Electrochem. Soc.* **1983**, *130*, 1844–1848.

[69] C. Stang, F. Harnisch, *ChemSusChem* **2016**, *9*, 50–60.

[70] Y. Qiu, J. A. Lopez-Ruiz, U. Sanyal, E. Andrews, O. Y. Gutiérrez, J. D. Holladay, *Appl. Catal. B Environ.* **2020**, *277*, 1–19.

[71] Y. Qiu, J. A. Lopez-Ruiz, G. Zhu, M. H. Engelhard, O. Y. Gutiérrez, J. D. Holladay, *Appl. Catal. B Environ.* **2022**, *305*, 0–1.

[72] K. Neubert, M. Schmidt, F. Harnisch, *ChemSusChem* **2021**, *14*, 3097–3109.

[73] T. R. Dos Santos, F. Harnisch, P. Nilges, U. Schröder, *ChemSusChem* **2015**, *8*, 886–893.

[74] N. Kurig, J. Meyers, F. J. Holzhäuser, S. Palkovits, R. Palkovits, *ACS Sustain. Chem. Eng.* **2020**, DOI 10.1021/acssuschemeng.0c06982.

[75] T. Ashraf, A. Paradelo Rodriguez, B. T. Mei, G. Mul, *Faraday Discuss.* **2023**, 1–8.

[76] F. J. Holzhäuser, J. B. Mensah, R. Palkovits, *Green Chem.* **2020**, *22*, 286–301.

[77] D. Klüh, W. Waldmüller, M. Gaderer, *Clean Technol.* **2021**, *3*, 1–18.

[78] G. Yuan, C. Wu, G. Zeng, X. Niu, G. Shen, L. Wang, X. Zhang, R. Luque, Q. Wang, *ChemCatChem* **2020**, *12*, 642–648.

[79] G. Yuan, L. Wang, X. Zhang, R. Luque, Q. Wang, *ACS Sustain. Chem. Eng.* **2019**, *7*, 18061–18066.

[80] S. Wang, D. Ren, Y. Du, M. Zhang, N. Zhang, Y. Sun, Z. Huo, *Carbon Resour. Convers.* **2023**, *6*, 287–297.

[81] F. J. Vidal-Iglesias, R. M. Arán-Ais, J. Solla-Gullón, E. Herrero, J. M. Feliu, *ACS Catal.* **2012**, *2*, 901–910.

[82] W. F. K. Dickinson, T., Wynne-Jones, W. F. K. Dickinson, T., Wynnes-Jones, W. F. K. Dickinson, T., Wynne-Jones, *Trans. Faraday Soc.* **1961**, *58*, 382–387.

[83] J. D. Benck, B. A. Pinaud, Y. Gorlin, T. F. Jaramillo, *PLoS One* **2014**, *9*, DOI 10.1371/journal.pone.0107942.

[84] M. Altomare, N. T. Nguyen, P. Schmuki, *Chem. Sci.* **2016**, *7*, 6865–6886.

[85] I. T. McCrum, M. J. Janik, *ChemElectroChem* **2016**, *3*, 1609–1617.

[86] J. Ranninger, P. Nikolaienko, K. J. J. Mayrhofer, B. B. Berkes, *ChemSusChem* **2022**, *15*, 1–7.

[87] B. A. Frontana-Uribe, R. D. Little, J. G. Ibanez, A. Palma, R. Vasquez-Medrano, *Green Chem.* **2010**, *12*, 2099–2119.

[88] S. Devi, N. Jyoti, N. Kiran, D. Wadhwa, J. Sindhu, *Org. Biomol. Chem.* **2022**, *20*, 5163–5229.

[89] D. Pletcher, *Electrochem. commun.* **2018**, *88*, 1–4.

[90] O. Q. Carvalho, P. Adiga, S. K. Murthy, J. L. Fulton, O. Y. Gutiérrez, K. A. Stoerzinger, *iScience* **2020**, *23*, 1–12.

[91] S. Koh, J. Leisch, M. F. Toney, P. Strasser, *J. Phys. Chem. C* **2007**, *111*, 3744–3752.

[92] R. V. Mom, L. J. Falling, O. Kasian, G. Algara-Siller, D. Teschner, R. H. Crabtree, A. Knop-Gericke, K. J. J. Mayrhofer, J. J. Velasco-Vélez, T. E. Jones, *ACS Catal.* **2022**, *12*, 5174–5184.

[93] C. L. Bentley, M. Kang, P. R. Unwin, *J. Am. Chem. Soc.* **2019**, *141*, 2179–2193.

[94] S. Mezzavilla, C. Baldizzone, A. C. Swertz, N. Hodnik, E. Pizzutilo, G.

Polymeros, G. P. Keeley, J. Knossalla, M. Heggen, K. J. J. Mayrhofer, F. Schüth, *ACS Catal.* **2016**, *6*, 8058–8068.

[95] N. Danilovic, R. Subbaraman, K. C. Chang, S. H. Chang, Y. J. Kang, J. Snyder, A. P. Paulikas, D. Strmcnik, Y. T. Kim, D. Myers, V. R. Stamenkovic, N. M. Markovic, *J. Phys. Chem. Lett.* **2014**, *5*, 2474–2478.

[96] R. Li, B. Hu, T. Yu, H. Chen, Y. Wang, S. Song, *Adv. Sci.* **2020**, *7*, DOI 10.1002/advs.201902830.

[97] M. Klein, S. Waldvogel, *Angew. Chemie - Int. Ed.* **2022**, *61*, 1–17.

[98] S. Park, D. Thasia Wijaya, J. Na, C. W. Lee, *Catalysts* **2021**, *11*, 253.

[99] J. Yoshida, K. Kataoka, R. Horcajada, A. Nagaki, *Chem. Rev.* **2008**, *108*, 2265–2299.

[100] L. J. Frevel, R. Mom, J. J. Velasco-Vélez, M. Plodinec, A. Knop-Gericke, R. Schlögl, T. E. Jones, *J. Phys. Chem. C* **2019**, *123*, 9146–9152.

[101] A. Minguzzi, O. Lugaresi, E. Achilli, C. Locatelli, A. Vertova, P. Ghigna, S. Rondinini, *Chem. Sci.* **2014**, *5*, 3591–3597.

[102] K. A. Stoerzinger, O. Diaz-Morales, M. Kolb, R. R. Rao, R. Frydendal, L. Qiao, X. R. Wang, N. B. Halck, J. Rossmeisl, H. A. Hansen, T. Vegge, I. E. L. Stephens, M. T. M. Koper, Y. Shao-Horn, *ACS Energy Lett.* **2017**, *2*, 876–881.

[103] Y. Deng, A. D. Handoko, Y. Du, S. Xi, B. S. Yeo, *ACS Catal.* **2016**, *6*, 2473–2481.

[104] R. Frydendal, E. A. Paoli, B. P. Knudsen, B. Wickman, P. Malacrida, I. E. L. Stephens, I. Chorkendorff, *ChemElectroChem* **2014**, *1*, 2075–2081.

[105] S. Cherevko, A. R. Zeradjanin, A. A. Topalov, N. Kulyk, I. Katsounaros, K. J. J. Mayrhofer, *ChemCatChem* **2014**, *6*, 2219–2223.

[106] S. Cherevko, S. Geiger, O. Kasian, N. Kulyk, J. P. Grote, A. Savan, B. R. Shrestha, S. Merzlikin, B. Breitbach, A. Ludwig, K. J. J. Mayrhofer, *Catal. Today* **2016**, *262*, 170–180.

[107] S. Hebié, L. Cornu, T. W. Napporn, J. Rousseau, B. K. Kokoh, *J. Phys. Chem. C* **2013**, *117*, 9872–9880.

[108] C. J. Bondue, F. Calle-Vallejo, M. C. Figueiredo, M. T. M. Koper, *Nat. Catal.* **2019**, *2*, 243–250.

[109] B. E. Conway, A. K. Vijh, *J. Phys. Chem.* **1967**, *71*, 3637–3654.

[110] I. Sekine, H. Ohkawa, *Bullitin Chem. Soc. Japan* **1979**, *52*, 2853–2857.

[111] M. L. Foresti, A. Pozzi, M. Innocenti, G. Pezzatini, F. Loglio, E. Salvietti, A. Giusti, F. D'Anca, R. Felici, F. Borgatti, *Electrochim. Acta* **2006**, *51*, 5532–5539.

[112] Y. Furuya, T. Mashio, A. Ohma, N. Dale, K. Oshihara, G. Jerkiewicz, *J. Chem. Phys.* **2014**, *141*, DOI 10.1063/1.4898707.

[113] V. I. Birss, M. Chang, J. Segal, *J. Electroanal. Chem.* **1993**, *355*, 181–191.

[114] A. E. Russell, *Phys. Chem. Chem. Phys.* **2008**, *10*, 3607–3608.

[115] C. F. Zinola, A. M. Castro Luna, W. E. Triaca, A. J. Arvia, *J. Appl. Electrochem.* **1994**, *24*, 119–125.

[116] L. D. Burke, M. M. Murphy, **1991**, *305*, 301–312.

[117] F. Burke, L.D., O'Sullivan, *J. Appl. Electrochem.* **1991**, *21*, 151–157.

[118] Y. Sugawara, A. P. Yadav, A. Nishikata, T. Tsuru, *Electrochemistry* **2006**, *4*, 359–365.

[119] T. Sakurai, T., Shibata, M., Horiuchi, R., Yagi, I., Kondo, *Chem. Lett.* **2011**, *40*, 402–404.

[120] Y. M. Kolotyrkin, V. V. Losev, A. N. Chemodanov, *Mater. Chem. Phys.* **1988**, *19*, 1–95.

[121] Z. Wang, E. Tada, A. Nishikata, *J. Electrochem. Soc.* **2014**, *161*, F845–F849.

[122] S. Cherevko, A. A. Topalov, A. R. Zeradjanin, G. P. Keeley, K. J. J. Mayrhofer, *Electrocatalysis* **2014**, *5*, 235–240.

[123] D. Friebel, D. J. Miller, C. P. O. Grady, T. Anniyev, J. Bargar, H. Ogasawara, T. Wikfeldt, L. G. M. Pettersson, *Phys. Chem. Chem. Phys.* **2011**, *13*, 262–266.

[124] B. Ferreira Gomes, F. J. Holzhaüser, C. M. Silva Lobo, P. Ferreira Da Silva, E. Danieli, M. Carmo, L. A. Colnago, S. Palkovits, R. Palkovits, B. Blümich, *ACS Sustain. Chem. Eng.* **2019**, *7*, 18288–18296.

[125] A. K. Vijh, B. E. Conway, *Chem. Rev.* **1967**, *67*, 623–664.

[126] L. Eberson, *Acta Chem. Scand* **1964**, *18*.

[127] Y. B. Vassiliev, V. A. Grinberg, *J. Electroanal. Chem.* **1990**, *283*, 359–378.

[128] H. Liao, Z. Qiu, Q. Wan, Z. Wang, Y. Liu, N. Yang, *ACS Appl. Mater. Interfaces* **2014**, *6*, 18055–18062.

[129] Y. Liu, G. Yuan, X. Ren, Q. Wang, *Int. J. Electrochem. Sci.* **2018**, *13*, 3210–3223.

[130] European Commission, “2050 long-term strategy,” can be found under https://climate.ec.europa.eu/eu-action/climate-strategies-targets/2050-long-term-strategy_en, **2023**.

[131] X. Hu, M. Gholizadeh, *J. Energy Chem.* **2019**, *39*, 109–143.

[132] R. H. Venderbosch, *ChemSusChem* **2015**, *8*, 1306–1316.

[133] G. Perkins, N. Batalha, A. Kumar, T. Bhaskar, M. Konarova, *Renew. Sustain. Energy Rev.* **2019**, *115*, 109400.

[134] H. J. Schäfer, *Chem. Phys. Lipids* **1979**, *24*, 321–333.

[135] B. Coleman, J; Lines, R; Utley, J; Weedon, *J.C.S. Perkin II* **1974**, 1064–1069.

[136] S. V. Vassilev, D. Baxter, L. K. Andersen, C. G. Vassileva, *Fuel* **2010**, *89*, 913–933.

[137] S. Arnold, T. Tews, M. Kiefer, M. Henkel, R. Hausmann, *GCB Bioenergy* **2019**, *11*, 1159–1172.

[138] P. F. Levy, J. E. Sanderson, L. K. Cheng, *J. Electrochem. Soc.* **1984**, *131*, 773–777.

[139] E. Klocke, A. Matzeit, M. Gockeln, H. J. Schäfer, *Chem. Ber.* **1993**, *126*, 1623–1630.

[140] A. Hickling, R. Wilkins, *Discuss. Faraday Soc.* **1968**, *45*, 261–268.

[141] Y. Hioki, M. Costantini, J. Griffin, K. C. Harper, M. P. Merini, B. Nissl, Y. Kawamata, P. S. Baran, *Science* **2023**, *380*, 81–87.

[142] J. Zhong, C. Ding, H. Kim, T. McCallum, K. Ye, *Green Synth. Catal.* **2022**, *3*, 4–10.

[143] D. Gunasekera, J. P. Mahajan, Y. Wanzi, S. Rodrigo, W. Liu, T. Tan, L. Luo, *J. Am. Chem. Soc.* **2022**, *144*, 9874–9882.

[144] S. Rodrigo, D. Gunasekera, J. P. Mahajan, L. Luo, *Curr. Opin. Electrochem.* **2021**, *28*, 100712.

[145] S. Rodrigo, C. Um, J. C. Mixdorf, D. Gunasekera, H. M. Nguyen, L. Luo, *Org. Lett.* **2020**, *22*, 6719–6723.

[146] L. Zeng, J. Wang, D. Wang, H. Yi, A. Lei, *Angew. Chemie - Int. Ed.* **2023**, *202309620*, DOI 10.1002/anie.202309620.

[147] Y. Kawamata, K. Hayashi, E. Carlson, S. Shaji, D. Waldmann, B. J. Simmons, J. T. Edwards, C. W. Zapf, M. Saito, P. S. Baran, *J. Am. Chem. Soc.* **2021**, *143*, 16580–16588.

[148] J. Guo, P. Brimley, M. J. Liu, E. R. Corson, C. Muñoz, W. A. Smith, W. A. Tarpeh, *ACS Sustain. Chem. Eng.* **2023**, *11*, 7882–7893.

[149] N. Singh, U. Sanyal, J. L. Fulton, O. Y. Gutiérrez, J. A. Lercher, C. T. Campbell, *ACS Catal.* **2019**, *9*, 6869–6881.

[150] W. C. Khor, S. Andersen, H. Vervaeren, K. Rabaey, *Biotechnol. Biofuels* **2017**, *10*, 1–11.

[151] G. Jerkiewicz, *Electrocatalysis* **2010**, *1*, 179–199.

[152] N. M. Marković, T. J. Schmidt, B. N. Grgur, H. A. Gasteiger, R. J. Behm, P. N. Ross, *J. Phys. Chem. B* **1999**, *103*, 8568–8577.

[153] K. Sasaki, A. Kunai, J. Harada, S. Nakabori, *Electrochim. Acta* **1983**, *28*, 671–674.

[154] N. Ayawei, A. N. Ebelegi, D. Wankasi, *J. Chem.* **2017**, *2017*, DOI 10.1155/2017/3039817.

[155] S. Gilman, *Electrochim. Acta* **2012**, *65*, 141–148.

[156] L. Lang, Y. Li, J. C. H. Lam, Y. Ding, X. Yin, C. Wu, *Sustain. Energy Fuels* **2022**, *6*, 2797–2804.

[157] T. Ono, Y, Kim, S.H., Yasuda, M., Nonaka, *Electrochemistry* **1999**, *67*, 1042–1045.

[158] S. Guan, O. Donovan-sheppard, C. Reece, D. J. Willock, A. J. Wain, G. A. Attard, *ACS Catal.* **2016**, *6*, 1822–1832.

[159] C. S. Wondergem, T. Hartman, B. M. Weckhuysen, *ACS Catal.* **2019**, *9*, 10794–10802.

[160] T. Hartman, C. S. Wondergem, B. M. Weckhuysen, *ChemPhysChem* **2018**, *19*, 2461–2467.

[161] J. E. Robinson, N. Y. Labrador, H. Chen, B. E. Sartor, D. V. Esposito, *ACS Catal.* **2018**, *8*, 11423–11434.

[162] R. Hegner, K. Neubert, C. Kroner, D. Holtmann, F. Harnisch, *ChemSusChem* **2020**, *13*, 5295–5300.

[163] M. Stöckl, N. J. Claassens, S. N. Lindner, E. Klemm, D. Holtmann, *Curr. Opin. Biotechnol.* **2022**, *74*, 154–163.

Appendix A: Supplementary Information to Chapter 2

A.1. Three electrode electrochemical cell

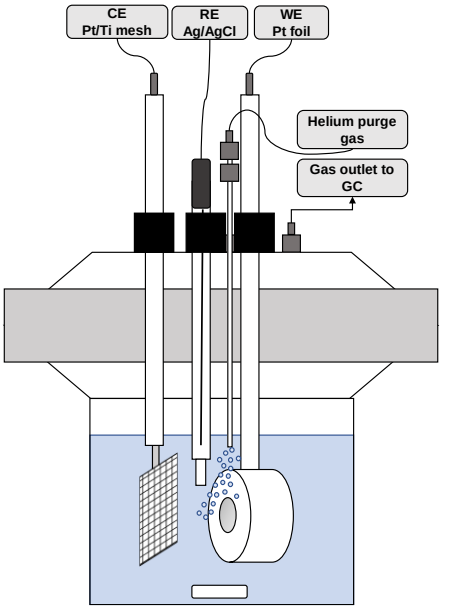

Figure A.1 a) Schematic representation of the custom-built single compartment three electrode glass cell (cell volume of 70 ml) consisting of a working electrode (WE), reference electrode (RE) and counter electrode (CE).

Figure A.1 b) Picture of Teflon electrode clamp purchased from AliExpress.

A.2. External calibration curves for gas analysis

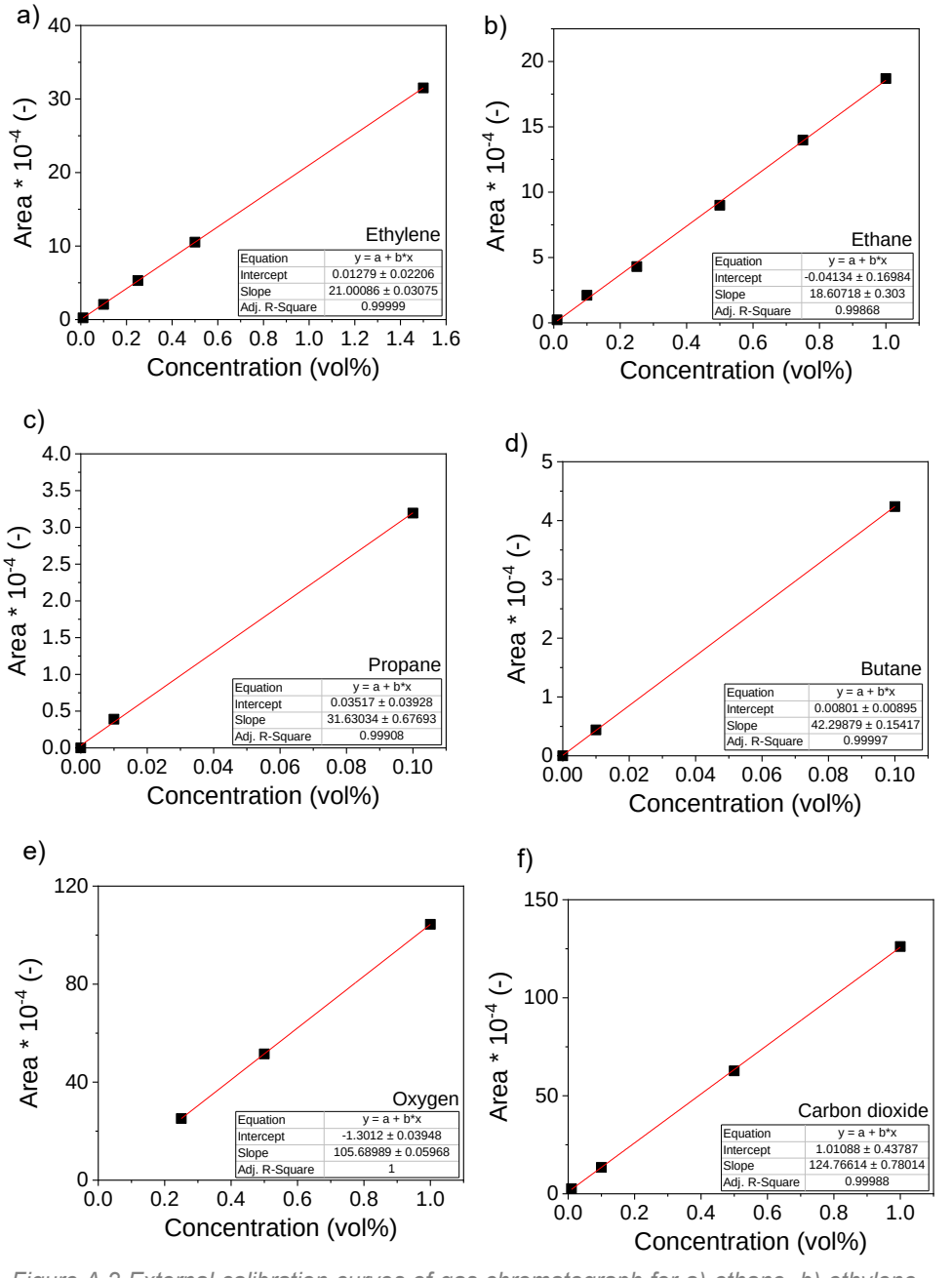

Figure A.2 External calibration curves of gas chromatograph for a) ethane, b) ethylene, c) propane, d) butane, e) oxygen and f) carbon dioxide.

A.3. External calibration curves for liquid analysis

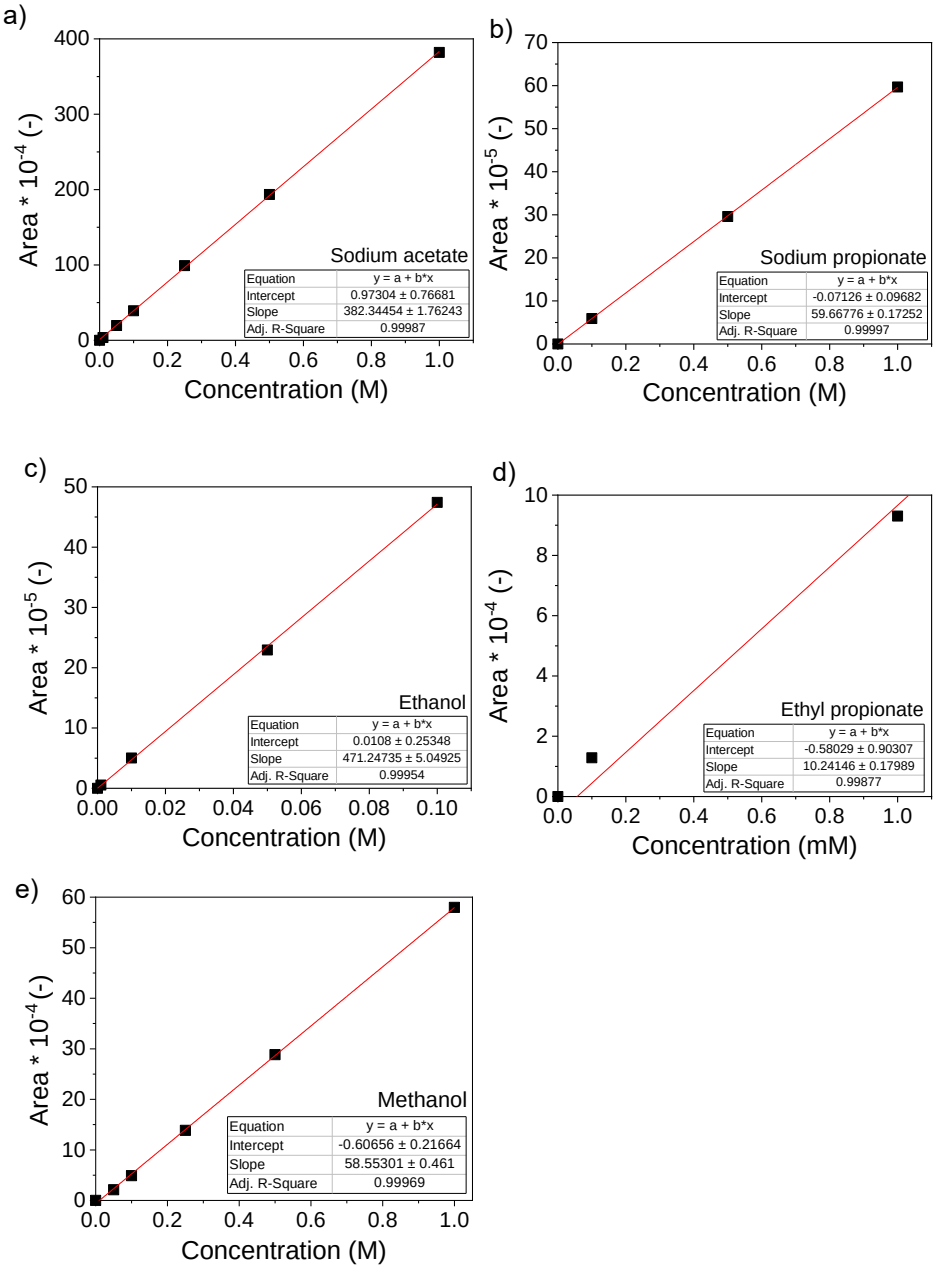

Figure A.3 External calibration curves of HPLC for a) sodium acetate, b) sodium propionate, c) ethanol d) ethyl propionate e) methanol.

A.4. Electrochemical activity of a FTO substrate

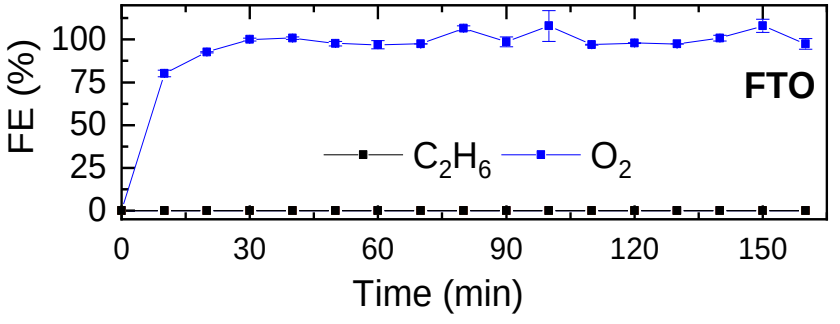

Figure A.4 FE (%) to ethane (black line) and oxygen (blue line) over time (min) during a constant current of 25 mA/cm^2 on bare FTO in 1 M acetic acid/sodium acetate solution (pH 5).

A.5. SEM images and ECSA of dewetted Pt/FTO samples

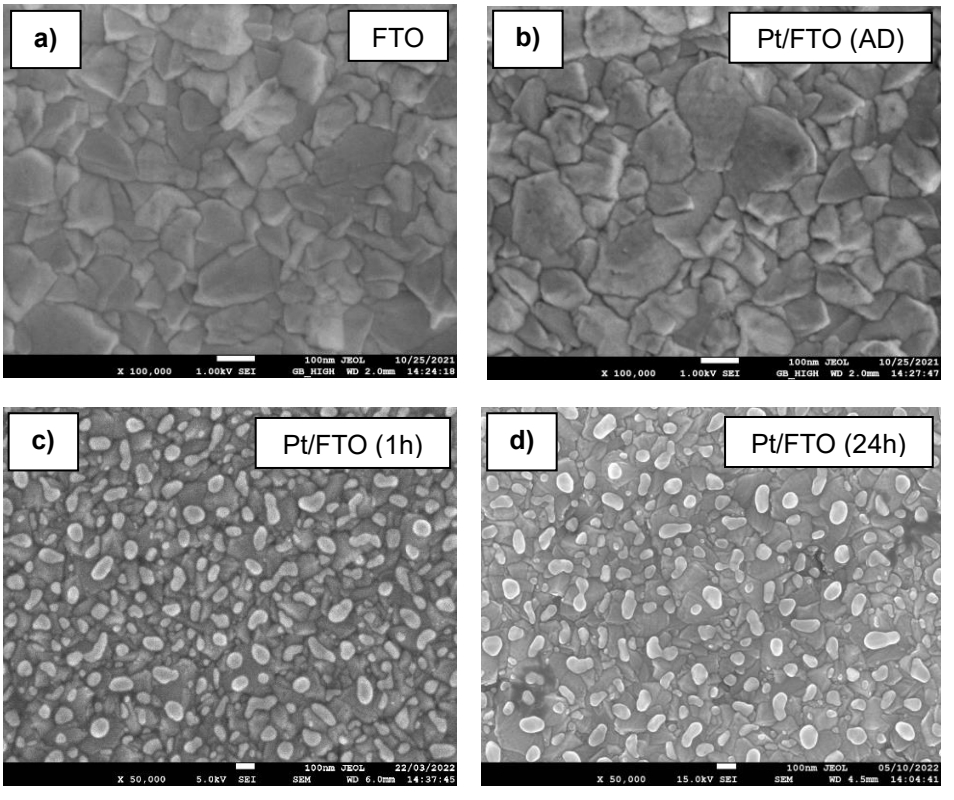

Figure A.5 SEM images of a) FTO b) Pt/FTO (AD) with 10000x magnification c) Pt/FTO (1h) and d) Pt/FTO (24h) with 50000x magnification.

Table A.5 Estimated electrochemical active surface area (cm^2) extracted from the charge density associated with hydrogen adsorption/desorption derived from the corresponding CV scans

Sample	Electrochemical active surface area (cm^2)
Pt-ED/Ti	0.06
Pt/FTO (1h)	3.2
Pt/FTO (24h)	3.0
Pt/FTO (AD)	6.2

A.6. Cyclic voltammograms of Pt/FTO samples before and after electrochemical characterization

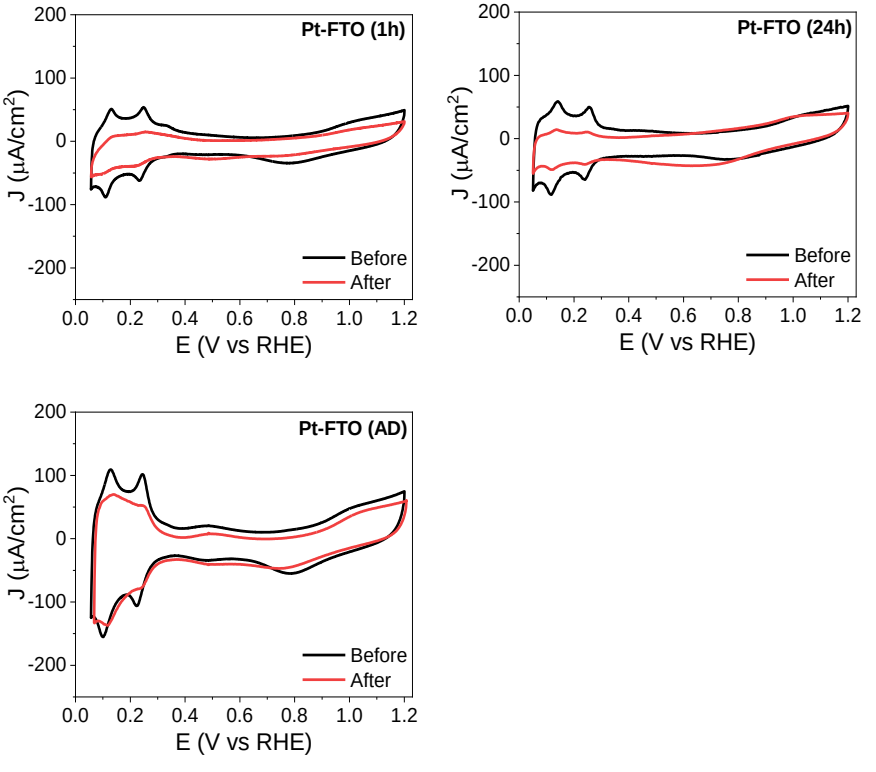

Figure A.6 Cyclic voltammograms of a) Pt-FTO (1h) b) Pt-FTO (24h) c) Pt-FTO (AD) before (black line) and after (red line) a constant current experiment at 25 mA/cm^2 in 1 M acetic acid/sodium acetate solution pH 5, scan rate: 100 mV/s.

A.7. Estimation of Pt dissolution rate for Pt-Ti (TF) samples

Constants

Thickness of 1 monolayer of Pt molecules: 2.76 Å

Area of 1 Pt molecule: $\pi \cdot (1.38)^2 =$ 5.97 Å^2 (π × (radius Pt)^2)

Weight of 1 Pt molecule: $\frac{195.08 \frac{g}{mol}}{6.022x10^{23} \frac{atoms}{mol}} = 3.25\ x\ 10^{-22} grams$

(molar mass / Avogadro's number)

Geometric surface area of the electrode: 0.785 cm^2

Calculations

We assume that the complete layer of Pt on the Ti foil was dissolved within the experimental time before electrode degradation was visible from the exponential rise in potential. For the 5 nm layer, this took 64 min. For 10 nm layer this took, 210 minutes. As no exponential rise in potential was observed for 100 nm Pt-Ti (TF), the Pt dissolution rate could not be estimated.

Number of monolayers on Ti: Layer thickness of Pt on substrate / thickness of 1 monolayer of Pt:

$$\frac{5\ nm}{2.76\ \cdot 10^{-1}\ nm} = 18.11\ monolayers \qquad \frac{10\ nm}{2.76\ \cdot 10^{-1}\ nm} = 36.23\ monolayers$$

Amount of Pt molecules in 1 monolayer: Geometric surface area electrode / area of 1 Pt molecule

$$\frac{0.785\ cm^2}{5.97 \cdot 10^{-16}\ cm^2} = 1.13\ \cdot 10^{15}$$

Amount of Pt molecules on Ti: Amount of Pt molecules in 1 monolayer x number of monolayers on Ti.

For 5 nm: $1.13 \cdot 10^{15}\ x\ 18.11\ monolayers = 2.38 \cdot 10^{16}$

For 10 nm: $1.13 \cdot 10^{15}\ x\ 36.23\ monolayers = 4.76 \cdot 10^{16}$

Total weight of Pt layer: amount of Pt molecules on Ti x weight of a Pt molecule

For 5 nm: $2.38 \cdot 10^{16}\ x\ 3.25\ x\ 10^{-22} grams = 7.71x\ 10^{-6} grams$

For 10 nm: $4.76 \cdot 10^{16}\ x\ 3.25\ x\ 10^{-22} grams = 1.54x\ 10^{-5} grams$

Pt dissolution rate: total weight of the Pt layer per cm^2 / time

For 5 nm: $\frac{7.71x\ 10^{-6} grams \cdot \frac{1}{0.785\ cm^2}}{(64\ min \cdot 60\ s)} = 2.01\ \cdot 10^{-9}\ \frac{grams}{s}$ = 2.56 ng s^{-1} cm^{-2}

For 10 nm: $\frac{1.54x\ 10^{-5} grams \cdot \frac{1}{0.785\ cm^2}}{(210\ min \cdot 60\ s)} = 1.22\ \cdot 10^{-9}\ \frac{grams}{s}$ = 1.56 ng s^{-1} cm^{-2}

A.8. Cyclic voltammograms of thin film Pt-Ti samples before and after electrochemical characterization

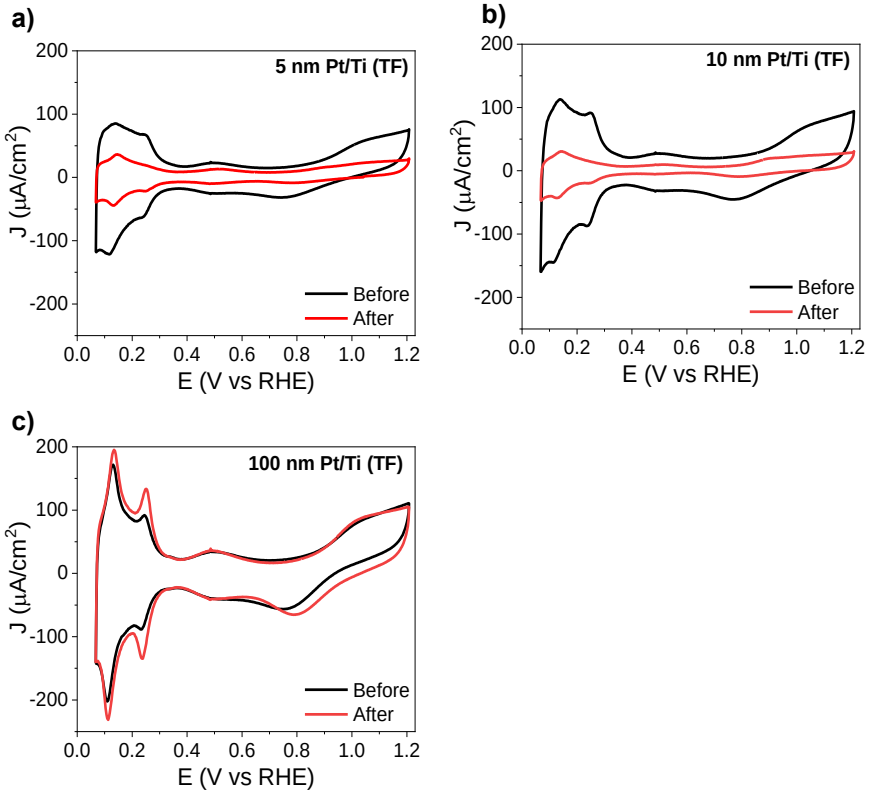

Figure A.8 Cyclic voltammograms of a) 5 nm Pt/Ti (TF) b) 10 nm Pt-Ti (TF) c) 100 nm Pt-Ti (100 nm) before (black line) and after (red line) a constant current experiment at 100 mA/cm² in 1 M acetic acid/sodium acetate solution pH 5, scan rate: 100 mV/s.

Appendix B Supplementary information to Chapter 3

B.1. Reaction mechanism of Kolbe electrolysis

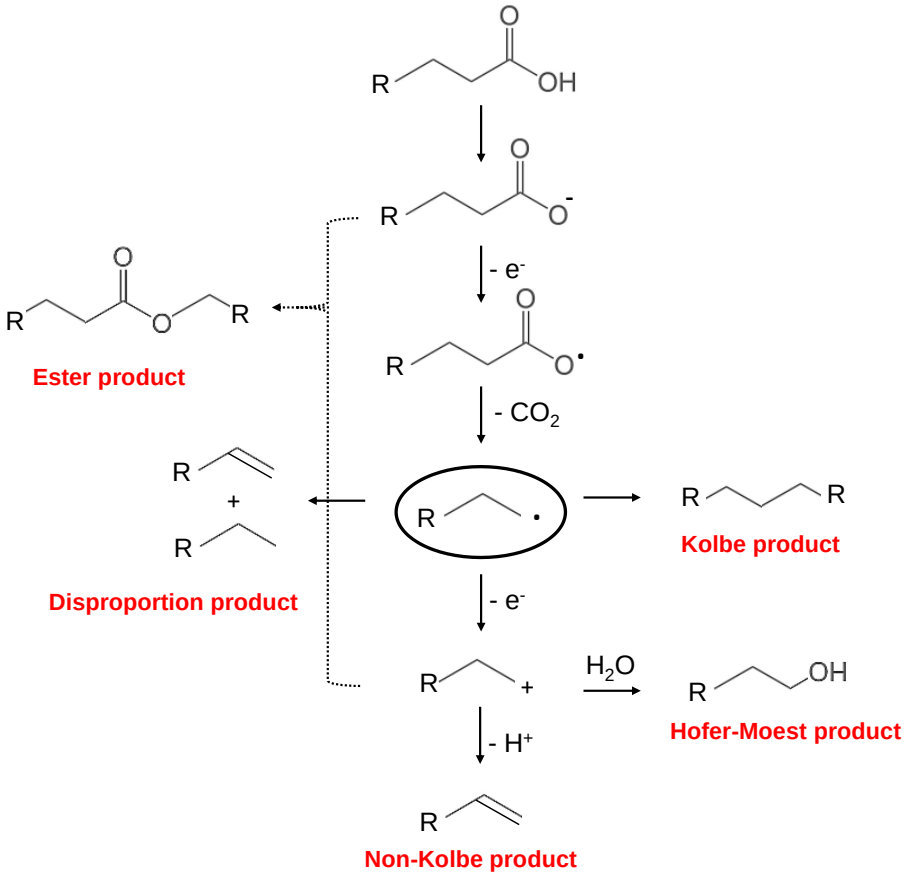

Figure B.1 Schematic representation of the reaction mechanism for the formation of Kolbe, Hofer-Moest, Non- Kolbe, disproportion, and ester products.

B.2. Gamry eQCM cell

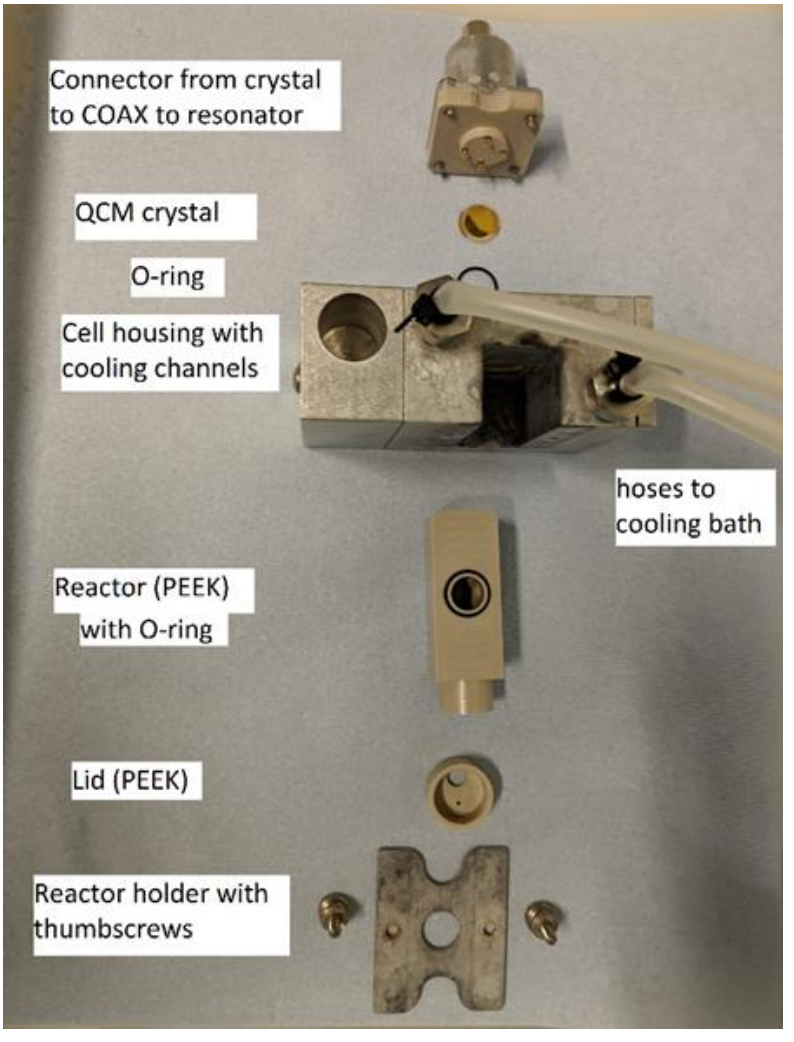

Figure B.2 Picture of the Gamry eQCM cell disassembled with a description of the individual parts.

B.3. X-ray adsorption spectroscopy cell

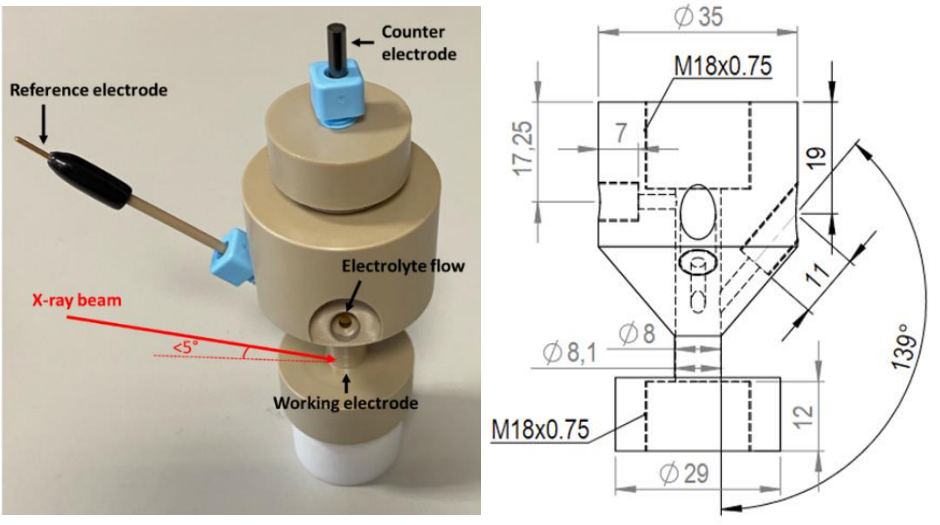

Figure B.3 Picture and schematic drawing of the in situ low incidence angle x-ray absorption spectroscopy cell

B.4. Cyclic voltammograms and potential vs. time curve of a constant current experiment in blank and acetic acid electrolyte in single compartment three electrode glass cell and eQCM reactor

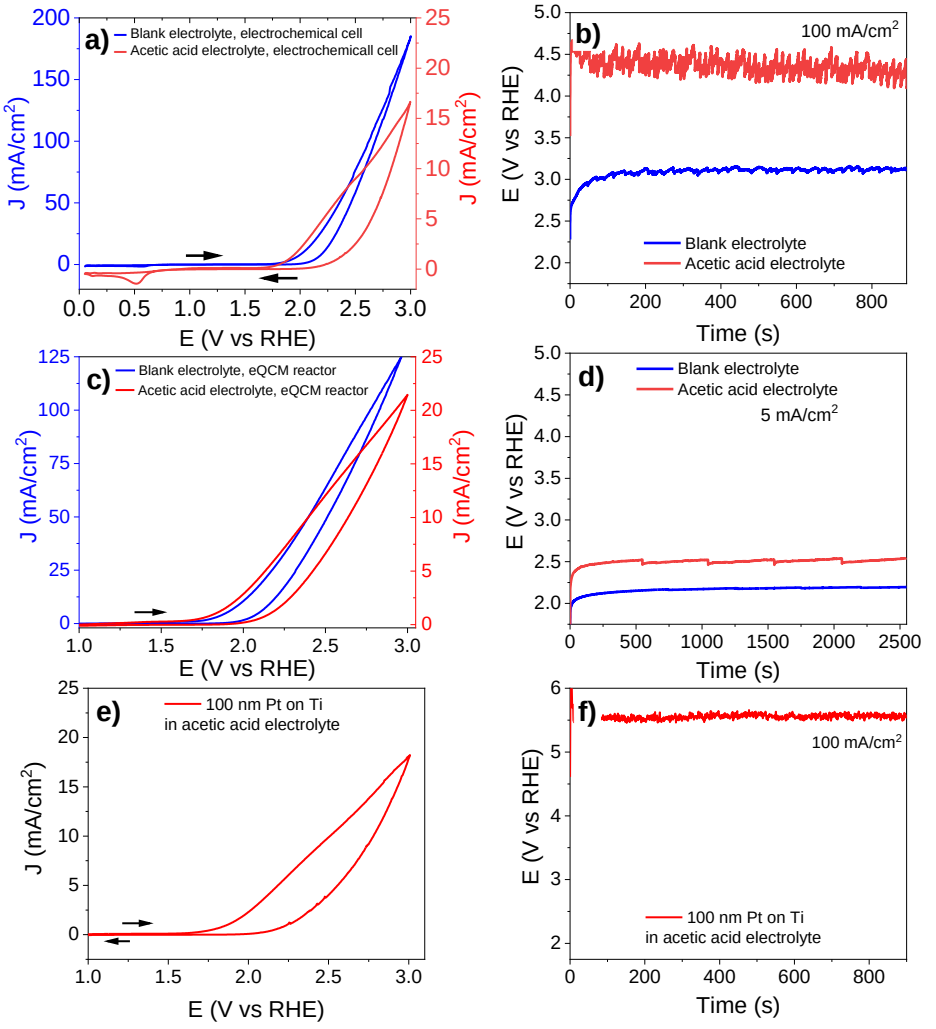

Figure B.4 a) Cyclic voltammogram (scan rate of 100 mV/s) and b) E-t profile (100 mA/cm^2, total charge of 70 C) obtained with a Pt foil in blank electrolyte (blue) and acetic acid electrolyte (red) performed in the single compartment three electrode glass cell; c) Cyclic voltammogram (scan rate of 100 mV/s) and d) E-t profile (5 mA/cm^2, total charge of 10 C) obtained with a Pt-covered eQCM crystal in blank electrolyte (blue) and acetic acid electrolyte (red) in the eQCM cell; e) Cyclic voltammogram of 100 nm Pt thin film sputtedeposited on Ti (scan rate of 100 mV/s) and f) corresponding E-t profile (100 mA/cm^2, total charge of 70 C) obtained in the single compartment three electrode glass cell in acetic acid electrolyte.

B.5. Cyclic voltammograms of Pt in blank and acetic acid electrolyte after polarization at high potential for different durations

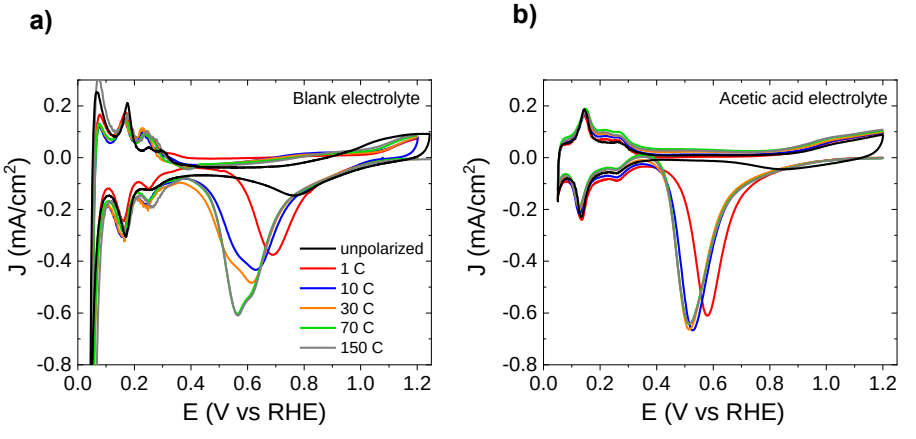

Figure B.5 Cyclic voltammogram in a) blank and b) acetic acid electrolyte after preconditioning the Pt anode at 100 mA/cm^2 after 1, 10, 30, 70 and 150 C of charge had passed. The unpolarized sample was obtained by scanning the potential up to 1.2 V vs RHE. Scan rate: 100 mV/s.

B.6. Relevance of the eQCM data

To study the formation of the platinum oxide layer in more detail, eQCM measurements were performed to reveal the mass changes associated with platinum oxide reduction after polarization in acetic acid electrolyte. The Pt anode was pre-polarized at constant current density of 5 mA/cm^2 until 1, 10 or 70 C of charge were passed. The lower current density was applied to reduce the risk of electrode roughening, dissolution and delamination and thus damaging the thin Pt layer[118][119]. Due to this limitation also oxygen evolution reaction might occur [61]. Nevertheless, as shown by Chan et al.[60], within the potential range of 1.5-2.5 V_{SHE}, Kolbe species dominate on the Pt electrode surface, while surface OER species decrease at potentials above ca. 2 V_{SHE}. Both cyclic voltammetry and potential time-profiles (Figure B.4c and d) suggest that the eQCM measurements are performed within a potential range characterized by a high Pt surface coverage with Kolbe species, moreover comparison of cyclic voltammetry data obtained after polarization of a Pt foil electrode at 5 and 100 mA/cm^2 suggest that the PtO reduction is if at all only influenced to a minor extent (Figure B.7a and b). Thus, meaningful data are obtained by the eQCM, despite the low current density used here.

B.7. Influence of polarization current density on the platinum oxide formation in blank electrolyte and acetic acid electrolyte

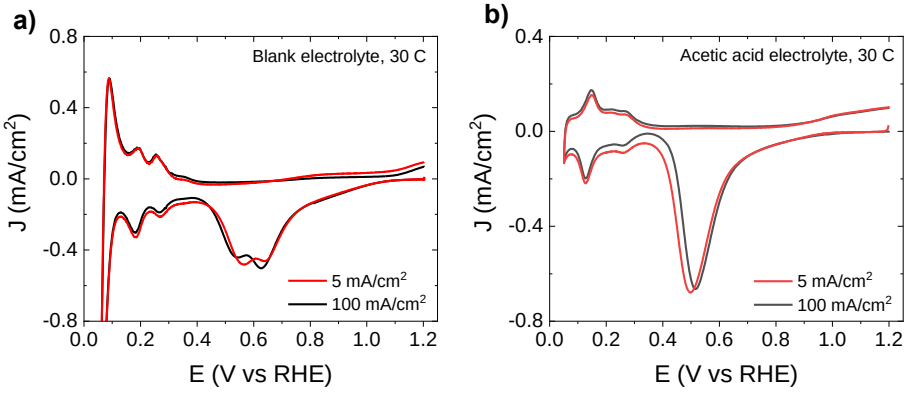

Figure B.7 Cyclic voltammogram in a) blank electrolyte and b) acetic acid electrolyte after preconditioning the Pt anode at 5 and 100 mA/cm² until 30 C of charge had passed.

B.8. CV and associated mass changes during Pt oxide reduction after polarizing the Pt anode at high potential until 1 C

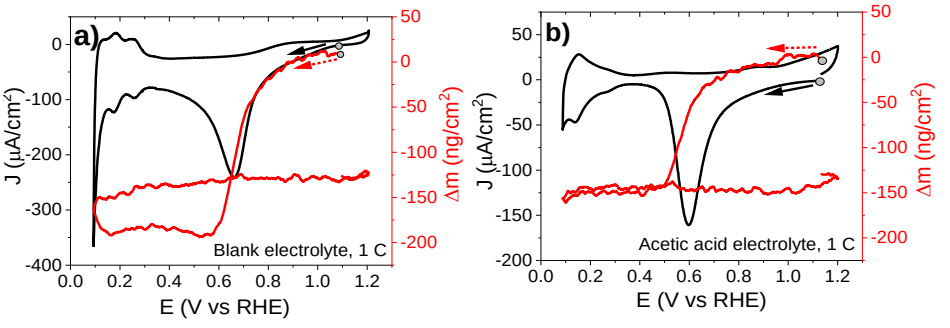

Figure B.8 Cyclic voltammogram and changes in surface mass Δm of preconditioned Pt in a) blank electrolyte and b) acetic acid electrolyte after preconditioning the Pt anode at 5 mA/cm² until 1 C had passed. Scan rate: 10 mV/s.

B.9. Reproducibility of mass changes after polarization in blank and acetic acid electrolyte

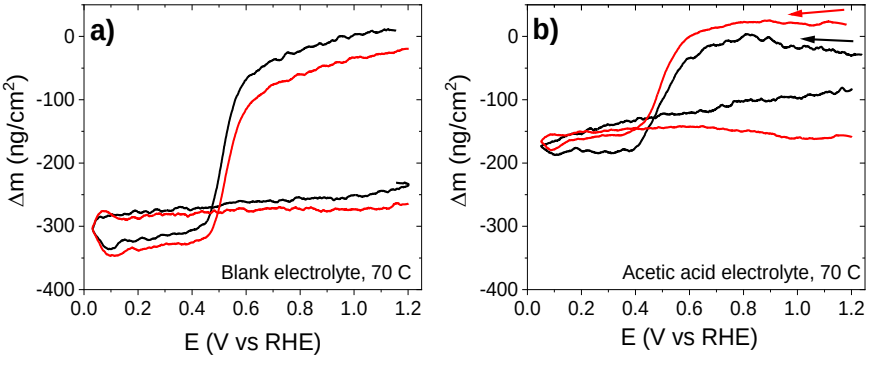

Figure B.9 Two individual experiment that record the changes in surface mass Δm of preconditioned Pt until 70 C has passed in a) blank electrolyte and b) acetic acid electrolyte as a function of the electrode potential. Scan rate: 10 mV/s.

B.10. EXAFS spectra of unpolarized and polarized Pt in blank and acetic acid electrolyte

Figure B.10a and B.10b show the EXAFS and corresponding Fourier Transforms (FTs). No significant differences in phase or amplitude of the EXAFS can be observed. Furthermore, the FTs of the different samples are all superimposable and there is always a higher peak centered at about 2.7 Å corresponding to the distance between the nearest neighbors in the platinum FCC structure.

The EXAFS of all samples were fitted from the same structural model consisting of platinum FCC by taking 4 shells around the photo absorber (the dotted lines represent the Pt-Pt distances of the four shells used in the model). The fit was

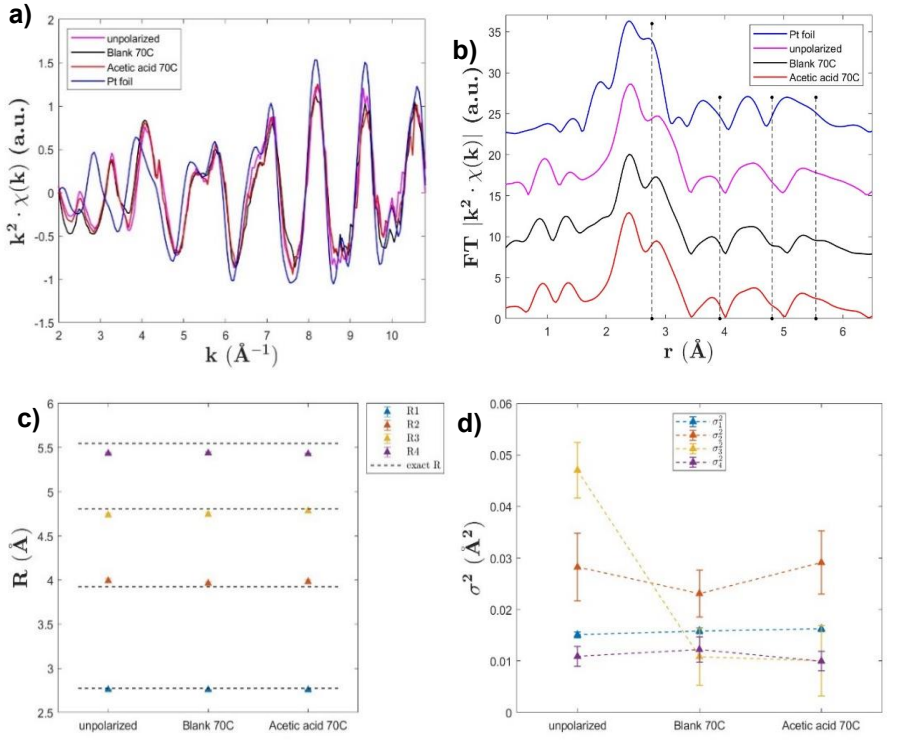

Figure B.10 a) *EXAFS and b) Fourier Transform (FT) of Pt foil (reference) unpolarized Pt and of Pt polarized at 100 mA/cm^2 in blank and acetic acid electrolyte after 70 C. c) Distances between the photo absorber and the first nearest shells as extracted from the fit and d) Debye-Waller factors for the same shells for the unpolarized electrode and the electrode at a 70C polarization in blank and acetic acid electrolyte.*

obtained by varying the distances between the central platinum and the 4 shells (R_1, R_2, R_3, R_4) and the Debye-Waller factors ($\sigma_1, \sigma_2, \sigma_3, \sigma_4$) for the corresponding shells, the results are shown in Table B.10. As shown in Figure B.10c, the distances in the four shells remain almost unchanged in the different samples and, especially for the first two shells, a perfect agreement with the theoretical values of 2.774 Å and 3.923 Å can be seen. Also, with regard to the Debye-Waller factors (Figure B.10d), no significant trend can be seen, and they can be considered constant within the experimental error, confirming that the different samples show the same behavior in terms of local disorder in the different shells.

Table B.10 Distances between the central platinum and the 4 shells (R_1, R_2, R_3, R_4) and the Debye-Waller factors ($\sigma_1, \sigma_2, \sigma_3, \sigma_4$) for the corresponding shells.

	Unpolarized	**Blank 70C**	**Acetic acid 70c**
$\boldsymbol{\sigma_1^2}$	0.015(1)	0.016(1)	0.016(1)
$\boldsymbol{\sigma_2^2}$	0.03(1)	0.023(9)	0.03(1)
$\boldsymbol{\sigma_3^2}$	0.05(1)	0.05(1)	0.04(1)
$\boldsymbol{\sigma_4^2}$	0.011(4)	0.012(5)	0.01(4)
R_1	2.759(5)	2.757(5)	2.756(5)
R_2	3.99(5)	3.96(4)	3.98(5)
R_3	4.74(4)	4.74(5)	4.78(4)
R_4	5.43(2)	5.44(2)	5.43(2)

B.11. Linear combination fitting XANES

Table B.11 Percentages of linear combination fitting of the XANES spectra of unpolarized Pt, Pt polarized in blank electrolyte and Pt polarized in acetic acid electrolyte using the XANES spectra of Pt foil and PtO2 pellets as the reference standards.

	Pt (%)	PtO_2 (%)
Pt unpolarized	97.6%	2.4%
Pt polarized in blank	87.9%	12.1%
Pt polarized in acetic acid	89.4%	10.6%

These numbers support that Pt oxide formation is lower in acetic acid electrolyte compared to the blank electrolyte, however they should not be considered to be accurate. The linear combination fitting was done with a Pt foil and PtO_2 pellets as a standard. The foil is not expected to be representative of Pt nanoparticles. Additionally, the spectrum of highly crystalline PtO_2 standard is highly crystalline, which, again, is (or may be) not representative of a disordered oxide layer. In order to obtain a better fit by linear combination, representative standards are required.

Appendix C: Supplementary information to Chapter 4

C.1. Electrolyte composition and acetic acid/acetate equilibrium

Equilibrium reaction between acetic acid and acetate:

$$CH_3COOH + H_2O \leftrightarrow CH_3COO^- + H_3O^+ \quad \text{(C1.1)}$$

Henderson-Hasselbalch equation, which can calculate the pH of a solution containing a mixture of a weak acid (HA) with its conjugated base (A-) using the acid dissociation constant, Ka, and the concentration.

$$pH = pK_a + \log\frac{[A^-]}{[HA]} \quad \text{(C1.2)}$$

[*] = add NaOH to adjust pH to 12
[**] = pH after 320 min at constant current

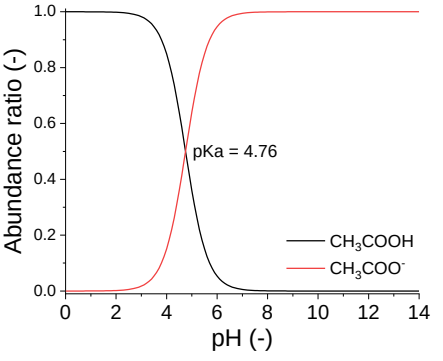

Figure C.1 Abundance ratio of acetic acid and acetate as a function of the pH of the solution.

Test condition	CH_3COOH (M)	$NaCH_3COO$ (M)	$HClO_4/NaClO_4$ (M)	Solution resistance (Ω)	Initial pH (-)	pH after 160 min at constant current (-)
Blank electrolyte pH 2	-	-	1	5	2.4	-
Blank electrolyte pH 4	-	-	1	5	3.7	-
Blank electrolyte pH 5	-	-	1	5	4.7	-
Blank electrolyte pH 9	-	-	1	5	8.7	-
Blank electrolyte pH 12*	-	-	1	5	11.6	-
Acetic acid electrolyte pH 2 @ 25 mA/cm^2	0.988	0.002	-	130	2.4	2.4
Acetic acid electrolyte pH 4 @ 25 mA/cm^2	0.926	0.007	-	75	3.6	3.6
Acetic acid electrolyte pH 5 @ 25 mA/cm^2	0.500	0.500	-	11	4.7	4.7
Acetic acid electrolyte pH 5 @ 1 mA/cm^2	0.500	0.500	-	11	4.7	4.7
Acetic acid electrolyte pH 5 @ 5 mA/cm^2	0.500	0.500	-	11	4.7	4.7
Acetic acid electrolyte pH 5 @ 10 mA/cm^2	0.500	0.500	-	11	4.7	4.7
Acetic acid electrolyte pH 9 @ 25 mA/cm^2	0	1	-	9	8.7	9.3
Acetic acid electrolyte pH 12* @ 25 mA/cm^2	0	1	-	8	12	9.3
Acetic acid electrolyte pH 2 + 0.25 M $NaClO_4$ @ 250 mA/cm^2	0.988	0.002	0.25	14	2.3	2.4
Acetic acid electrolyte pH 4 + 0.25 M $NaClO_4$ @ 250 mA/cm^2	0.926	0.007	0.25	14	3.5	3.7
Acetic acid electrolyte pH 5 @ 250 mA/cm^2	0.500	0.500	-	11	4.7	5.1

Acetic acid electrolyte pH 5 @ 250 mA/cm^2	0.500	0.500	-	11	4.7	9.7**
Acetic acid electrolyte pH 9 @ 250 mA/cm^2	0	1	-	9	8.6	9.3
Acetic acid electrolyte pH 9 + 0.1 M $NaHCO_3$ @ 250 mA/cm^2	0	1	-	8	8.4	9.3
Acetic acid electrolyte pH 9 + 0.5 M $NaHCO_3$ @ 250 mA/cm^2	0	1	-	7	8.4	9.3
Acetic acid electrolyte pH 12* @ 250 mA/cm^2	0	1	-	8	12	9.3

Table C.1 Specifications of the electrolyte properties used in the cyclic voltammetry and gas analysis experiments.

C.2. E-t profiles for constant current experiments

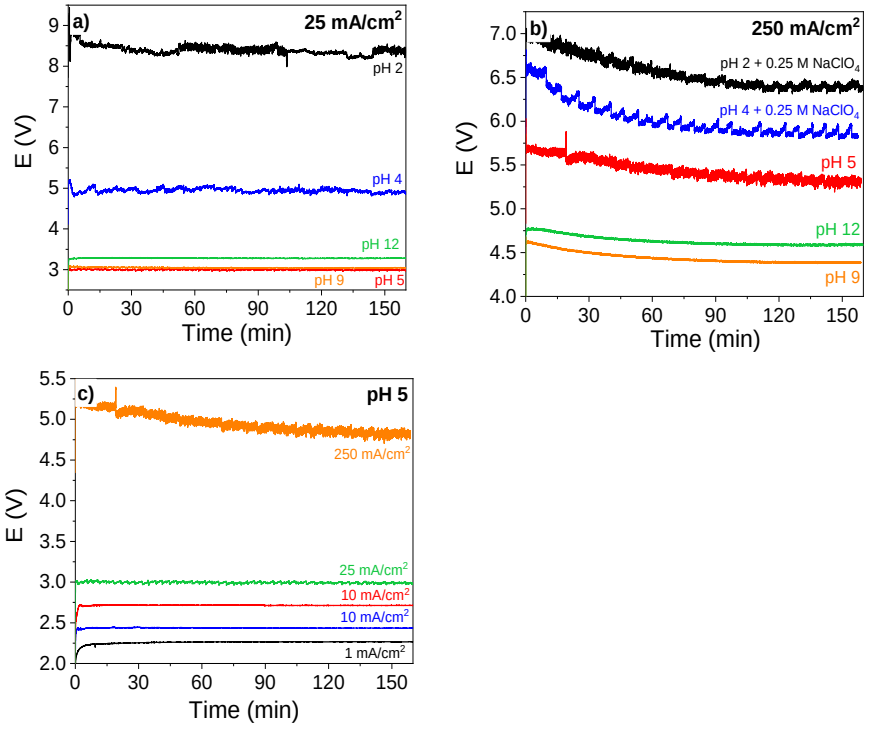

Figure C.2 Measured potential (V) vs time (s) for constant current experiment of 160 min with a) 1 M $CH_3COOH/NaCH_3COO$ with different pH at current densities 25 mA/cm^2 b) 1 M $CH_3COOH/NaCH_3COO$ with different pH at current densities 250 mA/cm^2 c) 1 M CH3COOH/NaCH3COO pH 5 at 1, 5, 10, 25 and 250 mA/cm^2. The potentials are uncompensated.

C.3. Effect of stirring on reaction-time dependent product selectivity for aqueous acetic acid electrolyte pH 4 and pH 5

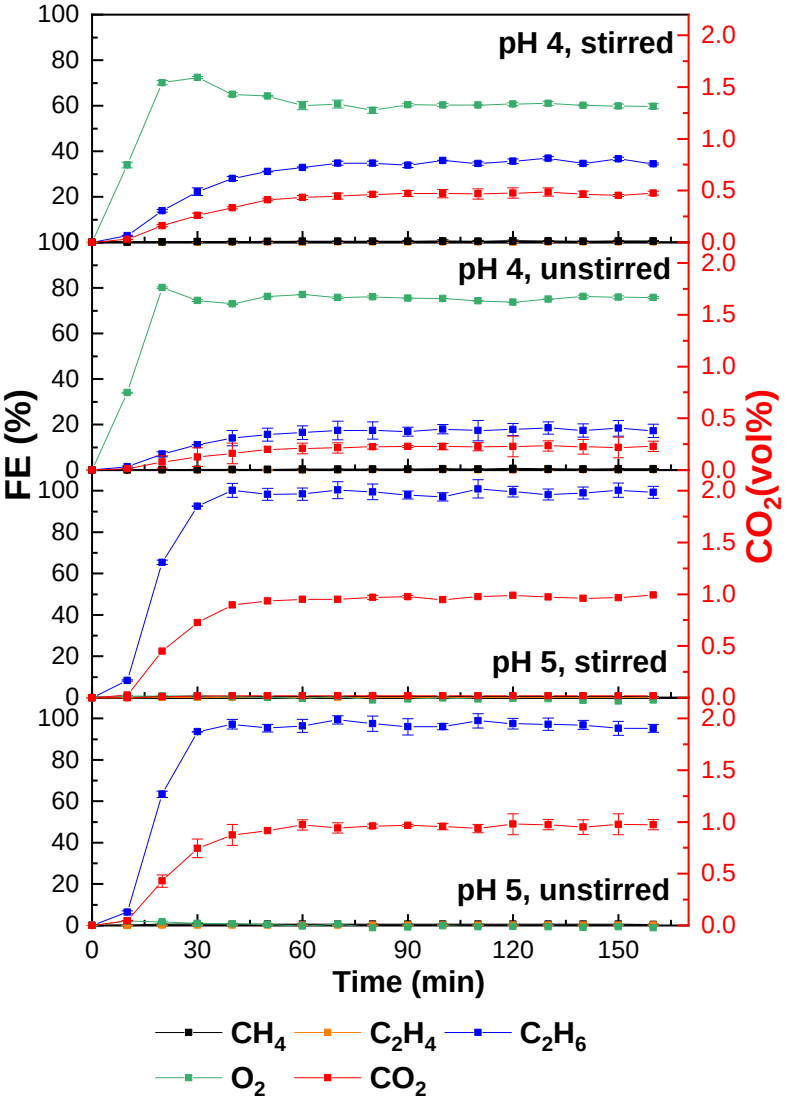

Figure C.3 Faradaic efficiency (%) over time (min) to methane (blank), ethylene (orange), ethane (blue), oxygen (green), and concentration of CO_2 (vol%) during a constant current experiment for 160 min at 25 mA/cm^2 in stirred (900 rpm) and unstirred solutions of electrolyte solution pH 4 and pH 5. n=2.

C.4. Carbonate equilibrium reactions

$CO_2\ (g) + H_2O \leftrightarrow H_2CO_3$ pH < 4.3 (C4.1)

$H_2CO_3 + H_2O \leftrightarrow HCO_3^- + H_3O^+$ 4.3 < pH < 8.2 (C4.2)

$HCO_3^- + H_2O \leftrightarrow CO_3^{2-} + H_3O^+$ pH > 8.2 (C4.3)

When the pH of the solution is < 4.3, dissolved CO_2 is in equilibrium with carbonic acid (Equation C4.1). In the pH range 4.3 < pH < 8.2, carbonic acid can donate a proton to form bicarbonate (Equation C4.2) and when the pH of the solution is higher than 8.2, bicarbonate ions donate another proton and form carbonate ions (Equation C4.3).

C.5. Faradaic efficiency to ethane over time with CO_2 presaturated electrolyte

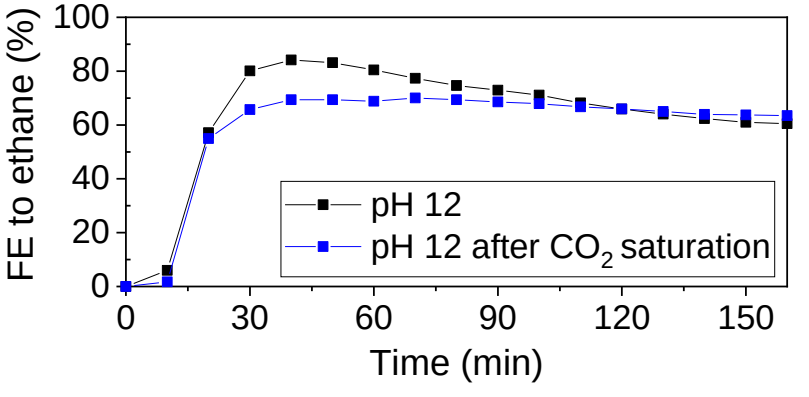

Figure C.5 Faradaic efficiency (%) over time (min) to ethane during constant current experiment of 25 mA/cm^2 for 160 min in electrolyte pH 12 with (blue) and without (black) presaturation of the electrolyte with carbon dioxide.

C.6. Faradaic efficiency to products during constant current experiments at 25 mA/cm^2

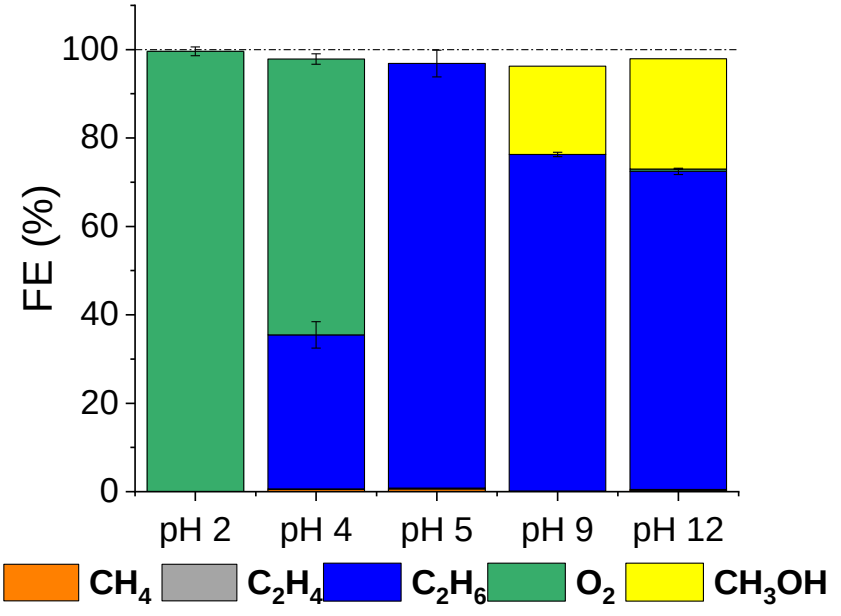

Figure C.6 Faradaic efficiency to methane, ethylene, ethane, oxygen and methanol during a constant current experiment for 160 min at 25 mA/cm^2 electrolyte solution with pH 2, 4, 5, 9 and 12. n=2 Faradaic efficiency to methane, ethylene, ethane, oxygen and methanol during a constant current experiment for 160 min at 25 mA/cm^2 electrolyte solution with pH 2, 4, 5, 9 and 12. n=2.

C.7. Cyclic voltammograms before and after constant current experiments at 25 mA/cm^2

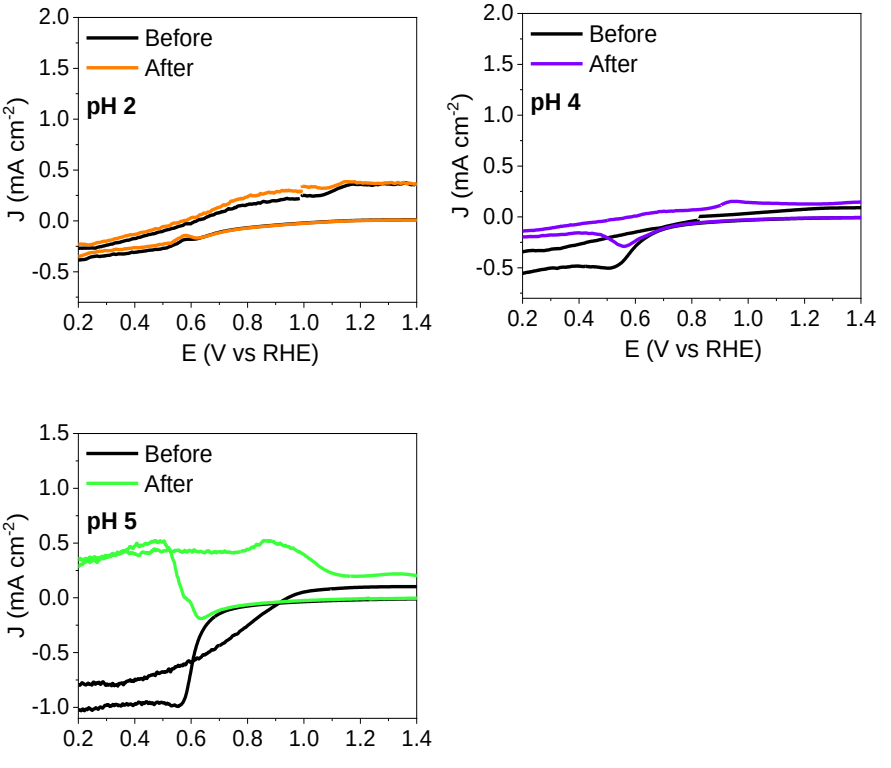

Figure C.7 Cyclic voltammogram of aqueous acetic acid electrolyte at a) pH 2 b) pH 4 c) pH 5 at scan rate 50 mV/s before and after a constant current experiment of 160 min at 25 mA/cm^2. The voltages are uncompensated.

C.8. Prolonged electrolysis in mildly acidic (pH 5) electrolyte

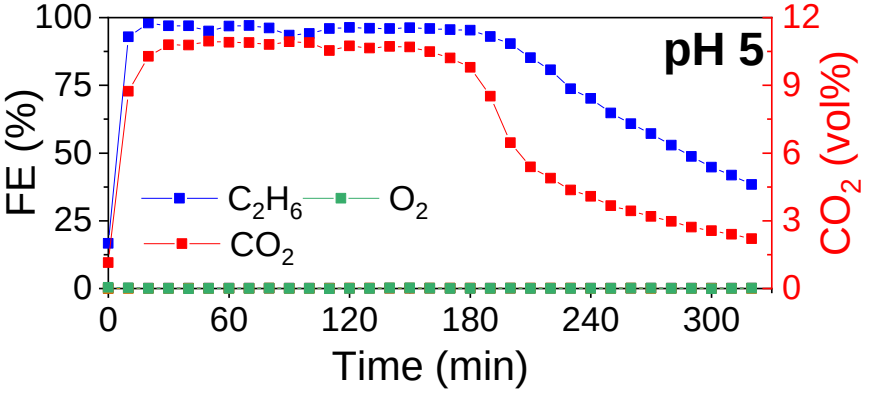

Figure C.8 FE (%) to ethane (blue) oxygen (green) and CO_2 (red) concentration (vol%) over time during prolonged constant current experiment of 250 mA/cm^2 in aqueous acetic acid electrolyte with pH 5.

C.9. Influence of supporting electrolyte on Kolbe electrolysis in aqueous solutions of acetic acid with pH 2 and 4

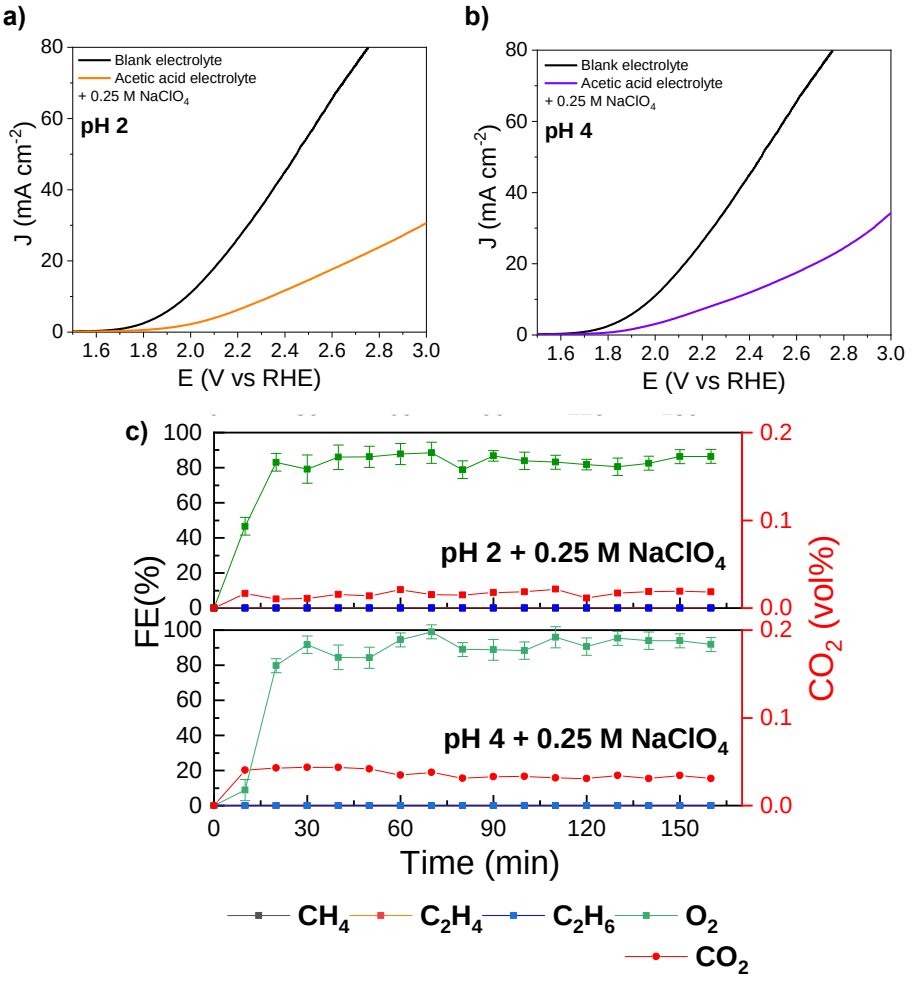

Figure C.9 Linear Sweep Voltammogram of a) 1 M CH_3COOH pH 2 (orange) and 1 M CH_3COOH + 0.25 M $NaClO_4$ pH 2 (black) and b) 1 M $CH_3COOH/NaCH_3COO$ pH 4 (purple) and 1 M $CH_3COOH/NaCH_3COO$ + 0.25 M $NaClO_4$ pH 4 (black) recorded with scan rate of 10 mV/s and stirring rate of 900 rpm c) FE (%) and CO_2 concentration (vol%) over time (min) during Kolbe electrolysis of aqueous solutions of acetic acid with a) pH 2 + 0.25 M $NaClO_4$, b) pH 4 + 0.25 M $NaClO_4$ with methane (black), ethylene (orange), ethane (blue) oxygen (green) and carbon dioxide (red) at 25 mA/cm^2 in 100 mL undivided cell using a stirring rate of 900 rpm. Every 10 min a gas sample was analysed, n=2.

C.10. Faradaic efficiency over time for different electrolytes at 250 mA/cm^2

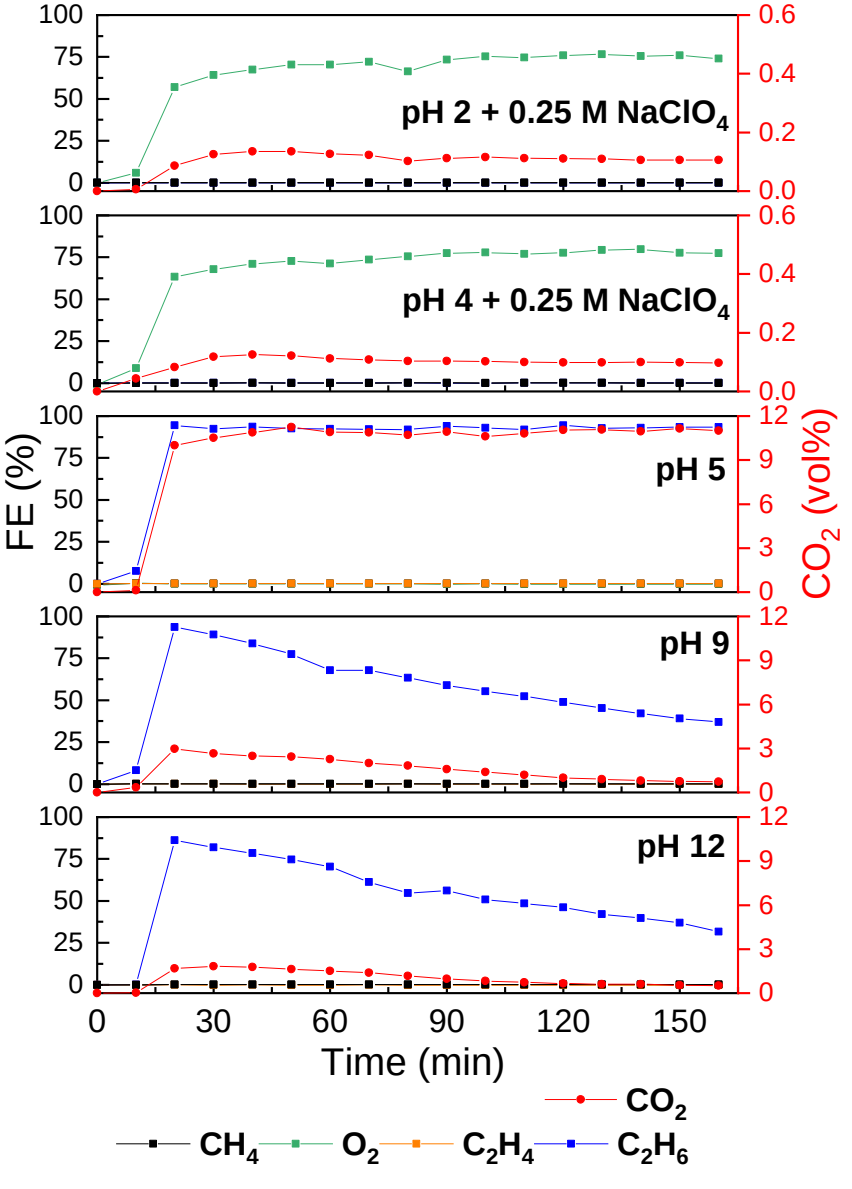

Figure C.10 FE over time during Kolbe electrolysis of aqueous solutions of acetic acid with a) pH 2 + 0.25 M $NaClO_4$, b) pH 4 + 0.25 M $NaClO_4$, c) pH 5 d) pH 9 and e) pH 12 with methane (orange), ethylene (black), ethane (blue) and oxygen (green) at 250 mA/cm^2 in 100 mL undivided cell. Every 10 min a gas sample was analysed.

Appendix D: Supplementary information to Chapter 5

D.1. External calibration curves liquid analysis

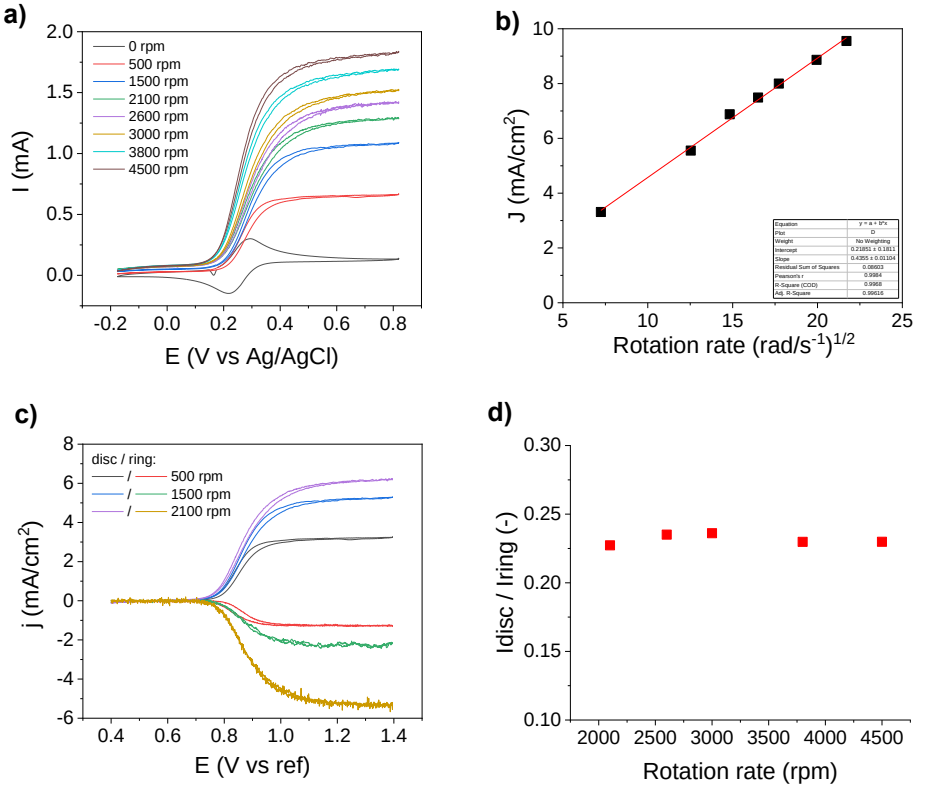

Figure D.1 a) Cyclic voltammogram of a Pt disc in 10 mM $K_4Fe(CN)_6$ and 1 M KNO_3 at 50 mV/s as a function of rotation rate; and b) Levich plot showing the limiting current density (taken at 0.7 V vs ref) as a function of the square root of rotation rate; c) Cyclic voltammogram of a Pt disc, Pt ring RRDE at 50 mV/s in 10 mM $K_4Fe(CN)_6$ and 1 M KNO_3, E_{ring} = +0.1 V; d) Theoretical efficiency (I_{disc} divided by I_{ring}) plot vs. the rotation rate obtained from data in Figure D.1c.

D.2. Cyclic voltammograms of C_3 and C_6 acid in C_2 acid buffer and reference Temkin adsorption isotherm of C_2 acid

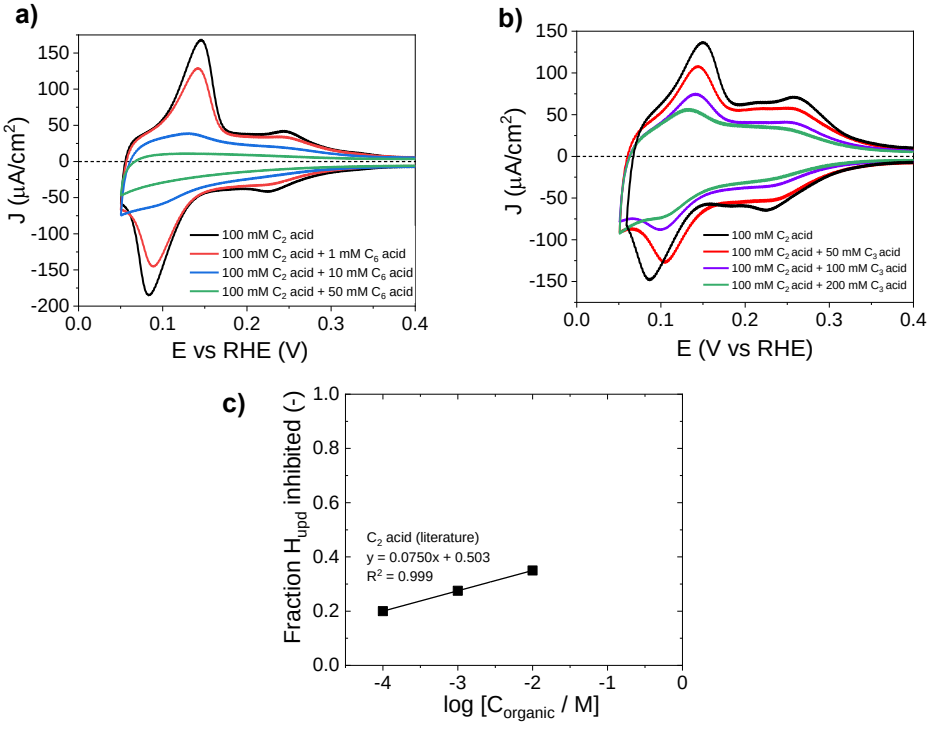

Figure D.2 a) Cyclic voltammograms showing hydrogen underpotential deposition of 50, 100 and 200 mM C_3 acid in 100 mM C_2 acid buffer b) 1, 10 and 50 mM C_6 acid in 100 mM C_2 acid buffer at 100 mV/s at room temperature. c) Temkin adsorption isotherm of C_2 acid in 1 M $HClO_4$ electrolyte

The data for the Temkin isotherm of C_2 acid was extracted from adsorption data provided in the work of Gilman et al.[155]

D.3. Galvanic square waveform pulses

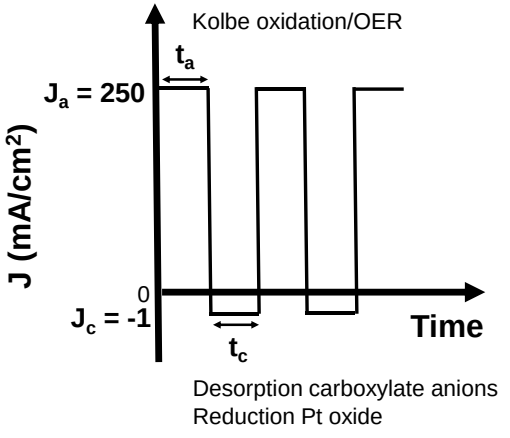

Figure D.3 Schematic representation of galvanic square waveform pulses, with an anodic current density (J_a) of 250 mA/cm^2 and cathodic current density (J_c) of -1 mA/cm^2. t_a and t_c present the duration of the anodic and cathodic pulse, respectively.

Upon applying the negative cathodic pulse, Kolbe electrolysis is interrupted. Carboxylate anions desorb from the platinum electrode surface by the opposing charge, which leads to the disruption of the carboxylate layer. Additionally, oxidation of the Pt surface oxide will occur. During the positive anodic pulse, the conditions for Kolbe electrolysis will restore again.

Table D.3 Ratio anodic/cathodic pulse charge (-) and FE to OER for different cathodic pulse durations. The anodic was fixed at 250 mA/cm^2 for 200 ms corresponding to an anodic pulse charge (Q_a) of 50000 µC.

t_c (ms)	Q_c (µC)	Ratio Q_a/Q_c (-)	FE to OER (%)
0	0	-	0
50	50	1000	0.5
150	150	333	2
300	300	166	9
400	400	125	13
500	500	100	22

D.4. Faradaic Efficiencies during galvanic square waveform pulsed experiments

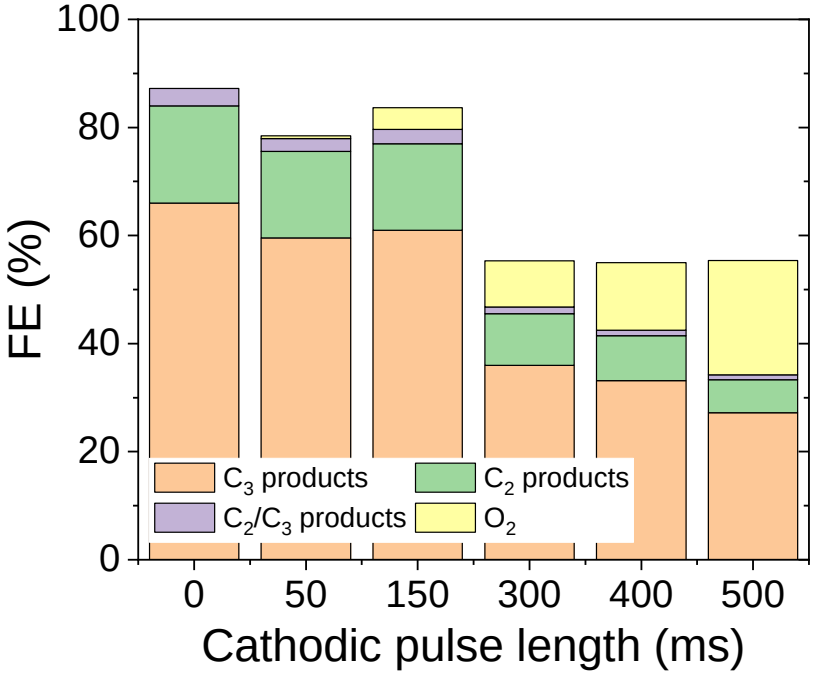

Figure D.4 Faradaic Efficiency (%) to C_2, C_3 and C_2/C_3 products during galvanic square waveform pulsed electrolysis of 1:1 mixture of acetic acid (C_2) and propionic acid (C_3) at pH 5 and with a total acid concentration of 1 M.

D.5. Cyclic voltammograms of Pt in 1:1 mixture C_2 and C_3 acid before and after galvanic square waveform pulsed experiments

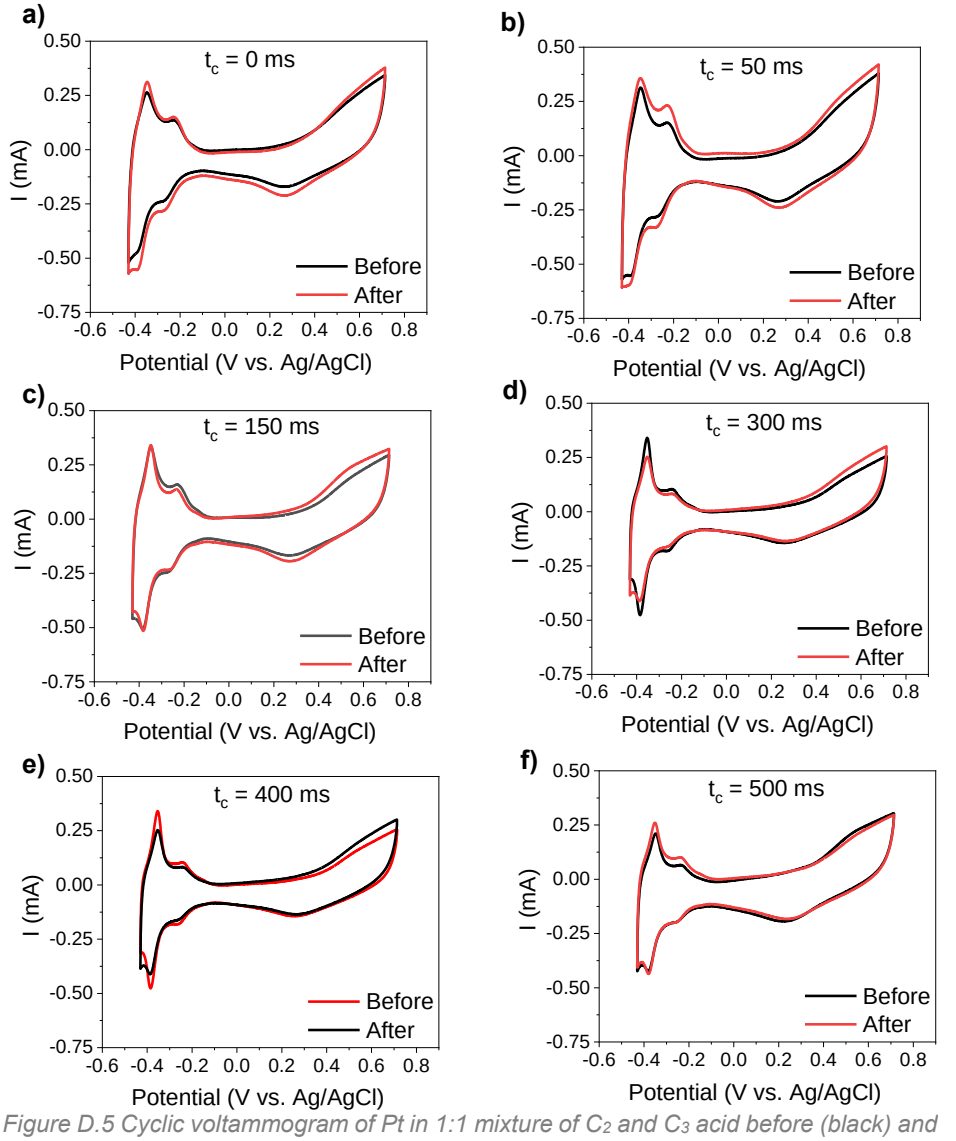

Figure D.5 Cyclic voltammogram of Pt in 1:1 mixture of C_2 and C_3 acid before (black) and after (red) for a) direct current experiment with t_c = 0 and galvanic square waveform pulsed experiments with a cathodic pulse duration of b) 50 ms, c) 150 ms, d) 300 ms, e) 400 ms and d) 500 ms. The scan rate was 200 mV/s.

List of journal publications

Olde Nordkamp, M., Mei, B. & Mul, G. Substrate specificity and product selectivity in mixed Kolbe electrolysis of short-chain carboxylic acids. *In preparation.*

Nordkamp, M.O., Ashraf, T., Altomare, M., Borca, A. C., Ghigna, P., Priamushko, T., Cherevko, S., Saveleva, V.A., Atzori, C., Minguzzi, A., He, X., Mul, G. & Mei, B. T. (2024). Investigating the Platinum Electrode Surface During Kolbe Electrolysis of Acetic Acid. *Surfaces and Interfaces*, 44, 103684, DOI: 10.1016/j.surfin.2023.103684.

Nordkamp, M.O., Mei, B., Venderbosch, R., & Mul, G. (2022). Study on the Effect of Electrolyte pH during Kolbe Electrolysis of Acetic Acid on Pt Anodes. *ChemCatChem*, *14*(16), **2022**. e202200438. DOI: 10.1002/cctc.202200438.

Soucie, H., **Olde Nordkamp, M.**, Faegh, E., Elam, M., Mul, G., & Mustain, W. (2021). Effects of pH and Potential in Kolbe Electrolysis of Acetate on Platinum. *Electrochemical Society Meeting Abstracts 240*, DOI: 10.1149/MA2021-02175mtgabs.

About the author

Margot Olde Nordkamp was born on 27th of February 1995 in Oldenzaal in the Netherlands. She obtained her bachelor degree in Chemistry in 2017 at Saxion University of Applied Sciences in Enschede, the Netherlands. During her bachelor, she completed a pre-master Sustainable Energy Technology at the University of Twente in Enschede, the Netherlands. She finished her bachelor thesis in the group of Prof. dr. Guido Mul focusing on 'The overall water splitting reaction photocatalyzed by strontium titanate and tungsten oxide'.

After her bachelor degree, she continued her master Sustainable Energy Technology at the University of Twente. In her second year, she went abroad for five months to follow specialization courses at Instituto Superior Técnico in Lisbon, Portugal. Margot finished her master thesis in the group of Prof. Dr. Sascha Kersten and in the group of Prof. dr. Guido Mul on 'Characterization of a bipolar membrane in a bicarbonate-formate redox system'.

Afterwards, Margot started her doctoral education at the University of Twente as well in the group of Prof. Dr. Guido Mul. For four and a half years, she has worked on the electrochemical decarboxylation of carboxylic acids over platinum surfaces for bio-oil upgrading. The research performed is described in this thesis.

Acknowledgements

The time to conclude my doctoral dissertation has come, and I reflect upon four remarkable years. These years were characterized by learning and personal development, not only in my academic endeavors, but also on a personal level. I have gained an immense amount of knowledge, experienced valuable moments and established unique relationships that have enriched my life. But above all, I thoroughly enjoyed this period.

This journey would have been considerably more challenging without the support, guidance and encouragement of the people in my surroundings. Their assistance was fundamental to my success. Hence, I wish to express my profound gratitude for their pivotal role during this incredible journey of pursuing my PhD.

First and foremost, I would like to express my deepest appreciation to my supervisors Guido and Bastian. **Guido**, thank you for the confidence in allowing me to conduct my bachelor, master and PhD within your research group. I admire how you always approach challenges from a different angle. Besides, your enthusiasm is contagious and significantly contributed to my drive to persevere during moments of discourage. **Bastian**, I highly appreciate that I could always count on you, even when you were no longer physically present at the university. Your valuable insights and constructive feedback have substantially improved the quality of my dissertation. Thanks to both for giving me the freedom to develop myself and steer my project.

Robbie, thank you for the great time at BTG. Although your enthusiasm and flood of research ideas could sometimes overwhelm me, they mostly provided new inspiration. Following your advice, we scheduled meetings primarily on Fridays, as at that day there were fries for lunch. I hope that in the near future, we will witness the utilization of electrochemistry within BTG for large scale bio-oil upgrading.

I am also grateful to the members of my graduation committee. **Prof. dr. Harnisch, Prof. dr. Bruijnincx, Prof. dr. Nijhuis and Prof. dr. Kersten**. Thank you for participating in my graduation committee and for sharing your expertise and invaluable feedback with me. I hope we are going to have fruitful discussions during my defense.

I also would like to express my sincere appreciation to RVO and TKI-BBE for their financial support, without which this research would not have been possible.

Then, I would like to express my heartfelt gratitude to the members of PCS. **Robert**, bedankt voor het vertalen van mijn technische vraagstukken naar praktische oplossingen. Jij wist het altijd voor elkaar te krijgen om een werkende experimentele opstelling te realiseren. Ik heb genoten van onze gesprekken (al dan niet werk gerelateerd) en wil je bedanken voor het delen van je (technische) kennis. Ik hoop dat je binnenkort gaat genieten van je welverdiende pensioen. **Wout,** ondanks dat wij niet heel lang samen hebben gewerkt, vond ik het altijd erg gezellig als je aanwezig was tijdens lunchpauzes en PCS activiteiten. Ik bewonder hoe snel jij technische problemen hebt opgepakt en je werkzaamheden eigen hebt gemaakt. Ik denk dat de vakgroep enorm boft met een technicus zoals jij. **Dorothy**, bedankt voor je hulp bij het regelen van de organisatorische zaken omtrent mijn promotietraject. Dankzij jouw puzzelvaardigheden konden afspraken met Guido snel gepland worden. Daarnaast ben jij een van de bindende factoren binnen PCS. De energie die jij steekt in het organiseren van sociale activiteiten waardeer ik enorm.

Also thanks to the members of the scientific staff: Annemarie, Georgios, Marco and Kasper. **Annemarie**, door de pandemie hebben we elkaar weinig gesproken, toch vind ik je een betrokken persoon die altijd in is voor een gezellig gesprek. **Georgios**, your assistance in conducting and interpreting the IRRAS measurements is very much appreciated. **Marco**, a big thanks to you for helping me with the preparation and interpretation of the XAS measurements. With your valuable input, we managed to publish the data in the form of a nice article. **Kasper,** jij bent een constante factor geweest in mijn tijd bij PCS. Door de jaren heen ben je een vriend geworden waarop ik kon terugvallen voor goede

adviezen maar ook voor een luisterend oor. Daarnaast zorgden jouw (flauwe) grappen regelmatig voor een glimlach op mijn gezicht. Ook bedankt voor je waardevolle input op mijn proefschrift, deze heeft zeker bijgedragen aan het verbeteren van de kwaliteit. Ik hoop dat de PCS groep nog lang van jouw aanwezigheid mag genieten.

Following my paranymphs, Tessa and Nathàlia, thank you for all the support, not only during the final stages of my PhD but throughout my time at PCS. **Nathàlia**, you are an incredible colleague always willing to help. I enjoyed our collaborative effort on GC maintenance and troubleshooting. Moreover, I cherish our long lab conversations about our weekend plans and shared interest such as sports and cooking. Our common aversion to coriander will always be a unifying factor. **Tessa,** jouw komst naar PCS heeft nieuw leven geblazen in de vakgroep. Met jouw ondernemende, creatieve en sociale mindset zorg je voor opwinding en saamhorigheid in de groep. De dagen met jou op het lab waren nooit saai. Ik hoop dat de klanken van het Foute Uur nog lang in het lab te horen zullen zijn.

Also, thanks to Lisanne, David and Jorik for sharing an office with me. **David**, thank you for teaching me the tips and tricks in Matlab and SolidWorks and for giving me a morning peptalk when I felt demotivated to do experiments. I hope you will not need these peptalks and complete your work in time. **Lisanne**, ondanks dat je niet vaak op kantoor werkte, vond ik het toch altijd erg gezellig als je er was. De geur van zoete thee en jouw prachtige tekeningen aan de muur maakten ons kantoor een fijne plek om te werken. **Jorik,** hoewel onze overlap in het kantoor kort was, vond ik het fijn dat de lege plek eindelijk weer opgevuld werd. Geniet van je tijd in de PCS groep.

Talal, with your arrival, I finally had a research buddy with whom I could engage in in-depth scientific discussions. I was impressed by the expertise and work experience you brought, so it did not surprise me that you were able to publish so early on in your PhD. In addition to this, you are a great colleague always willing to assist but also to chat and drink a cup of tea. Thank you for joining me to Grenoble; this was an experience I will not soon forget. **Shreyas,** you are a great person to be around, talkative and humorous but at the same time

hardworking. Your assistance in sputtering samples and making SEM images made a significant contribution to my research. Also, thanks for organizing the PCS borrels together with Nathàlia; they always provided a pleasant way to end the workweek. I wish you the best of luck in completing your PhD. P.S. Until that time, I will continue tagging you in PhD memes. **Shri,** thank you for helping me, especially with 3D printing. Even though you had a busy agenda yourself, you always found time. This is highly appreciated. Good luck with writing your thesis (it's not that bad). **Max,** jouw fascinatie voor duurzaamheid en politiek is bewonderingswaardig. Dankzij jou leerde ik dat je zonder al te veel moeite recepten veganistisch kunt maken. **Anneloes,** dankzij jouw toezicht beschikt de PCS groep nu over brandschone labs (en een volle fotogalerij). Ook bedankt voor de zelfgemaakte stickers die Whatsapp gesprekken naar een hoger niveau hebben getild. **Adam,** besides engaging in endless scientific discussions with you, I also found great amusement (thanks to you). Particularly, past N3C conference was a memorable experience. **Tursun**, I admire your perseverance. It is not easy to work with a GC that may stop working at any moment. **Dalia**, thank you for always being kind to me. Even though we did not work together much, I enjoyed our little corridor conversations. **Lukas**, door het doen van je bachelor en master opdracht en PhD traject in de PCS groep bewandel jij hetzelfde pad als ik gedaan heb. Ik wens je heel veel plezier en succes in je promotietraject. Also, thanks to the rest of the members of PCS with whom I spent time during my PhD: **Kim, Ellen, Shrisendu, Rakesh, Yusen, Fernanda, Marco and Sean**.

As I was trapped in between two generations of PhD students, I also would like to acknowledge the 'first' generation of PhD students: **Vera, Robert, Nakul, Devin, Mozhgan, Martijn, Liniker, Piotr, Ronald, Anne, Kaijian and Ainoa**. **Ainoa**, as you became a true friend during my time at PCS, it was sad to see you leaving. Because we were in the same phase of our PhD trajectory, we faced similar challenges and could use each other to vent. I still believe that our way to deal with these struggles, simply by laughing about them, was the best way. I will carry our shared nickname 'oxidation girl' with me forever.

I also would like to thank the people that supported my research activities. **Shahab**, many thanks for facilitating the HPLC analysis. Without this, a significant part of my research would not be there. Besides, I always enjoyed having you as company in ME142. **Robert Beltman**, ik kan jou niet onbenoemd laten. Bedankt voor je hulp bij het ontwerpen en fabriceren van reactor(onderdelen). Zonder aankondiging en met weinig ervaring betrad ik de werkplaats, maar dankzij jouw geduld en deskundigheid verliet ik deze altijd met een helder ontwerp. Ook wil ik je bedanken voor de gezellige gesprekken. Ik hoop dat je binnenkort zult genieten van je pensioen.

Ook wil ik de studenten bedanken waar ik afgelopen jaren mee samengewerkt heb: **Laura, Thijs en Tim**. Bedankt voor jullie waardevolle bijdrage aan mijn proefschrift.

Ik wil mijn (schoon)familie, vrienden en vriendinnen bedanken voor alle steun en oprechte interesse in de afgelopen jaren. Jullie boden niet alleen een luisterend oor, maar zorgden ook voor de gewenste afleiding. Dit hielp me eraan herinneren dat er meer in het leven is dan alleen een PhD. **Papa en mama**, bedankt dat jullie mij de vrijheid hebben gegeven om mezelf te ontwikkelen en mijn eigen pad te bewandelen.

Tot slot, **Erik**, wil ik mijn diepste waardering aan jou uiten. Niet alleen voor je onvoorwaardelijke steun, maar ook voor de liefde, het begrip en de aanmoediging die je me de afgelopen jaren hebt gegeven. Jij was een vangnet in moeilijke tijden, maar vierde ook samen met mij de hoogtepunten. Jij bent mijn grootste supporter en dat waardeer ik meer dan woorden kunnen uitdrukken.